UNIVERSITY OF CALIFORNIA

Santa Barbara

Molecular beam epitaxy of electronic perovskite oxides: $BaSnO_3$, Sr_3SnO, and $Eu_xSr_{1-x}SrTiO_3$

A dissertation submitted in partial satisfaction of the

requirements for the degree of

Doctor of Philosophy in Materials

by

Nicholas Glenn Combs

Committee in charge:

Professor Susanne Stemmer, Chair

Professor Stephen D. Wilson

Professor John W. Harter

Professor Bolin Liao

March 2023

The dissertation of Nicholas Glenn Combs is approved.

Bolin Liao

John W. Harter

Stephen D. Wilson

Susanne Stemmer, Committee Chair

March 2023

Molecular Beam Epitaxy of Electronic Perovskite Oxides: $BaSnO_3$, Sr_3SnO, and $Eu_xSr_{1-x}SrTiO_3$

Nicholas Glenn Combs

Curriculum Vitæ

Nicholas Glenn Combs

Education

2023 **Doctor of Philosophy** in Materials, University of California, Santa Barbara

2017 **B. Sc. in Materials Science and Engineering**, University of Tennessee

Publications

2023 **N. G. Comb**s, H. Jeong, R. Russell, L. Kautzsch, T. N. Pardue, T. E. Mates, S. D. Wilson, J. W. Harter, S. Stemmer. "Ferroelectricity and superconductivity in strained $Eu_xSr_{1-x}TiO_3$ films." Phys. Rev. B 107, 094504.

2022 W. Wu, **N. G. Combs**, S. Stemmer. "Revealing the intrinsic transport properties of antiperovskite Sr_3SnO thin films." Appl. Phys. Lett. 121, 233101.

H. Jeong, R. Russell, **N. G. Combs**, T. N. Pardue, J. W. Harter, S. Stemmer. "Similarity in the critical thicknesses for superconductivity and ferroelectricity in strained $SrTiO_3$ films." Appl. Phys. Lett. 121, 012601.

A. P. Kaijdos, **N. G. Combs**, S. Stemmer. "Hybrid molecular beam epitaxy." In *Epitaxial Growth of Complex Metal Oxides, Second Edition.* Editors: G. Koster, M. Huijben, G. Rijnders. Elsevier. Book chapter.

C. Lau, **N. G. Combs**, E. Karapetrova, J. Jiang, S. Stemmer, C. H. Ahn, F. J. Walker. "Resonant x-ray scattering method for measuring cation stoichiometry in $BaSnO_3$ thin films." J. Vac. Sci. Technol. A 40, 013411.

2021 H. Jeong, **N. G. Combs**, S. Munyan, A. Rashidi, S. Stemmer. "Reducing surface depletion of superconducting $SrTiO_3$ films with $EuTiO_3$ capping layers." Appl. Phys. Lett. 119, 162601.

W. Wu, **N. G. Combs**, S. Stemmer. "Molecular beam epitaxy of phase-pure antiperovskite Sr_3SnO thin films." Appl. Phys. Lett. 119, 161903.

J. Cheng, H. Yang, **N. G. Combs**, W. Wu, H. Kim, H. Chandrasekar, C. Wang, S. Rajan, S. Stemmer, W. Lu. "Electron transport of perovskite oxide $BaSnO_3$ on (110) $DyScO_3$ substrate with channel-recess for ferroelectric field effect transistors." Appl. Phys. Lett. 118, 042105.

K. Thirunavukkuarasu, R. Richardson, Z. Lu, D. Smirnov, N. Huang, **N. G. Combs,** G. Pokharel, D. Mandrus. "Magneto-elastic coupling in multiferroic metal-organic framework $[(CH_3)_2NH_2]Co(HCOO)_3$." AIP Adv. 11, 015040.

2020 **N. G. Combs**, W. Wu, S. Stemmer. "Stoichiometry control in molecular beam epitaxy of $BaSnO_3$." Phys. Rev. Mat. 4, 014604.

W. Wu, **N. G. Combs**, T. E. Mates, S. Stemmer. "Carbon impurity concentrations in $BaSnO_3$ films grown by molecular beam epitaxy using a tin oxide source." J. Vac. Sci. Technol. A 38, 043405.

J. Cheng, H. Yang, C. Wang, **N. G. Combs**, C. Freeze, O. Shoron, W. Wu, N. K. Kalarickal, H. Chandrasekar, S. Stemmer, S. Rajan, W. Lu. "Nanoscale etching of perovskite oxides for field effect transistor applications." J. Vac. Sci. Techol. B 38, 012201.

2017 R. Mukherjee, H. J. Chuang, M. R. Koehler, **N. Combs**, A. Patchen, Z. X. Zhou, D. Mandrus. "Substitutional electron and hole doping of WSe_2: synthesis, electrical characterization, and observation of band-to-band tunneling." Phys. Rev. Appl. 7, 034011.

Conference Presentations

2022 APS March Meeting 2022 – "Thickness dependence of the interplay between superconductivity and ferroelectricity in compressively strained $SrTiO_3$ thin films." Presented virtually. March 16. Focus session.

2019 19^{th} International Conference for Crystal Growth and Epitaxy – "High-mobility heterostructures with $BaSnO_3$." Keystone, CO. July 31. Invited talk.

Fellowships

2019-2022 **Quantum Foundry Traineeship Program** – Graduate fellow. Funded through the NSF Q-AMASE-i initiative.

Abstract

Molecular Beam Epitaxy of Electronic Perovskite Oxides: $BaSnO_3$, Sr_3SnO, and $Eu_xSr_{1-x}TiO_3$

by

Nicholas Glenn Combs

Perovskite oxides are a class of materials known to exhibit a wide range of electronic, magnetic, and other functional properties. In their simplest forms they have the chemical formula ABO_3, where the O is oxygen and *A* and *B* are cations. Different combinations of the *A* and *B* cations lead to a plethora of properties in electronic structure, magnetism, structural transitions, quantum phases, and more. In addition, certain inversions of this relatively simple structure, such as the *anti*perovskites, open up an entirely new realm of topologically nontrivial materials that offer even more avenues of exploration. Molecular beam epitaxy (MBE) is a thin film growth technique which is known for its ability to produce films of the highest quality (i.e. low defect density) with multiple levels of control, making it an excellent tool for the study of novel perovskite oxides.

$BaSnO_3$ is a transparent semiconductor which displays high electron mobilities at room-temperature when single crystals are doped with La. These mobilities are accessed at high carrier densities, opening up possibilities for uses in high power density electronics and

transparent conductor applications. Thin films have so far been unable to match the mobilities exhibited by single crystals, however. In this thesis, I will describe studies aimed towards understanding the various mobility-limiting mechanisms at play in thin film $BaSnO_3$. These show that while dislocations may a prominent role in limiting mobility at the moment, ultimately it may be stoichiometry control which sets an upper limit on the mobility that can be achieved in films.

Sr_3SnO is an *anti*perovskite oxide which exhibits topologically nontrivial band inversion in its bulk. It has only a protected band crossing at the Fermi level, making it a three-dimensional topological Dirac semimetal (or topological crystalline insulator if a small mass gap is considered). Additionally, superconductivity was discovered in polycrystalline samples, opening up the possibility that Sr_3SnO is an intrinsic topological superconductor. In this thesis I will describe my efforts involving getting the initial growth of this material by MBE off the ground. I will also discuss a protective capping scheme developed such that the material would degrade in air once removed from the growth chamber, as it is extremely air sensitive.

$SrTiO_3$ is one of the most well-studied perovskite oxides. It is a dilute superconductor, which challenges the traditional electron-phonon pairing mechanisms of BCS theory. It is also an incipient ferroelectric, meaning it is in proximity to a ferroelectric quantum phase transition. In this thesis I will describe experimental work – built on prior progress in the growth of high-quality $SrTiO_3$ thin films – to further examine the coexistence of ferroelectricity and superconductivity in $SrTiO_3$. By growing films alloyed with magnetic Eu ($Eu_xSr_{1-x}TiO_3$), I will show that superconductivity in $SrTiO_3$ is not only remarkably insensitive to magnetism, but may also be more strongly tied to the presence of static polar order than has been previously considered.

Table of Contents

List of Figures

List of Tables

Chapter 1. Introduction

1.1 Perovskite Oxides

Perovskite oxides are a class of materials that host one of the widest ranges of functional properties among a single material class which shares a common structure, from ferroelectrics to ferromagnets, antiferromagnets to antiferroelectrics, superconductors to high-k dielectrics, topologically nontrivial band structures to high-mobility semiconductors, to name a few. In their simplest forms they have chemical formula ABO_3, where O is oxygen and A and B are cations. The cubic perovskite crystal structure is shown in Fig. 1.1, where the A cations sit on the corners of the unit cell, the B cation is in the center and is six-fold coordinated by an octahedron of oxygen anions. The vast combinations of A and B cations that can be incorporated into this one structural motif offer a unique playground for exploring rich physics, much of which is still being uncovered. The fact that widely differing properties are exhibited by materials which share a common structural motif allows for relatively easy epitaxial integration via heterostructures on high-quality single crystal substrates, which serves to multiply the phase space of functionalities these materials can exhibit. In this thesis I will discuss my work with three different perovskite materials, all of which can be grown by

molecular beam epitaxy, and each with markedly different electronic properties from the others.

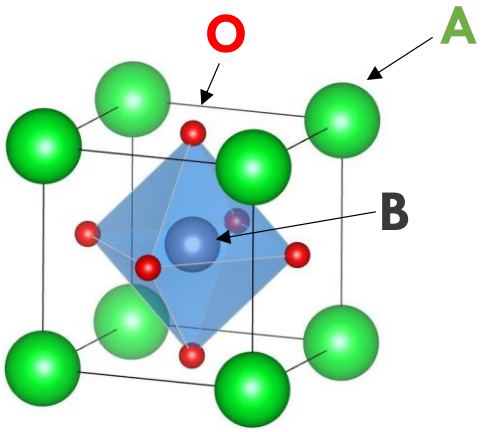

Figure 1.1 – Cubic perovskite crystal structure of ABO_3 perovskite oxide, showing the positions of the constituent elements.

1.1.1 $BaSnO_3$

Bulk $BaSnO_3$ has an ideal cubic perovskite structure (space group $Pm\bar{3}m$) with a lattice constant of 4.116 Å [1]. It is a transparent semiconductor with an indirect band gap of ~3.1 eV [2] and a direct band gap of ~3.4 eV [3]. The bottom of its conduction band is comprised primarily of Sn 5*s* orbitals [4], leading to a dispersive conduction band and low electron effective mass (m^*) of 0.19 m_e [5]. Single crystals of La-doped $BaSnO_3$ were found to exhibit maximum room-temperature electron mobilities (μ) above 300 $cm^2\ V^{-1}\ s^{-1}$ at carrier densities (n) above ~10^{19} cm^{-3} [6–8], the highest room-temperature μ of any semiconductor with $n >$ ~10^{19} cm^{-3} at the time (Fig. 1.2). This combination of high-temperature mobilities at high carrier densities in a material with a relatively wide band gap makes this material extremely

promising for uses in next-generation power electronic devices, especially when combined with other perovskites such as $BaTiO_3$ [9].

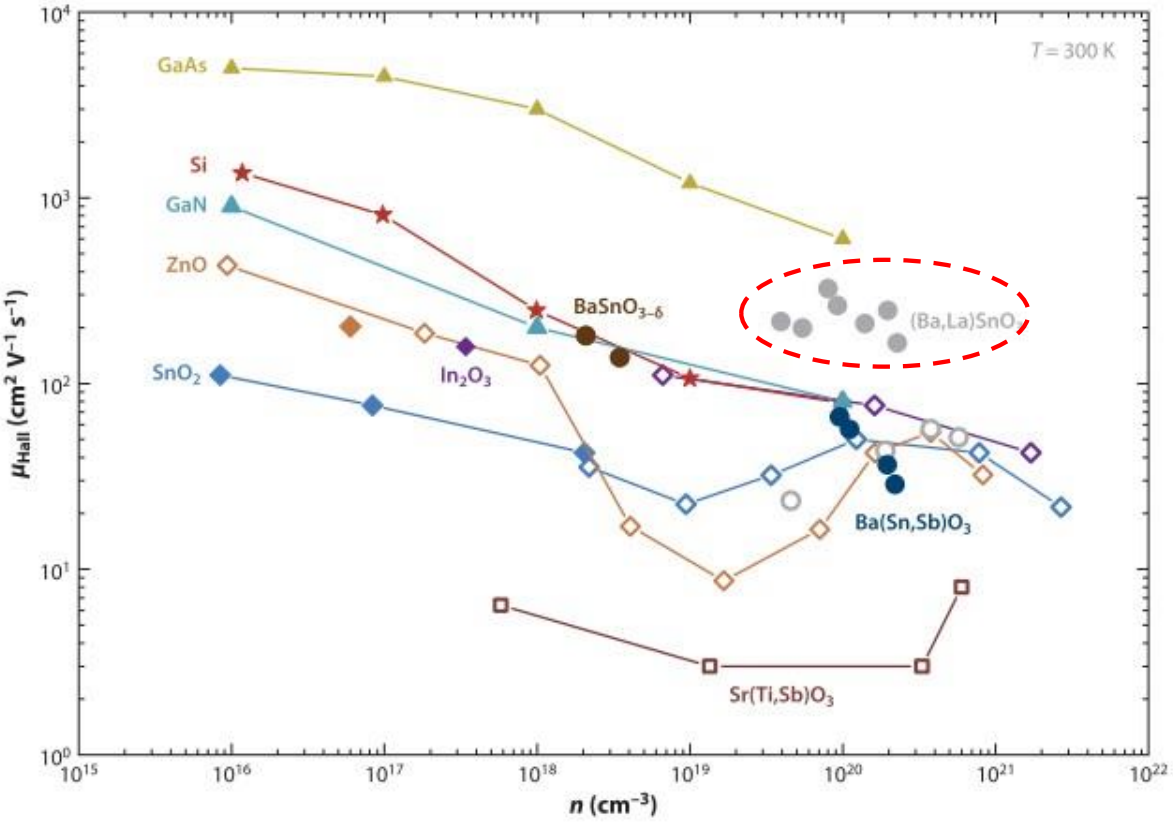

Figure 1.2 – Comparison of maximum room-temperature mobility μ_{Hall} as a function of carrier density n for various semiconductors. Adapted with permission from ref. [8]

1.1.2 Sr_3SnO

Sr_3SnO belongs to a family of *antiperovskite* oxides, with generic chemical formula A_3BO where A is an alkaline earth metal such as Ca, Ba, or Sr, and B is Sn or Pb. The antiperovskite crystal structure (Fig. 1.3a) is symmetrically equivalent to the perovskite structure except that the occupation of the A and O sites are swapped [10,11]. The A and O ions are generally

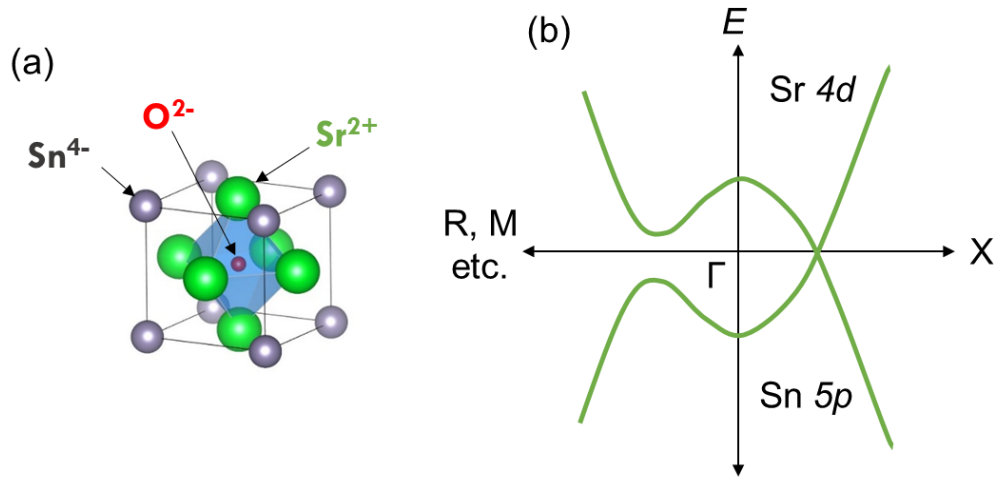

Figure 1.3 – (a) Cubic antiperovskite crystal structure of Sr_3SnO showing the formal charge states of the constituent elements. (b) schematic band structure of Sr_3SnO illustrating the band inversion along the Γ - X line and no other bands at the Fermi level. More correctly there is a small gap opened at the band crossing.

expected to retain their formal charge states of A^{2+} and O^{2-}, which forces the *B* metal into an unusual B^{4-} anionic state to maintain charge neutrality. This unusual electronic configuration leads to interesting electronic structures, such as band inversions, three-dimensional (3D) Dirac fermions, topologically non-trivial Chern numbers, and unique topological surface states [12–20]. Sr_3SnO exhibits six Dirac nodes along each of the equivalent *Γ-X* lines due to band inversion between Sr 4*d*- and Sn 5*p*- derived bands, which are protected from hybridizing due to the fourfold rotational symmetry [18] (see Fig. 1.3b for a schematic band structure). However, higher-order spin-orbit coupling effects induce a small gap at the Dirac nodes, effectively categorizing it as a topological crystalline insulator [13]. The smallness of the gap is such that the dispersion in the vicinity of these points is quasilinear and thus it approximates a 3D Dirac semimetal.

It was later reported that polycrystalline samples with an extremely high degree of Sr-deficiency ($Sr_{3-x}SnO$) exhibit superconductivity with a superconducting transition temperature (T_c) of ~5 K [21–23]. Sr vacancies induce *p*-type carriers (holes). Because of the combination of a superconducting phase emerging from a topologically nontrivial band structure, this lead to speculation that this material may be an intrinsic topological superconductor [16]. Topological superconductors are predicted to host non-Abelian anyons on their edges [24], which, aside from their fundamental physical interest, could serve as a platform for future topological quantum computing [25].

An important caveat to this excitement, however, is that superconductivity has only been observed in polycrystalline samples, which contain secondary phases [21–23]. Though the authors have taken much care to rule out the possibility of an additional phase as the source for the superconductivity, the claim remains uncertain unless it can be reproduced in other sample forms such as single crystals or thin films. This experimental endeavor, however, is itself not trivial, as the unusual Sn^{4-} anion makes these antiperovskite oxides extremely unstable in air due to the tendency for oxidation, which requires keen technical consideration when synthesizing and measuring.

1.1.3 $SrTiO_3$

$SrTiO_3$ is one of the most widely studied perovskite oxides due to its many interesting properties. In pure bulk form, it has a cubic perovskite structure ($Pm\bar{3}m$) at room temperature with a lattice constant of 3.905 Å [26]. It is a band insulator with indirect and direct band gaps of 3.3 eV and 3.8 eV, respectively [27]. It can be electron doped by a wide variety of dopants:

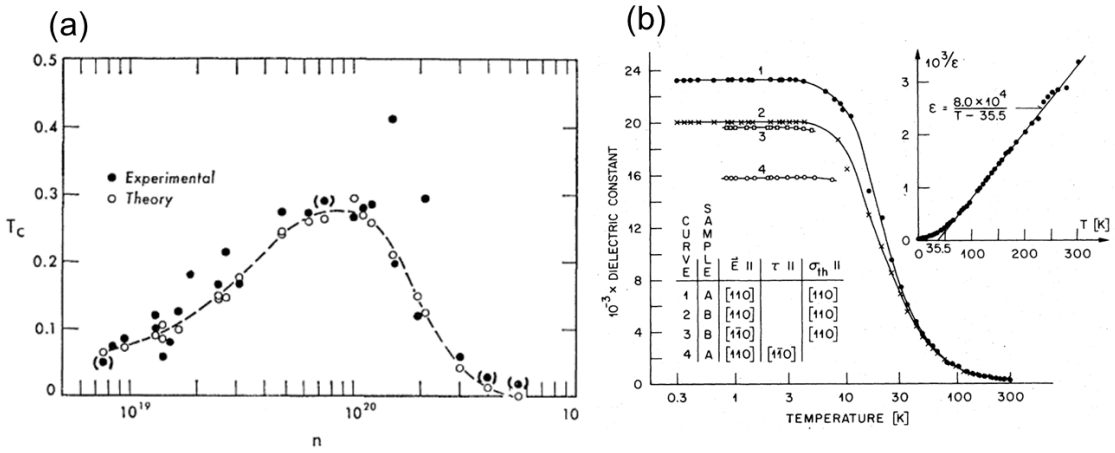

Figure 1.4 – (a) Superconducting T_c as a function of 3D carrier density n for $SrTiO_{3-\delta}$ crystals. Adapted with permission from ref. [36] (b) Static dielectric constant ε as a function of temperature for $SrTiO_3$ crystals. Adapted with permission from ref. [39]

substituting trivalent cations on the Sr-site (La, Sm, Gd, Nd) [28–31], substituting pentavalent cations on the Ti-site (Nb) [32], or by inducing oxygen vacancies [33].

Doped $SrTiO_3$ was the first discovered oxide superconductors [34]. Like many semiconductor superconductors, it exhibits a superconducting "dome" in carrier density [35,36] (Fig. 1.4a). It is also one of the most dilute superconductors, with a carrier density as low of the order $\sim 5 \times 10^{17}$ cm^{-3} [37]. This diluteness immediately challenged the applicability of the standard Bardeen-Cooper-Schrieffer (BCS) model describing the phonon-mediated electron-electron pairing. The so-called Migdal criterion generally requires that the phonons mediating the pairing, which have characteristic frequency ω_D , have an energy much less than the Fermi energy ϵ_F, i.e. $\omega_D / \epsilon_F << 1$, whereas in SrTiO3, $\omega_D / \epsilon_F \sim$ 1-100, among the highest ratio of any doped semiconductor superconductor [38].

$SrTiO_3$ is also an incipient ferroelectric (or equivalently, a quantum paraelectric), meaning it is in proximity to a ferroelectric ground state instability brought about by the softening of a low-energy transverse optical phonon [39]. While first-principles calculations predict a

ferroelectric ground state due to this soft-mode instability, it is thought that zero-point quantum fluctuations prevent the emergence of a long-range ordered state, and the frequency of the soft-mode levels off to a real frequency at low temperatures. This nearby paraelectric-ferroelectric transition is manifested by a rapidly increasing dielectric constant as temperature is lowered, which initially follows a Curie-Weiss behavior but then deviates from this and eventually saturates to a constant value by around 40 K (Fig. 1.4b). Numerous methods have been shown to be able tune the lattice into a ferroelectric ground state, which include chemical substitution on the *A*-site with Ca [40,41] and Ba [42], isotopic substitution of ^{18}O [43], applied uniaxial stress [44], and epitaxial strain [45,46].

As mentioned above, bulk, doped $SrTiO_3$ can become superconducting with a maximal T_c of ~450 mK (depending on how T_c is defined). It has been demonstrated that each of the various methods listed above to stabilize a ferroelectric ground state can also lead to enhancement of the superconducting T_c [31,41,46–51]. This phenomenon points to a strong link between the nature of the superconducting state and the incipient ferroelectricity in $SrTiO_3$, and a number of theories have been proposed to attempt to find this link [52–56]. While no consensus has been found to-date, there is mounting evidence that broken inversion symmetry might be key to the pairing, which has been relatively overlooked by many of the above proposed theories.

1.2 Electronic Transport in Thin Films

For a material to be utilized in electronic devices, it must first be grown as a thin film. Films also offer a unique geometry for testing various physical properties. Here we will

introduce some basic concepts of electronic transport, carrier scattering, and measurement of electronic properties, as pertaining to thin films.

1.2.1 Electronic transport theory

Ohm's law is the linear relationship between the electric field E and the current density J, related by the conductivity σ, which is also related to the carrier density n and the drift velocity v_d:

$$J = \sigma E = env_d \quad (1.1)$$

where e is the electron charge. At low electric fields, the drift velocity of an electron (or hole) is related to the electric field strength by the proportionality constant known as mobility or μ, which has units of $cm^2\ V^{-1}\ s^{-1}$, such that:

$$v_d = \mu E \quad (1.2)$$

The mobility is a measure of how easily or quickly a free electron moves under the influence of an electric field. It is a function of the electron's effective mass m^* and the various scattering mechanisms present in the solid, which is represented by the mean time between scattering events τ, such that:

$$\mu = \frac{e\tau}{m^*} \quad (1.3)$$

The mobility thus contains information about both the electronic structure (through m^*) and the scattering sources (through τ). The effect of the various scattering sources on the total mobility can be calculated as the simple sum of the mobility limits imposed by the individual scattering mechanisms (in the weak scattering limit), which is known as Matthiessen's rule:

$$\frac{1}{\mu} = \sum_i \frac{1}{\mu_i} \qquad (1.4)$$

1.2.2 Scattering Mechanisms

Scattering of free electrons in a periodic lattice (i.e. Bloch states) is caused by local deviations of the periodicity of the lattice. These deviations can be dynamic (e.g. phonons) or static in nature. Phonons are quanta of lattice vibrations resulting from thermal energy of the lattice, and thus their effect on mobility is temperature dependent. For metals and degenerate semiconductors, the effect of static scattering sources on mobility is relatively temperature-independent. Electron-electron scattering can also contribute to the total mobility, and its effect is temperature dependent. Thus, we can separate the total mobility into temperature dependent and temperature independent components:

$$\mu^{-1} = \mu^{-1}(T) + \sum_i \mu_i^{-1} \qquad (1.5)$$

where the μ_i^{-1} now represent the various mobility limits imposed by the residual (temperature-independent or static) disorder.

One of the most commonly expected static scattering sources in doped semiconductors is ionized impurity scattering due to the ionized dopant atoms. Charged impurities generally have a relatively strong effect on mobility due to the Coulomb potential emanating from them, though high-enough carrier densities can screen this potential to certain degrees. As such, neutral impurities can generally be expected to have a less-severe effect on mobility than charged impurities. In thin films, especially those which have undergone strain relaxation, dislocations can contribute significantly to scattering. The nature of dislocations in various

materials can strongly affect how they contribute to scattering. In $BaSnO_3$, for example, it is proposed that the relaxation-induced dislocations are charged entities, with a certain charge-per-unit-length gleaned from fitting models to experimental data [57,58]. These models, however, require a significant amount of assumptions, and their accuracy would depend on accounting for all relevant scattering sources in the films, which is not well-understood. Discussion of the finer points of the effects of various defects on mobility is not within the scope of this thesis, and so we will simply state that dislocations are likely a significant source of scattering, whether they are carrying a charge or not.

1.2.3 Hall Measurements

Mobility and carrier density can be measured in a lab setting by utilizing the Hall effect. The mobility measured via the Hall effect is the Hall mobility μ_H, which differs from the drift mobility by the Hall factor r_H:

$$\mu = \frac{\mu_H}{r_H} \quad (1.6)$$

The Hall factor typically takes values on the order of 1-2, dependent on the dominant scattering mechanism(s) and whether or not a semiconductor is degenerate [59]. A typical Hall effect measurement is a four-terminal measurement which can be performed in two common geometries: van per Pauw (vdP) [60] and Hall bars. Unless otherwise specified, all Hall measurements in this thesis were measured using the vdP method, shown in Fig. 1.5. Small contacts are deposited on the corners of a typical square sample, which we will label as 1, 2, 3, and 4 (Fig. 1.5a). The longitudinal resistance is first measured in both the *x* and *y* directions, which we denote as R_{xx} and R_{yy}. For R_{xx}, we apply a small current between contacts 1 and 4

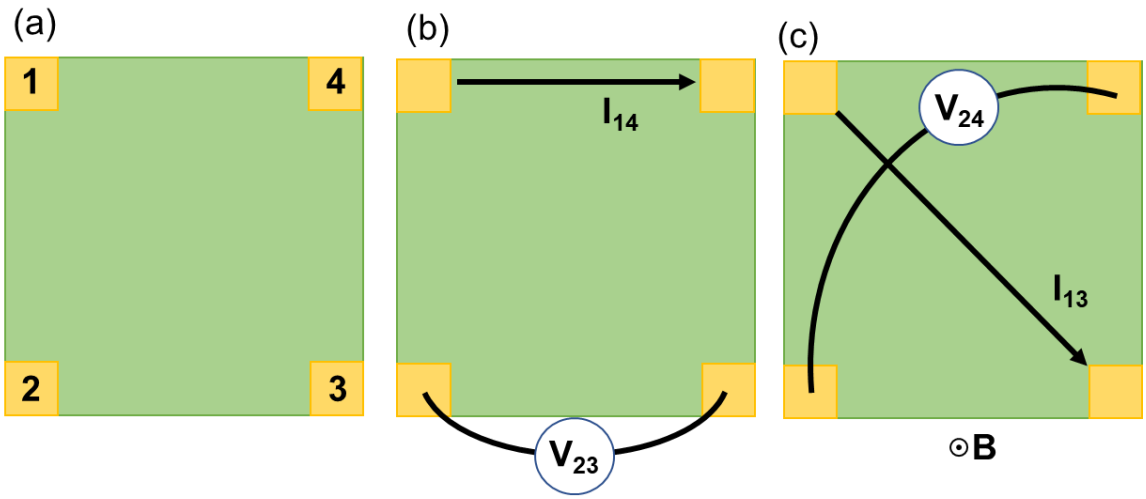

Figure 1.5 – Diagram of (a) van der Pauw geometry for performing Hall measurements on a square thin film sample with contacts labeled 1, 2, 3, and 4. Measurement setup for measuring (b) R_{xx} and (c) R_{xy} with a magnetic field B oriented out-of-plane.

(I_{14}) and measure the voltage drop between contacts 2 and 3 (V_{23}) (Fig. 1.5b), which gives $R_{xx} = V_{23}/I_{14}$. R_{yy} is then given by $R_{yy} = V_{43}/I_{12}$. The longitudinal resistances are then used to calculate the sheet resistance R_s using the van der Pauw equation:

$$e^{\left(\frac{-\pi R_{xx}}{R_s}\right)} + e^{\left(\frac{-\pi R_{yy}}{R_s}\right)} = 1 \quad (1.7)$$

Note that R_s can only be solved for analytically if $R_{xx} = R_{yy}$. If R_{xx} and R_{yy} differ slightly, Eq. 1.7 can be solved numerically typically using an average of R_{xx} and R_{yy} as an initial guess. If R_{xx} and R_{yy} differ strongly then the vdP method is not applicable. The transverse resistance R_{xy} is then measured by applying a current between two diagonal contacts (e.g. I_{13}) and measuring the voltage between perpendicular contacts (e.g. V_{24}) as a function of a magnetic field B applied perpendicular to the plane of the sample (Fig. 1.5c). The transverse voltage is a result of the Lorentz force on mobile carriers, and thus the sign of the voltage can distinguish between the type of majority carriers, i.e. holes or electrons. The Hall coefficient R_H is defined as:

$$R_H = \frac{V_{24}}{BI_{13}} = \frac{V_{31}}{BI_{24}} = \frac{R_{xy}}{B} \qquad (1.8)$$

The Hall coefficient can be used to calculate the sheet carrier density n_s:

$$n_s = \frac{1}{eR_H} \qquad (1.9)$$

which can then be used along with the sheet resistance to calculate the Hall mobility:

$$\mu_H = \frac{1}{en_s R_s} \qquad (1.20)$$

It should be noted that the Hall signal should be linear for single-carrier type properties to be assessed. Deviations from non-linearity can result from multiple carrier types being present, which will not be discussed here. However, experimental artifacts can also result in "non-linearity" that are purely noise. An example of this would be lack of temperature equilibration during temperature-dependent measurements. If the temperature distribution across a sample changes appreciably during the course of the *B*-field sweep, then this can result in a Hall coefficient that appears to vary as a function of *B*, but is actually the result of time-dependent thermal equilibration. Thus, care should be taken to ensure good thermal contact between the sample and the sample holder, and adequate dwell times at each temperature to ensure equilibration before performing the B-field sweep.

1.3 Molecular Beam Epitaxy

Many of the interesting physical properties exhibited by perovskite oxides (and other semiconductors in general) can be extremely sensitive to the presence of material defects. In the same way that various bulk crystal growth methods can result in differing quality of the resultant crystals as demonstrated by defect concentrations, different film growth methods can

be distinguished by their ability to suppress defect formation. Molecular beam epitaxy (MBE) is widely touted as the technique of choice for growing high-quality (i.e. low defect density) electronic thin films. One example of this is the extremely high low-temperature mobility exhibited by La-doped $SrTiO_3$ thin films grown by MBE, which reached as high as 53,000 cm^2 V^{-1} s^{-1} [61] compared to the highest reported for bulk single crystals of 22,000 cm^2 V^{-1} s^{-1} [32] and thin films grown by other techniques (6600 cm^2 V^{-1} s^{-1} by pulsed laser deposition) [62]. The sensitivity of carrier scattering to even small concentrations of defects makes low-temperature mobility (in semiconductors) an excellent metric for discerning materials quality.

In its most basic form, beams of atomic or molecular species impinge upon a heated crystalline substrate, upon which the crystalline film is grown. MBE utilizes an ultra-high vacuum (UHV) environment with background pressures in the $1\text{-}10 \times 10^{-10}$ Torr range or lower. The UHV leads to large mean free paths of free particles, such that the vapor-phase molecules of the source materials travel from source to growth surface without suffering from scattering and thus form well-defined "beams." The UHV also minimizes the adsorption of impurity species in the growing film, leading to highly pure films (the purity essentially becomes dependent on the purity of the source materials used). MBE is a low-energetic deposition method due to using thermal evaporation or sublimation of its source materials. Other thin film growth techniques, such as sputtering and pulsed laser deposition (PLD), impart a significant amount of excess kinetic energy to the species arriving at the growth surface, which can result in high concentrations of energetic point defects. The kinetic energy of the species used in MBE is orders of magnitude lower by comparison, and thus energetic point defects are minimized. The low energetic deposition also allows for sharp, atomically abrupt interfaces

between the substrate and film or between heterostructure layers, which might otherwise become roughened or intermixed via more aggressive deposition techniques [63].

The UHV environment also allows for the use of reflection high-energy electron diffraction (RHEED) during film growth. RHEED is a powerful *in situ* characterization tool that provides real-time information about the growing film. The most basic information provided by RHEED pertains to the growth morphology of the sample, such as whether it is growing as a two-dimensional (2D) planar film (streaks), as 3D islands (lattice spots), or if it is growing polycrystalline (rings) (Fig. 1.6). If the film grows in a layer-by-layer fashion (as opposed to step-flow), the intensity of the RHEED streaks will oscillate with the growth of each layer: one full oscillation corresponds to the growth of a single film layer. This information can be leveraged to extract the real-time growth rate of the film such that the thickness can be precisely controlled. Yet another useful application of RHEED is the observation of surface reconstructions, which are the appearance of higher-order reflection streaks that can appear due to reconstruction of surface dangling bonds. In certain materials systems, these can provide

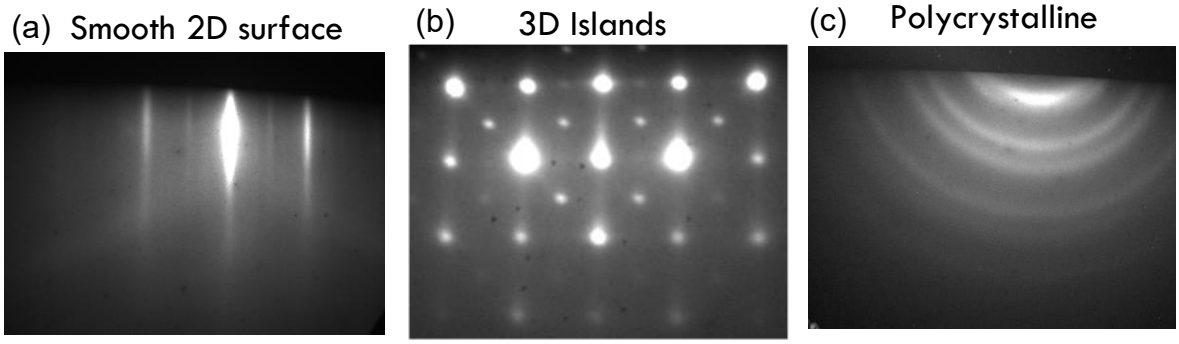

Figure 1.6 – Representative RHEED patterns indicating (a) a smooth 2D surface, (b) 3D island growth, and (c) polycrystalline rings

powerful *in situ* information about a growing film, such as its composition or the actual temperature (as opposed to the measured temperature).

For this work, two separate Veeco Gen. 930 MBE systems were utilized, affectionately termed the "Old Oxide" and the "New Oxide." Both systems are the same in general design and construction, and a generalized schematic is shown in Fig. 1.7. The systems differ by types of materials they are used to grow: the Old Oxide was used for the stannates and antiperovskites, and the New Oxide was used for the titanates.

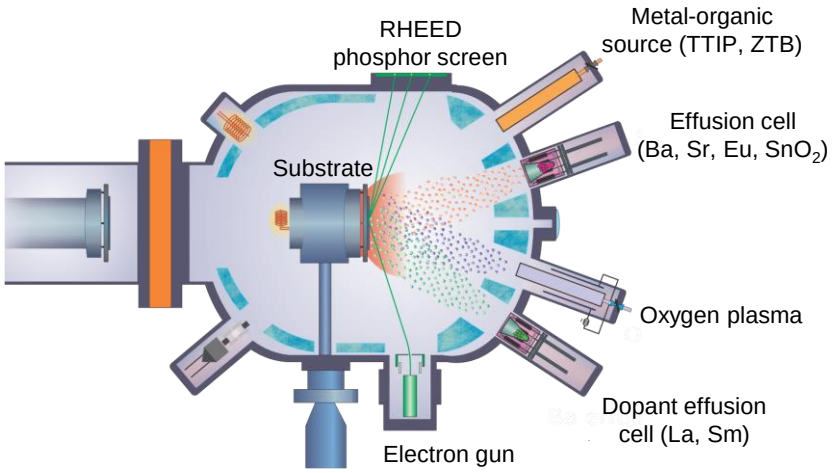

Figure 1.7 – Schematic of an MBE chamber used for perovskite oxide growth.

1.3.1 The Growth Window

The use of separate source fluxes to grow a compound semiconductor necessitates finding growth conditions under which the desired crystalline phase is formed without the formation of secondary unwanted phases. The primary growth condition tuning knobs in MBE are the temperature of the substrate, the absolute fluxes of the atomic or molecular species, and the relative composition of the fluxes being applied. Naively, a stoichiometric compound could be

expected to be grown by supplying the fluxes of the source materials in relative stoichiometric amounts. However, this would necessitate precise control of the flux beams, which in practice is extremely difficult. Any deviation of one or both of the fluxes during the course of a growth would result in the relative over- or under-incorporation of one of the species, which could result in nonstoichiometric defects or the formation of secondary phases. Luckily, the need for precise flux control can be avoided by exploiting thermodynamics to open a "growth window." The MBE growth window is range of growth conditions (substrate temperature, relative flux ratio, and absolute flux magnitudes) in which the (nominally) stoichiometric compound of interest coexists with the vapor phase of at least one of the constituents [64]. The existence of a growth window was a key factor in the success of early III-V semiconductor growth. Using GaAs as an example, this corresponds to a range of conditions in which a two-phase equilibrium consisting of the growing GaAs crystal and As vapor (i.e. under As "overpressure") is stable. Small fluctuations of the Ga flux are compensated by matching incorporation or desorption of As to and from the vapor, and small fluctuations of the As flux simply contribute to fluctuations in the vapor overpressure.

Growth windows (also called adsorption-controlled or self-regulating growth windows) naturally require that at least one of the species have a sufficient vapor pressure at viable growth temperatures and pressures. This is relatively easily accessible for III-V compounds where most group V elements are sufficiently volatile. For ternary oxides, however, the existence of an accessible growth window using solid elemental sources for the *A* and *B* metals is by no means guaranteed. Using $SrTiO_3$ as an example, when fluxes of Sr, Ti, and molecular oxygen (or a more activated form such as RF-plasma or ozone) are supplied, the oxygen (which of course is itself volatile) oxidizes the metals into SrO and TiO_2, which are then incorporated

into the film forming $SrTiO_3$. However, Sr nor Ti, nor their binary oxides SrO or TiO_2, have a reasonable vapor pressure at substrate temperatures below ~ 1500 °C [65], and thus any deviation from a precise 1:1 Sr:Ti flux ratio results in nonstoichiometric defects. Even the highest degree of flux control on the order of ~ 0.1 – 1% [66] would result in defect concentrations of 10^{20} cm^{-3} or higher.

1.3.2 Hybrid MBE for the growth of titanates

The use of a metal-organic (MO) precursor as a volatile Ti source has been shown to be extremely successful for the growth of high-quality $SrTiO_3$ [65,67]. The MO molecule titanium tetra-isopropoxide (TTIP) has the chemical formula $Ti(OCH(CH_3)_2)_4$ with a central Ti^{4+} bonded to four oxygen atoms (Fig. 1.8a), and has a high vapor pressure at viable substrate temperatures. Once adsorbed to the growth surface at elevated temperatures, is can decompose into TiO_2 and volatile organic byproducts which do not incorporate into the film in any appreciable amounts [68]. Above substrate temperatures of ~700 °C, the growth rate of TiO_2 using TTIP becomes limited by the desorption rate of TTIP from the surface (desorption-limited). It is in this regime of substrate temperatures that a growth window for $SrTiO_3$ using TTIP, Sr, and oxygen plasma sources is opened up, though the exact kinetics of the process once Sr is present are not precisely known [69,70]. A generalized schematic of the various processes occurring on and near the growth surface is shown in Fig. 1.8b**.** MBE using a combination of MO and elemental sources has thus become termed hybrid MBE.

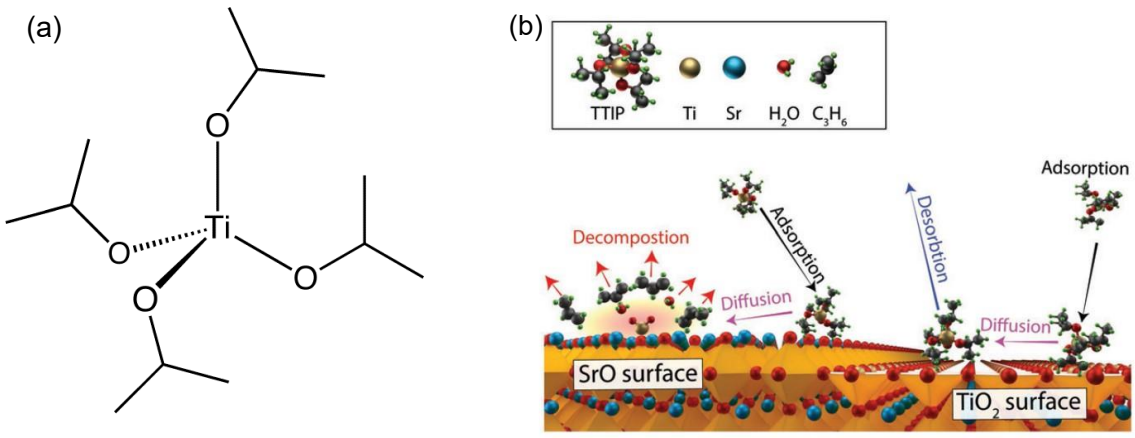

Figure 1.8 – (a) schematic structure of the TTIP molecule. (b) Schematic of the various surface kinetic processes of TTIP on a SrO terminated plane (left) and a TiO_2 terminated plane (right) of a $SrTiO_3$ (001) surface showing adsorption, diffusion, desorption, and decomposition. Adapted with permission from ref. [69].

The stoichiometry of the films can be determined by lattice parameter measurements, which are sensitive to nonstoichiometric defects and are known to expand regardless of whether conditions are Ti-rich or Sr-rich [65,67]. Using these measurements, the growth window could be established for a particular substrate temperature as a range of TTIP/Sr flux ratios within which stoichiometric films are grown. As substrate temperature is increased, the width of this flux ratio range widens [65], i.e., the growth window "opens." Under certain conditions, the stoichiometry of the film can be identified *in situ* by surface reconstructions observed via RHEED [71]. The excellent stoichiometry control afforded by TTIP combined with the low energetics of MBE contributed to the growth of films with the highest low-temperature mobility reported for $SrTiO_3$ of any form, as mentioned above [61]. The ferroelectric transition of strained $SrTiO_3$ films on LSAT substrates was also found to be sensitive to nonstoichiometric defects as told by second harmonic generation (SHG) [72].

Films grown using TTIP/Sr ratios which were outside of the stoichiometric window on both the Ti-rich and Sr-rich sides did not exhibit signs of a ferroelectric transition.

Initial hybrid MBE growth of $SrTiO_3$ utilized a co-supply of activated oxygen plasma along with TTIP and Sr, though it was later found that the additional oxygen is not necessary to grow high-quality $SrTiO_3$ [73], which is attributed to the ability of TTIP to also supply oxygen as well as Ti. The central Ti^{4+} cation comes bonded to 4 O^{2-} anions (Fig. 1.8a). The co-supply of oxygen mainly serves to minimize a small degree of oxygen vacancies [74], though these can generally be filled by a post-growth annealing treatment in air. The ability for adequate oxygen to be supplied without creating an extremely oxidizing environment has aided in the growth of rare-earth titanate materials such as $GdTiO_3$ [73], where the valence states are $Gd^{3+}Ti^{3+}(O^{2-})_3$. The Ti^{4+} state is favored oxidizing conditions, which can lead to the unintentional growth of a pyrochlore phase instead of the perovskite phase. TTIP has allowed for the growth of a wide variety of other perovskite titanates, including $BaTiO_3$ [75], $EuTiO_3$ [76], $SmTiO_3$ [77] and others.

1.3.3 SnO_2 source for Stannates

The growth of perovskite stannates ($ASnO_3$) by MBE also found difficulty in using elemental metal sources. Some limited success was achieved using metallic Sn and Ba sources along with ozone as an oxidant [78], but the mobility in these films was on par with PLD-grown films indicating that they contained a relatively high amount of point defects. At first glance, accessing a growth window using metallic Sn and an oxidant should be viable as one of the constituent oxides, SnO, is highly volatile. However, the hindrance lies in the fact that

Sn is difficult to oxide and readily reduces in the UHV environment, forming metallic Sn droplets on the surface [79,80]. Following from the success of TTIP for titanates, attempts were made to grow $BaSnO_3$ using an analogous MO that contains Sn, tin tert-butoxide (SnTB). However, SnTB was found to be thermally unstable and decomposed before reaching the growth chamber [81]. An alternative MO source, hexamethylditin (HMDT), has been used to successfully grow $BaSnO_3$ and $SrSnO_3$ [81,82]. Due to the lack of oxygen in the HMDT, a co-supply of oxygen (in this case oxygen plasma) is needed. However, mobilities in $BaSnO_3$ films grown with HMDT are below that which can be achieved with other sources (described below), and it is speculated that the absence of sufficient oxidation from the MO itself could contribute to this.

The successful growth of high-quality La-doped $BaSnO_3$ films with room-temperature mobilities exceeding 140 $cm^2\ V^{-1}\ s^{-1}$ was first demonstrated by Raghavan *et al* at UCSB by utilizing solid SnO_2 as a Sn source [80]. SnO_2 sublimates in UHV environments as ~77% SnO and ~21% O_2, and the remainder is constituted of various suboxides (Fig. 1.9) [83]. Thus, Sn is provided in a pre-oxidized form, and an adsorption-controlled growth window could be accessed due to the volatility of SnO, within which the highest mobility films could be grown. It was initially believed that a rather significant co-supply of additional oxidant (either oxygen plasma [80] or ozone [84]) was still necessary along with the SnO_2 source due to known low oxidation potential of Sn. This will be further explored in Chapter 2.

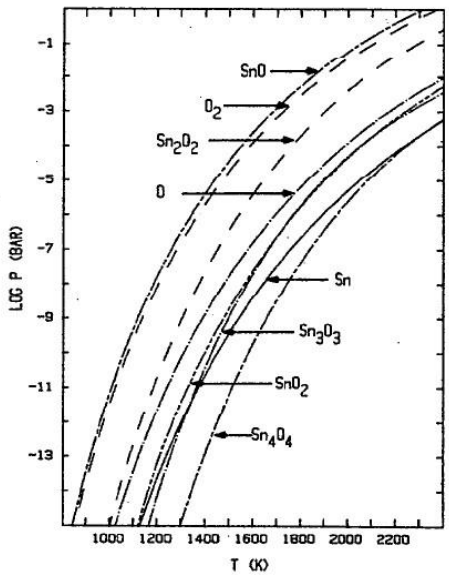

Figure 1.9 – Partial pressures of the various molecular species formed under congruent vaporization conditions of SnO_2. Adapted with permission from ref [83]

1.3.4 Epitaxial strain in films

The choice of substrate can have important effects on the epitaxial film. Unless the film is homoepitaxial (i.e. the film is the same material as the substrate) there will in all likelihood be some degree of mismatch between the lattice parameter of the film and the lattice parameter of the substrate, which will induce strain in film. The lattice misfit strain is given as $\varepsilon_m = \frac{a_{sub}-a_{film}}{a_{film}} \times 100\%$, where a_{sub} and a_{film} are the cubic (or pseudocubic) lattice parameters of the substrate and film, respectively. The biaxial strain imposed by the substrate translates into stress in the growing film, which becomes greater as the film grows thicker. If the stress becomes too great, the film will relax via the introduction of misfit dislocations to relieve some of the stress, and thus the film will no longer be coherently strained to the substrate. The critical stress at which this relaxation occurs translates into a critical thickness h_c. The Matthews-

Blakeslee (MB) formula for critical thickness can be used to estimate this thickness, which is given as:

$$h_c = \frac{1}{\varepsilon_m(1+\upsilon)}\frac{|b|}{8\pi\cos\lambda}(1-\upsilon\cos^2(\beta))\ln\frac{\alpha h_c}{|b|} \qquad (1.21)$$

where ν is Poisson's ratio, $|b|$ is the magnitude of the Burgers vector, λ is the angle between the dislocation line and the film/substrate interface, β is the angle between the Burgers vector and the dislocation line, and α is a cutoff parameter. This critical thickness represents the thickness at which the elastic strain energy released by the introduction of a misfit dislocation is equivalent to the energy increase introduced by the creation of the dislocation. We will use $SrTiO_3$ (a = 3.905 Å) grown on LSAT (001) (a = 3.868 Å) as an example, for which the misfit strain ε_m = -0.95% (compressive strain). For a cubic perovskite oxide oriented in the [001] direction, we will assume the active slip system to be $\{101\}\langle 10\bar{1}\rangle$ [85], thus making λ = 45°, β = 90°, and $|b|$ = 5.52 Å. Poisson's ratio ν can be approximated to be ~0.3, and the cutoff parameter α is 4 [85]. This gives a critical thickness h_c of ~12 nm. However, fully strained films of $SrTiO_3$ on LSAT can be grown as thick as ~200 nm [86]. This demonstrates that while the MB formula may accurately estimate h_c in certain situations, it can severely underestimate it in others. This can be attributed in part to the fact that strain relaxation via the nucleation and propagation of dislocations is a kinetic process, and thus certain kinetic barriers which are not accounted for in the equilibrium free energy minimization may contribute to larger h_c's. The relaxation process is complex, and it is difficult to derive an exact analytical equation which can accurately capture and describe all of the relevant factors, if not impossible. In practice, it is common for strained $SrTiO_3$ films grown to thicknesses above ~150 nm to experience strain relaxation, whereas others grown under identical conditions to nearly identical thicknesses

could grow fully strained. This highlights the fact that there is a certain degree of stochasticity to achieving thick, fully strained films above the thermodynamic critical thickness. However, general trends can still be assumed based on how the kinetics of dislocation nucleation and propagation might be affected [64]. For instance, a higher growth temperature would be more likely to induce relaxation than a lower one due to enhanced dislocation motion. A higher concentration of point defects (i.e. doping or alloying) can serve as catalysts or stress concentrators for dislocations in the lattice, which can also lead to a higher propensity for relaxation. It should be noted, however, that for very large strains (i.e. > 2%), the critical thickness is extremely thin, and films grown with this degree of mismatch can be almost guaranteed to grow relaxed, as is the case with $BaSnO_3$ due to its lack of a lattice-matched substrate.

1.4 Outline

This thesis is organized in three main chapters, each which concerns a different perovskite materials system. Due to the widely different properties exhibited by each of the materials being studied, each chapter will begin with a few sections of additional background information that is specific to the material system in question. Chapter 2 details various growth studies of the high mobility oxide $BaSnO_3$. Chapter 3 describes very early efforts to grow and characterize the 3D Dirac oxide Sr_3SnO antiperovskite films, including techniques to deal with the strong air sensitivity. Chapter 4 describes a study of the evolution of ferroelectricity and superconductivity in Eu-alloyed $SrTiO_3$ films with increasing amounts of magnetic Eu.

In Chapter 2, past work in growing thin films of $BaSnO_3$ are briefly described to illustrate the difficulty in achieving thin film mobilities that are on par with single crystals. Three distinct growth studies are then presented. In the first, various attempts are made to fabricate $BaTiO_3/BaSnO_3$ heterostructures to investigate the plausibility of such structures for high power density field effect transistors. In the second study, two anecdotal growths on lattice matched substrates are described, which do not constitute a formal study but the insights gained from each highlight the sensitivity of mobility in $BaSnO_3$ to factors beyond just dislocations. In the third study, $BaSnO_3$ films are grown under different oxidant conditions, and lattice parameter measurements reveal a relatively high concentration of Sn_{Ba} antisite defects in all films regardless of oxidant conditions. This highlights the difficulty in oxidizing Sn in MBE environments and may provide an additional reason why film mobilities are so low relative to single crystals.

In Chapter 3, previous experimental work in the synthesis and characterization of various antiperovskite oxides is briefly described to provide context for the present study. Then, the preliminary steps leading to the first attempts at growing Sr_3SnO by MBE at UCSB are described, which had very limited previous reports of growth in the literature. A scheme for protecting the extremely air-sensitive films using a capping layer deposited *in situ* is also developed. This work served as the groundwork for continued work by another student, Wangzhou Wu, who further improved growth conditions and electrically characterized the films [87,88].

In Chapter 4, a brief review of superconductivity and ferroelectricity in $SrTiO_3$, with particular focus placed on where the two properties intersect, is provided to serve as background for the tentative argument that the superconductivity in $SrTiO_3$ may at least to

some degree depend on the presence of broken inversion symmetry. Then, a study of strained films of highly Eu-alloyed $SrTiO_3$ (i.e. $Eu_xSr_{1-x}TiO_3$) is presented which seeks to further explore the apparent insensitivity of the superconductivity in $SrTiO_3$ films to magnetic impurities. It is found that the Eu alters the polarizability of the $SrTiO_3$ lattice such that a global ferroelectric ground state is no longer favorable and instead leads to a crossover to a relaxor-like state with locally polar domains. It is this structural change which may lead to the eventual suppression of superconductivity.

Chapter 5 summarizes the results of this thesis and provides possible future research directions that arise from the results.

1.5 Permissions and Attributions

Chapter 2. $BaSnO_3$

The discovery of record-high room-temperature mobility of 300 $cm^2\ V^{-1}\ s^{-1}$ in single crystals of La-doped $BaSnO_3$ motivated a significant amount of research into attempting to grow this material as a thin film. The combination of high mobility at high carrier densities makes it a promising candidate for power electronics purposes, in addition to the fact that it is a transparent conducting oxide. However, achieving mobilities in thin films that are on par with those of single crystals has so far not been successful. Not least among the limitations imposed by thin films is the lack of a lattice-matched substrate for $BaSnO_3$, which means growths on commercially available substrates will experience relaxation and induce mobility-limiting dislocations. Nonetheless, mobilities in films has reached as high as 170 – 180 $cm^2\ V^{-1}\ s^{-1}$ at room temperature, which still vastly outperforms other perovskite oxides and indeed many degenerately doped semiconductors in this carrier density range of ~ 1-10 × 10^{19} cm^{-3}. These highest film mobilities, which contain relaxation-induced dislocations, were enabled by the successful growth via MBE using a solid SnO_2 source as originally developed at UCSB. Much of the groundwork for growing high-mobility films had been laid by the time I began growing $BaSnO_3$, and thus my work presented here serves as a continuation of the techniques and ideas developed by previous group members.

Though the mobilities achieved via MBE with SnO_2 vastly outperforms those achieved via other thin film growth methods, inconsistency and growth condition sensitivity has become very apparent through the hundreds of growths that had been performed both prior to my work and while I was involved. Regardless of this, the limited but still impressive mobilities that had been displayed in thin films motivated a collaboration with Prof. Siddharth Rajan and his group at the Ohio State University to grow prototypical heterostructures for exploring high power density devices. For my part, I grew heterostructures of $BaTiO_3/BaSnO_3$ which utilize the high polarizability of the $BaTiO_3$ to mitigate high peak electric fields that result from a highly doped $BaSnO_3$ channel. I will also present some very limited growths on lattice-matched substrates, which do not exhibit vast improvements in mobility even though no dislocations were induced via relaxation. Finally, through a somewhat accidental discovery, it is found that La-doped $BaSnO_3$ films can be grown using only La, Ba, and SnO_2 sources. Using this insight along with investigations of the out-of-plane lattice parameter, it is posited that a significant amount of Sn_{Ba} antisite defects exist in even the highest-mobility MBE-grown films. This finding supports the known difficulty in oxidizing Sn in a vacuum environment, and may place an upper limit on the mobility that can be achieved in films even if a lattice matched substrate is made widely available, unless a more-oxidizing growth method can be found.

2.1 Introduction

2.1.1 Past Work

Following the discovery of high room-temperature mobility at high carrier densities in single crystals, attempts to grow films of high mobility $BaSnO_3$ soon followed. Due to the large lattice parameter (4.116 Å), it was immediately realized was that there lacked a

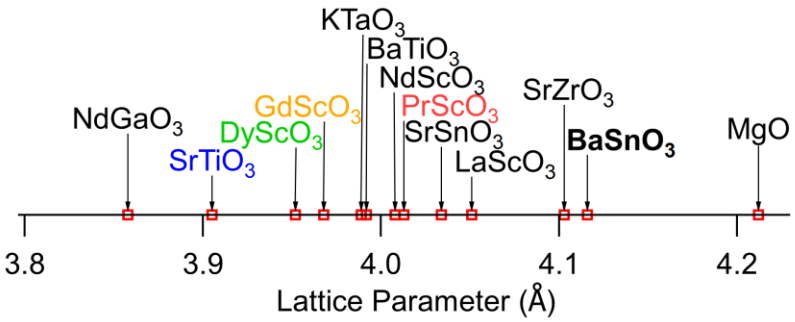

Figure 2.1 – Comparison of room temperature cubic or pseudocubic lattice constants of various perovskite oxides. The materials written in color are commercially available substrates used for $BaSnO_3$ growth.

commercially available substrate which is closely lattice-matched to $BaSnO_3$ (i.e. < 2% mismatch) (Fig. 2.1**)**, and the excessive compressive strain would cause films to relax, introducing misfit dislocations which can harm the mobility. Regardless of this and with the promise that perhaps a lattice-matched substrate could eventually become commercially viable, film growth was attempted on lattice mismatched substrates in efforts to achieve the highest mobility possible in the presence of misfit dislocations.

Most early attempts to grow films of doped $BaSnO_3$ utilized pulsed laser deposition (PLD) [6,91,92] or sputtering [93]. These are highly energetic deposition methods which can introduce high concentrations of energetic point defects, degrading the mobility. Perhaps owing to the thermal stability of $BaSnO_3$, post-growth annealing techniques are limited in their ability eliminate these defects once they are locked in during growth. The rather significant effect of these energetic point defects on μ is illustrated by the study by Lee *et al* [91], which utilized insulating $BaSnO_3$ crystals as substrates for the PLD growth of their La-doped $BaSnO_3$ films (being the same group who originally reported the single crystal growth [6]). The homoepitaxial substrate allows for growth without strain relaxation and thus no misfit

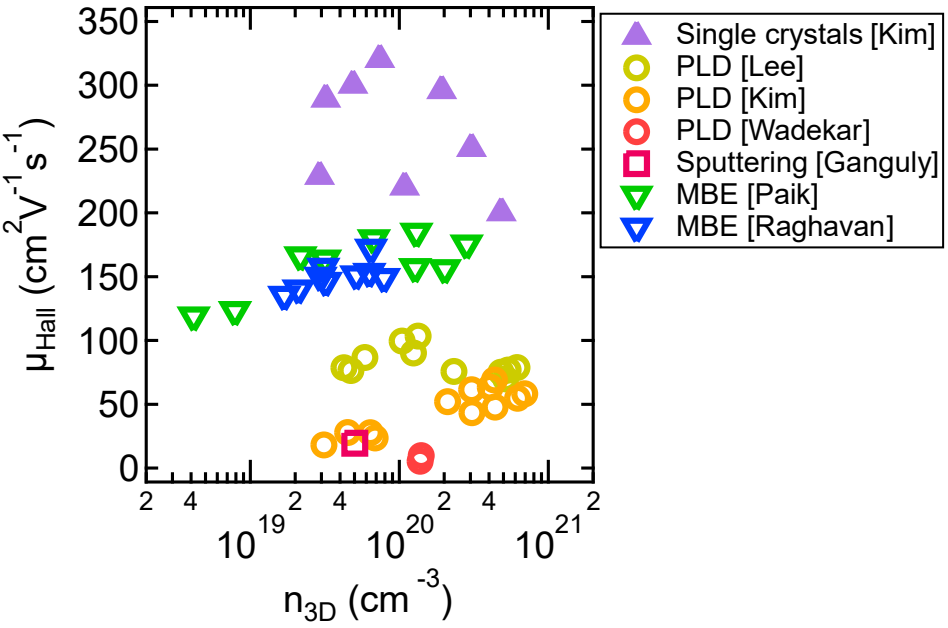

Figure 2.2 - Comparison of selected maximum room temperature Hall mobilities μ_{Hall} measured with varying carrier densities n_{3D} for different film growth methods and single crystals. Data from reports from literature [7,80,84,91–93]**.**

dislocations. However, the maximal room-temperature mobility was limited to below ~ 100 $cm^2\ V^{-1}\ s^{-1}$. This indicates that energetic point defects in these concentrations are the primary limiter of mobility (Fig. 2.2).

As mentioned in section 1.3.3, MBE growth of La:$BaSnO_3$ films using SnO_2 as the Sn source enabled the highest room-temperature mobilities reported in thin films [80,84]. These films were grown relaxed on a variety of substrates using either ozone (10% + O_2) [84] or oxygen RF-plasma [80]. The highest reported room-temperature mobility of La:$BaSnO_3$ grown using oxygen plasma was originally 150 $cm^2\ V^{-1}\ s^{-1}$, grown on $PrScO_3$ (110) (-2.2% mismatch). However, this was later raised to 172 $cm^2\ V^{-1}\ s^{-1}$ grown on $DyScO_3$ (110) (-4%) by using a ~10 nm thick unintentionally doped (UID) buffer layer for a ~30 nm La-doped film (not reported). The UID layer places the active layer further from the substrate, avoiding the

area of the film with the highest concentration of misfit dislocations. The highest reported room-temperature mobility of thin-film La:$BaSnO_3$ is 184 $cm^2 V^{-1} s^{-1}$ grown on MgO (+ 2.3%) and can be attributed to the use of an excessively thick UID buffer layer of 150 nm [58]. Thus, for MBE-grown $BaSnO_3$ films, the maximal mobility appears to be limited by the relaxation induced by lattice mismatched substrates. However, this will be challenged in later sections.

2.1.2 MBE growth and experimental methods

Following the pioneering work using SnO_2 as the Sn source for MBE-grown $BaSnO_3$ at UCSB, my work served as a continuation of the efforts to investigate ways to further improve the mobility of thin films, as well as to explore $BaSnO_3$-based heterostructures for possible power electronics applications. Previous group members had established a growth procedure through numerous growth campaigns which generally resulted in high mobilities (~150 $cm^2 V^{-1} s^{-1}$ or higher) once growth conditions were calibrated. This general procedure will be described below, and can be assumed to have been followed for all the growths presented in the subsequent sections unless otherwise specified.

Substrates used for growth were typically 5 mm × 5 mm × 0.5 $DyScO_3$ (110) or (001), which were essentially equivalent in their surface-plane lattice constants of ~3.94 Å and mismatch of ~ -4%. These were more readily available than a slightly more lattice matched substrate $PrScO_3$ (~ -2.2%). As these are wide band gap oxides which do not readily absorb radiative heating, the substrates are backed with 200-300 nm of Mo, which allows for sufficient growth temperatures to be achieved while also being sufficiently oxidation resistant to withstand the growth conditions [94].

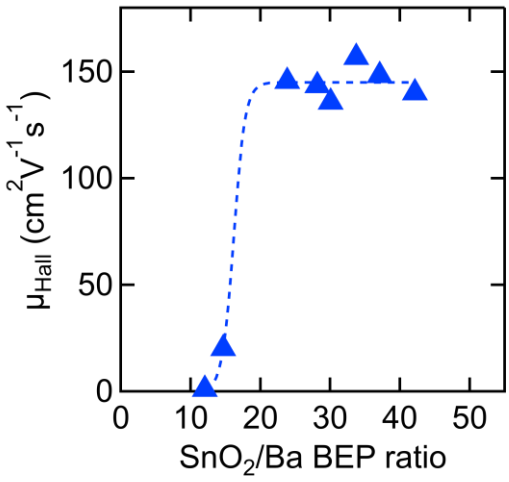

Figure 2.3 - Representative growth calibration curve showing room temperature Hall mobilities μ_{Hall} as a function of SnO_2/Ba beam flux ratio used for each sample.

Flux calibration measurements for the Ba and SnO_2 source cells were performed overnight prior to each growth day to establish the beam equivalent pressure (BEP) as a function of cell temperature. Relatively high SnO_2/Ba flux ratios are needed to produce the highest mobility films (Fig. 2.3**)**. Going towards more Ba-rich conditions produces a precipitous drop-off in mobility, and very quickly leads to insulating films. Going towards more SnO_2-rich conditions, the mobility appears to plateau, which gives merit to the argument that an adsorption-controlled growth window exists under excess flux of volatile SnO. Calibration growths were carried out at the beginning of all growth campaigns to establish the range of SnO_2/Ba flux ratios that produced high-mobility films (which could shift between campaigns). Growth rates were limited by the Ba flux, as would be expected for adsorption-controlled growth. However, when changing the flux ratio between growths, it was found that changing the temperature of the SnO_2 cell produced more inconsistencies than using an approximately constant SnO_2 flux and

changing the Ba flux. This would inevitably affect the growth rate, but this could be compensated by changing the growth time and La dopant cell temperature to keep the carrier density in the ~ 1 – 10 × 10^{19} cm^{-3} range.

The substrate was heated to the growth temperature and allowed to anneal for ~10 minutes prior to growth. Typical growth temperatures were in the 750-850 °C range, measured by a thermocouple behind the sample as well as an infrared pyrometer. It was found that more consistency in growth quality resulted from using constant output power of the sample heater during growth rather than using temperature control. The measured temperature of the film would drift somewhat during growth, in part thought to be due to the partial oxidation of the backing metal [94,95].

In addition to Ba, SnO_2, and La, activated oxygen RF-plasma was also used as an oxidant source. High-purity oxygen is introduced to the chamber via a linear leak valve (LLV), and the plasma was produced by a RF-plasma generator at the inlet to the chamber (300W power), which produced a BEP of ~1 × 10^{-5} Torr. Prior to growth, the substrate was subjected to a 20-minute plasma anneal following the initial 10-minute anneal. Growth would proceed directly following the plasma anneal by opening the Ba and SnO_2 shutters, keeping the plasma conditions the same as used during the anneal. The growth was monitored *in situ* via RHEED. Strongly Sn-rich or Ba-rich conditions produced spotty RHEED patterns indicating rough, 3D surfaces. For all the growths I performed, RHEED intensity oscillations were never observed. Streaky RHEED patterns were indicative of "good" growth conditions, though both insulating and high mobility films could exhibit very similar RHEED patterns, and thus RHEED was only a first-order check. Typical growths consisted of a UID buffer layer of approximately 1/3 the total film thickness. The La shutter was opened at approximately 1/3 the total growth time

to dope the top 2/3 of the film. Total film thicknesses are generally ≥ 35 nm, which is sufficiently thick for achieving mobilities of 150 $cm^2\ V^{-1}\ s^{-1}$ [80]. After growth, cooling the samples down under the oxygen plasma was found to have minimal effect.

Once removed from the growth chamber, the samples were annealed in an oxygen atmosphere at 900 °C for 10 minutes to suppress oxygen vacancies using a rapid thermal annealer (RTA). The film structure was characterized by XRD to assess out of plane lattice parameters (a_{op}) and film crystallinity. Laue thickness fringes were commonly observed, indicating relatively good crystalline quality, and were used to determine the film thickness. In general, it was found that the post-growth oxygen anneal could improve the crystallinity of the film as told by sharpening (or simply the appearance) of Laue fringes following the anneal. 50nm Ti / 300nm Au ohmic contacts were deposited via electron beam evaporation on the corners of the sample, and room-temperature Hall measurements were performed in a vdP geometry to assess carrier densities and mobilities.

2.1.3 Sample Variability

Finally, a note on sample quality and variability. The studies presented here consist of a very small percentage of the total amount of growths performed, due to the observed need for almost constant calibration of the growth conditions. Calibrations were performed to find conditions which produced the highest mobility of films, and these conditions would then be replicated with minor tweaks for the particular study in question. It is common for films grown under nearly identical growth conditions within the same growth campaign to exhibit mobilities which might differ by 20-30 $cm^2\ V^{-1}\ s^{-1}$. Thus, “good” growth conditions were

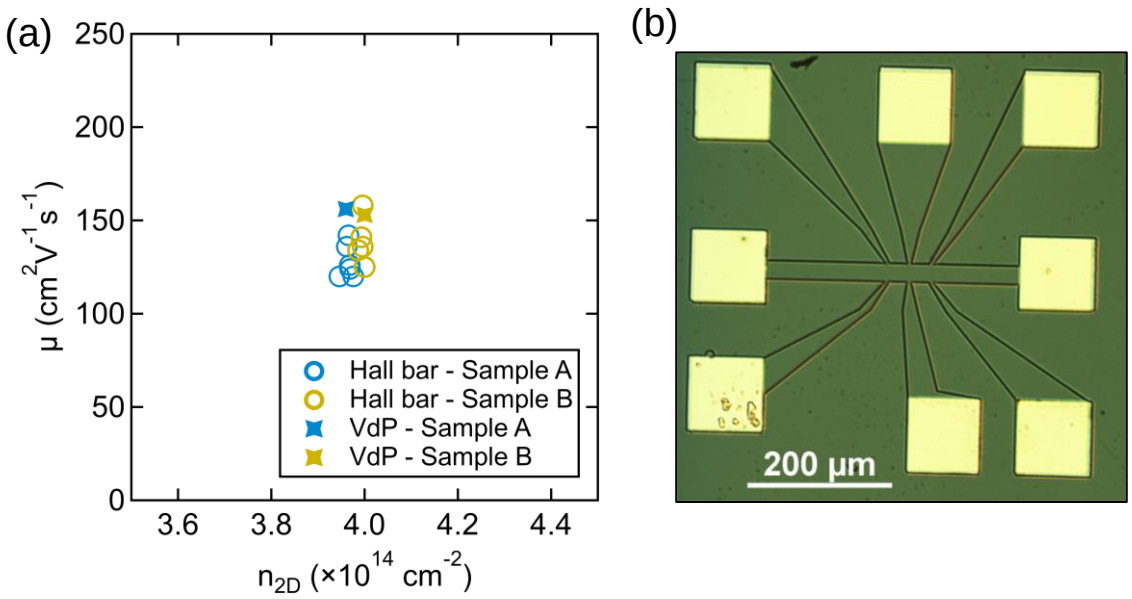

Figure 2.4 - (a) Hall mobilities and sheet carrier densities extracted from Hall bars fabricated on two different films. The mobility and sheet carrier density (n_{2D}) measured via Van der Pauw (VdP) technique prior to Hall bar fabrication is also shown. (b) Optical micrograph of a $BaSnO_3$ Hall bar. Adapted with permission from ref. [89].

generally defined as those which could consistently produce films with mobilities above 120 $cm^2\ V^{-1}\ s^{-1}$. Mobilities were usually measured via vdP contacts, which essentially represent the "average" properties of the entire film. To investigate the possible source of this apparently random sample-to-sample variability, Hall bar structures were fabricated on two samples and the mobility and carrier density measured individually for each Hall bar. The resulting measurements are shown in Fig. 2.4. As can be seen, while the sheet carrier density n_{2D} only varies by a small amount among the different devices, the mobility takes values in a range of 50 $cm^2\ V^{-1}\ s^{-1}$. This indicates relatively significant sample nonuniformity, and this is likely a common feature to all or most $BaSnO_3$ films.

In theory, finding high mobility growth conditions would correspond to finding conditions which produced "stoichiometric" films, as nonstoichiometric defects are known to diminish mobility, and thus finding conditions of maximal mobility should correspond to the most stoichiometric conditions. For many other perovskite systems, stoichiometry can be elucidated via a_{op} lattice parameter measurements, as is done for $SrTiO_3$. $BaSnO_3$ films were consistently fully relaxed, which eliminates residual strain as a component and thus the a_{op} should match the bulk stoichiometric value of 4.116 Å for nominally stoichiometric growth conditions. However, a_{op} measurements were routinely found to follow no observable trend whatsoever, neither with cation flux ratio nor with measured mobility. Additionally, many lattice parameters were found to be *below* the bulk, stoichiometric value. This is extremely uncommon as, for most perovskite oxides, non-stoichiometric defects tend to cause only lattice *expansions*, not contractions. A more complete collection of measurements illustrating this lack of trend can be found in ref. [95]. A trend of a_{op} with cation flux ratio and mobility could be better observed once the oxygen plasma was removed from growth, described in detail in Section 2.4. Thus, it is possible that the use of the high oxygen pressure in the 1×10^{-5} Torr range – which is quite high for MBE growths – could have contributed some of the variability, though the reason is not well-understood.

Other sample inconsistencies could be seen in the presence of SnO_2 peaks in XRD and the degree of surface deposits seen in atomic force microscopy (AFM). Neither of these appeared to have any direct correlation with the mobility of the film, and no clear trend in why they would be more strongly observed in one sample and not the next could be established either. The most general trend was that SnO_2 peaks could appear in films which utilized the highest SnO_2/Ba flux ratios, though not always. It is most likely that the surface deposits seen in AFM

measurements were SnO_2, though films with a high degree of surface deposits did not always exhibit SnO_2 peaks in XRD, and vice versa. In any case, it is extremely unlikely that the SnO_2 exists as a secondary phase *within* the film, but rather formed on the surface after growth had finished (perhaps once exposed to air, as post-growth RHEED did not indicate the presence of such 3D-like features).

2.2 $BaTiO_3/BaSnO_3$ Heterostructures

The promise of a high-mobility channel material which can also be highly doped makes $BaSnO_3$ a promising candidate for high-power and high-frequency field-effect transistor (FET) devices, as the combination of these two properties mean you can put a significant amount of charge carriers into the channel and then move them around with relative ease. However, extremely high peak fields can develop on the drain side of the gate in high carrier density devices like these, which can lead to dielectric breakdown. This effect can be mitigated by the use of a high-k dielectric under the gate, which serves to smooth out these lateral fields [9,96]. $SrTiO_3$ and $BaTiO_3$ were identified as excellent candidates for this purpose due to their relatively low mismatch with $BaSnO_3$ (~ -5.4% and ~ -3%, respectively) and high dielectric constants (~250 for $SrTiO_3$, and $BaTiO_3$ is ferroelectric).

Prior $BaTiO_3/BaSnO_3$ heterostructures had been grown by Chris Freeze and sent to collaborators in Prof. Siddharth Rajan's group at the Ohio State University (OSU) for device fabrication [95]. For these samples, the $BaSnO_3$ layer was grown, removed from the chamber, characterized, and then a diced section of the film (to remove areas with metal contacts) was loaded back into the MBE growth chamber for deposition of 20 nm of $BaTiO_3$. For some of

these heterostructures, the $BaTiO_3$ had difficulty wetting the surface of the $BaSnO_3$, as described in ref. [95]. It was also found that the gates were extremely leaky, even for relatively well-coalesced $BaTiO_3$ layers. Thus, it was believed that some of the gate leakage could be attributed to interfacial defects between the $BaSnO_3$ and $BaTiO_3$, which may have formed as a result of exposing the $BaSnO_3$ surface to ambient air before $BaTiO_3$ deposition. Regardless of the leaky gates on some of these devices, some promising results were published which exhibited record high current densities of a $BaSnO_3$-based FET device [97,98].

2.2.1 Growth and characterization of $BaTiO_3/BaSnO_3$ heterostructures

In order to reduce possible interfacial defects, heterostructures would be grown by growing the $BaTiO_3$ directly after the $BaSnO_3$ layer without breaking vacuum. Before growing the heterostructures, both $BaSnO_3$ and $BaTiO_3$ growth conditions were calibrated. The $BaTiO_3$ was grown using a flux of Ba, TTIP, and oxygen plasma, at a substrate temperature of around 800 °C. $BaTiO_3$ growth conditions were calibrated by XRD a_{op} measurements. For the $BaSnO_3$ layer, the target sheet carrier density requested by the OSU team was $n_{2D} < 4 \times 10^{14}$ cm^{-2} for a ~30 nm thick film such that the channel could be effectively pinched off if the heterostructure synthesis was successful. At the time, the highest achievable mobility for this relatively low carrier density was found to be 112 $cm^2 V^{-1} s^{-1}$ at a carrier density of 3.7×10^{14} cm^{-2}. The AFM and XRD for this calibration sample are shown in Fig. 2.5. A small SnO_2 peak can be seen in XRD, and the surface exhibited SnO_2 deposits. Immediately following the growth of this calibration sample, a series of $BaTiO_3/BaSnO_3$ heterostructures were grown. Three heterostructures were grown with different thickness of the doped layer to see the effects this

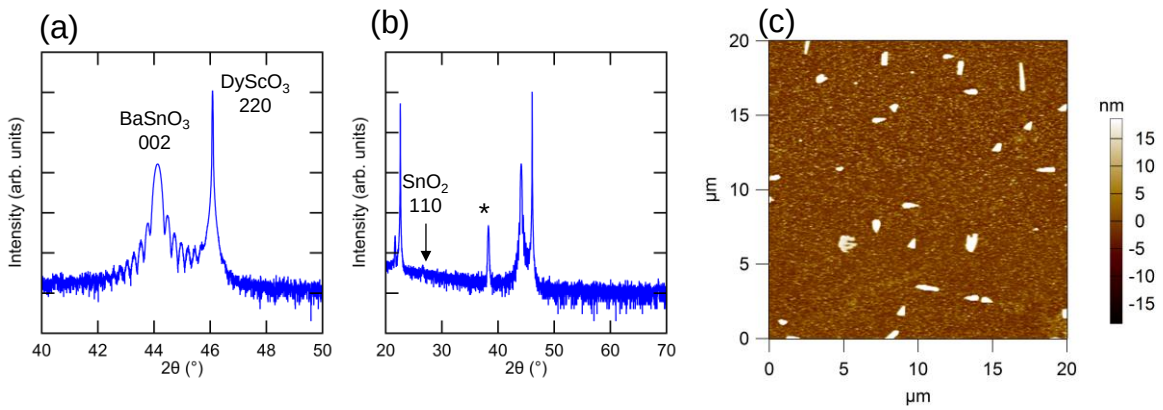

Figure 2.5 – (a) XRD scan around the $BaSnO_3$ 002 and $DyScO_3$ 220 substrate peak. (b) wide-angle scan of the calibration sample, showing a peak from the contact (indicated by a *) and a small SnO_2 110 peak. (c) AFM of the surface of the calibration sample, showing surface deposits.

would have for the FET devices: doped thicknesses of the top 2/3, 1/2, and 1/3 of the total thickness for samples A-C, respectively. The 3D doping density was kept constant, thus effectively reducing the total sheet carrier density as the doped thickness was lowered. These heterostructures were grown in succession, and RHEED was nominally normal for all heterostructures.

Fig. 2.6 shows XRD and AFM for heterostructures A-C. Sample A exhibits relatively nice thickness fringes of the $BaSnO_3$ layer after annealing, and small SnO_2 peaks, which also appear in the calibration sample. Samples B and C, however, exhibit additional phases not seen in the calibration samples. The rather broad peak near 40 °2θ could be attributed to a $BaO_2 \cdot 8H_2O$ hydroxide phase, which has been seen before in $BaSnO_3$ films, however, generally only in extremely Ba-rich conditions [94]. The other peak at around 30 °2θ could possibly belong to a misoriented $BaSnO_3$ 110 peak, which has also been seen in samples grown at too-low growth temperatures [94]. The $BaSnO_3$ 110 peak was completely suppressed in both samples after the 10-minute oxygen anneal. The $BaO_2 \cdot 8H_2O$ peak was fully suppressed after the oxygen anneal in Sample C, but only partially suppressed in sample B. While the surfaces of all

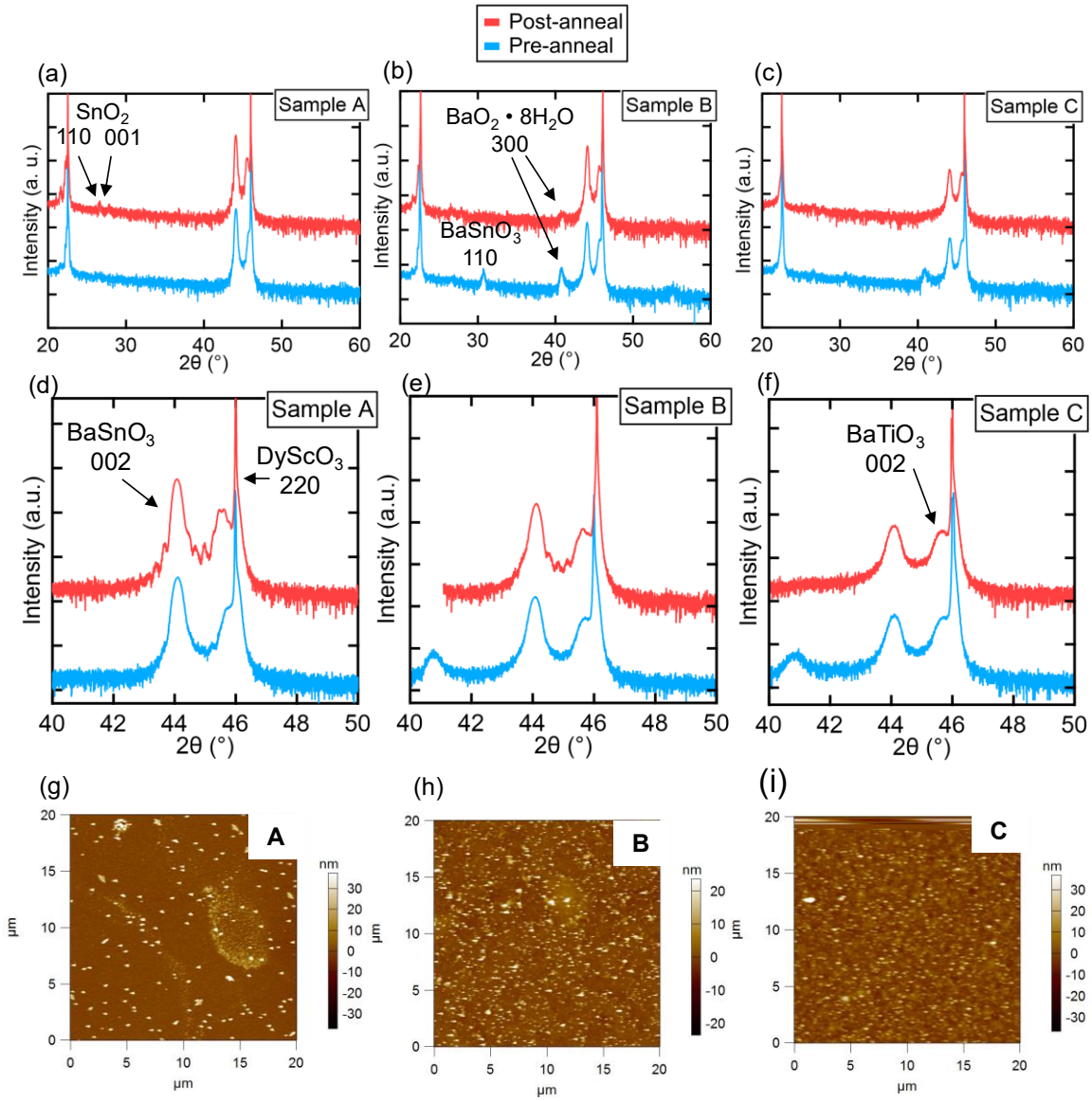

Figure 2.6 – (a-c) Wide-angle on-axis XRD scans for Samples A, B, and C, respectively. (d-f) High resolution XRD scan around the $BaSnO_3$ and $BaTiO_3$ 002 peaks and the $DyScO_3$ substrate peaks. (g-i) AFM scans of the surfaces of samples A, B, and C, respectively

heterostructures are covered in deposits (unclear if these are all SnO_2), no obvious signs of de-wetting of the $BaTiO_3$ layer are observed, other than some small, shallow pinholes in sample B (not shown). The $BaTiO_3$ layer is fully relaxed in all cases. The $BaSnO_3$ peak for samples A and B exhibited weak but present Laue thickness fringes after annealing, which allowed for a

rough measurement of the thickness. Thickness fringes were not apparent for sample C, and thus the thickness was assumed to be similar to the other samples.

Electrical properties of the heterostructures are given in Table 2.1. The $BaSnO_3$ layer of sample A had the same structure as the calibration sample shown in Fig. 2.5. The expected sheet carrier density for samples B and C were estimated assuming a consistent doping density with the calibration sample and scaled by the thickness of the doped layer. The mobilities for samples B and C were too low to accurately assess via Hall measurements. For sample A, there is a reduction of the measured n_{2D} by about 1×10^{14} cm^{-2}, and a reduction in mobility down to 86 cm^2 V^{-1} s^{-1}.

Table 2.1 – Data for the four $BaTiO_3/BaSnO_3$ heterostructure samples described in the text. The expected n_{2D} and μ values were based off of values measured in a calibration sample grown immediately prior to the heterostructures. Those marked with a * indicate the n_{2D} and μ was estimated by assuming the same constant 3D doping density and mobility as the calibration sample. Samples B and C were found to be too resistive to accurately measure carrier density and mobility

Sample	**A**	**B**	**C**	**D**
Thickness (nm)	34	32	~33	40
Doped portion of total thickness	2/3	1/2	1/3	2/1
Expected n_{2D} (cm^{-2})	3.7×10^{14}	2.2×10^{14} *	1.5×10^{14} *	1.1×10^{14}
Expected μ (cm^{-2} V^{-1} s^{-1})	112	112 *	112 *	140
Measured n_{2D} (cm^{-2})	2.7×10^{14}	-	-	$\sim2.5\times10^{13}$
Measured μ (cm^{-2} V^{-1} s^{-1})	86	-	-	~10

Growth conditions for the $BaSnO_3$ layer were further improved, and a calibration sample for a later heterostructure attempt exhibited a mobility of 143 $cm^2\ V^{-1}\ s^{-1}$ at a sheet carrier density of $1.1 \times 10^{14}\ cm^{-2}$. This sample had a more desirable sheet carrier density for pinch-off devices, and the raw mobility was higher. It was found later that this sample exhibited a small number of surface pits in AFM, possibly due to some surface deposits on the substrate. Another attempt at *in situ* $BaTiO_3/BaSnO_3$ heterostructure growth (sample D) was attempted immediately following the growth of the latest $BaSnO_3$ calibration sample. The XRD and AFM for this sample are shown in Fig. 2.7. We again see the $BaO_2 \bullet 8H_2O$ phase and misoriented $BaSnO_3$ 110 peak, as well as SnO_2 and an unidentified peak. Interestingly, the SnO_2 peak appears to diminish in intensity after the oxygen anneal, whereas in most cases this peak will increase in intensity after the anneal. The $BaSnO_3$ 110 peak is fully suppressed by the anneal, but the $BaO_2 \bullet 8H_2O$ hydroxide phase somewhat remains. AFM shows surface pits in this sample as well, again likely due to the substrate as the same batch of substrates was used for the heterostructure sample as the $BaSnO_3$ calibration sample. Height traces show these pits can extend up to 60 nm deep, which is roughly the thickness of the $BaTiO_3/BaSnO_3$ heterostructure, indicating they extend all the way down to the substrate. The electrical data for this heterostructure and its calibration sample are also shown in Table 2.1. A precipitous reduction in mobility is seen down to 10 $cm^2\ V^{-1}\ s^{-1}$, which is near the regime where the Hall measurement can be deemed to be inaccurate. If the sheet carrier density is to be trusted, it appears that this sample also suffered from a reduction of about $\sim 1 \times 10^{14}\ cm^{-2}$, similar to Sample A.

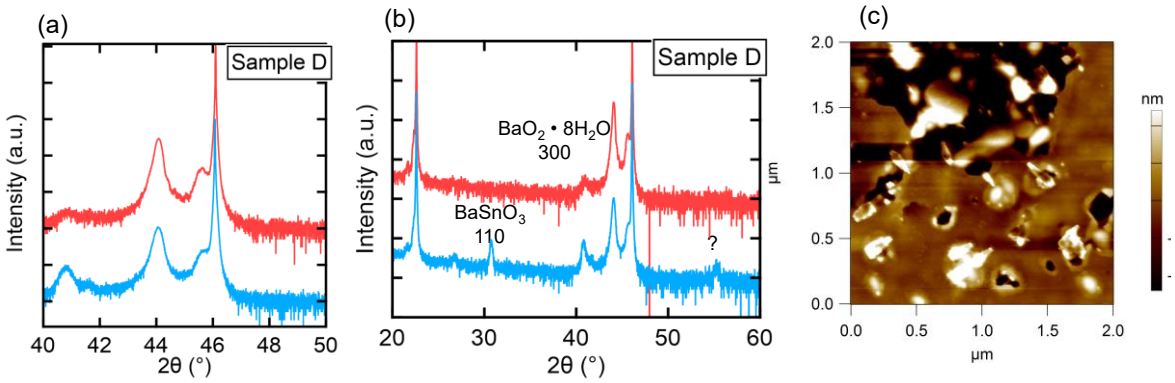

Figure 2.7 – (a) High resolution XRD scan around the $BaSnO_3$ and $BaTiO_3$ 002 peaks and the $DyScO_3$ substrate peaks of sample D. (b) Wide-angle on-axis XRD scan. (c) AFM scan of the surface of sample D, showing a strange surface morphology including pits

2.2.2 Discussion

It is unclear why the excess phases appeared for samples B-D but not for A. It is most probable that the excess phases exist at the $BaTiO_3/BaSnO_3$ interface, and likely formed due to a reaction between the layers. One possibility could be related to the SnO_2 surface deposits. Though crystalline SnO_2 is commonly observed in post-growth XRD, it is not known whether crystalline SnO_2 exists on the film surface while still under vacuum after growth. Neither spotty nor ring-like RHEED patterns are observed after the growth of the $BaSnO_3$ films, which would indicate that there is not a significant amount of rough crystalline deposits present at that time. Instead, it is possible that small droplets of liquid Sn remain present on the surface, which may oxidize upon seeing atmospheric oxygen. The idle temperature of the substrate in the growth chamber (i.e. when RHEED can be observed) is 300 °C, which is above the melting temperature of Sn (~232 °C), and thus these liquid droplets would never solidify such that they could be seen in RHEED. If these droplets are still on the surface when the $BaTiO_3$ is deposited,

it is very possible that they could lead to a reaction which could produce these extra phases. However, the fact that these extra phases did not appear for all heterostructures (including some not shown) clouds this picture. It should be noted that none of these excess phases seemed to appear for $BaTiO_3/BaSnO_3$ heterostructures in which the $BaSnO_3$ layer was first removed from the growth chamber, though some of those did exhibit $BaTiO_3$ wetting issues [95].

Though the excess phases are clearly undesirable for high-performance devices, it is unlikely that their presence is the sole cause of the poor electrical properties of samples B-D. They likely existed at the interface between the layers, and as mentioned in previous sections, $BaSnO_3$ mobility can be somewhat robust against the presence of macroscopic defects, including pits which extend down through the entire film layer. Instead, it is more likely that the primary cause for the degradation of mobility is due to carrier depletion caused by the epitaxial $BaTiO_3$ layer. As clearly evidenced in Sample A and possibly in Sample D, the addition of the $BaTiO_3$ layer reduces the sheet carrier density by an order of $\sim 1\times10^{14}$ cm^{-2}. This carrier depletion is likely caused by the ferroelectricity of the $BaTiO_3$ film [99], as opposed to a conduction band offset issue [100]. With fewer carriers to screen the now relatively higher concentration of ionized dopant atoms, the mobility of the remaining carriers suffers, leading to lower mobility in the channel. It is likely that this occurred in all films, and those films with less sheet carrier density to begin with experienced stronger relative depletion, and thus the mobility suffered more strongly than in sample A. As a final note, it was reported to us by our OSU collaborators that the $BaTiO_3$ gates of these heterostructures were extremely leaky, likely due to the dislocations propagating through the $BaTiO_3$ from the $BaSnO_3$, and others which may have newly formed due to the $BaTiO_3$ relaxation. This leaky gate behavior was observed in previous $BaTiO_3/BaSnO_3$ heterostructures [95].

2.2.3 Conclusions

Though plagued by unexplained secondary phases, it is likely that the $BaTiO_3$ layer itself resulted in the poor performance of the $BaTiO_3$/$BaSnO_3$ heterostructures described here. This highlights an issue with $BaSnO_3$ in general, in that it needs a sufficiently high carrier concentration to achieve the high mobility it is notable for. However, for high performance FET devices, the carrier density in the channel cannot be excessively high to allow for sufficient pinch-off. Thus, the overlap of the high-mobility region and the depletable FET region is small, if not nonexistent. The loss of mobility at low carrier densities is due to the high concentration of defects in $BaSnO_3$ films, not only ionized dopant atoms, but threading dislocations and perhaps other non-stoichiometric defects as well. As such, with the current state of relaxed $BaSnO_3$ films, it seems very difficult to achieve the high-performing $BaSnO_3$-based FET structures which relied on the presence of high carrier density in the channel.

2.3 Lattice-Matched Growths

Though MBE growth using an SnO_2 source enabled growth of the highest mobility films, the lack of a lattice-matched substrate means that films are plagued by defect-reducing dislocations. From the study of growths performed by PLD on $BaSnO_3$ substrates by Lee *et al*, it is evident that the use of the lattice-matched substrate can improve mobility above that of other PLD-grown films on lattice-mismatched substrates [91] (yellow circles in Fig. 2.2**)**. The use of excessively thick buffer layers (150 – 300 nm) to reduce the dislocation density in the active layer also does result in some of the highest reported mobilities in MBE-grown

films [58,84], though the improvement in mobility is marginal over that which can be achieved with much thinner buffer layers.

In order to disentangle the effect of dislocations from other possible defects, lattice-matched growths are a valuable tool, even when the availability of the lattice-matched substrates is extremely small and thus not immediately scalable. Here, we describe some very limited growths on two types of lattice-matched substrates: $SrZrO_3$ and $BaSnO_3$.

2.3.1 $SrZrO_3$ substrates

$SrZrO_3$ has a pseudocubic lattice parameter of 4.103 Å and thus a lattice mismatch of only ~ -0.3% with $BaSnO_3$ (Fig. 2.1). However, due to the high melting temperature of $SrZrO_3$, high-quality substrate crystals are difficult to produce, and thus are not widely available. A batch of $SrZrO_3$ substrates had been purchased by previous students from MaTeck GmbH. Due to the difficulty in growing large, high-quality crystals of this material, the largest substrate size that could be obtained were only 3 mm × 3 mm, smaller than the typical 5 mm × 5 mm used for our $BaSnO_3$ growths. This is undesirable as the smaller substrate size necessitates a different type of substrate holder used for growth, which relies on spring-clamps on the side of the substrate rather than small pins that clamp on the sample surface (Fig. 2.8). The surface pin design is not used here as they need to be large enough to reliably hold the sample in the block, but this would cover a relatively larger area of the smaller substrate surface than they do for larger substrates. This type of substrate holder has a much higher propensity for nonuniform heat coupling into the substrate.

The desired crystallographic surface plane for the $SrZrO_3$ substrates was the (100) *pseudocubic* plane, or $(100)_{pc}$, which essentially corresponds to the (110) plane using the

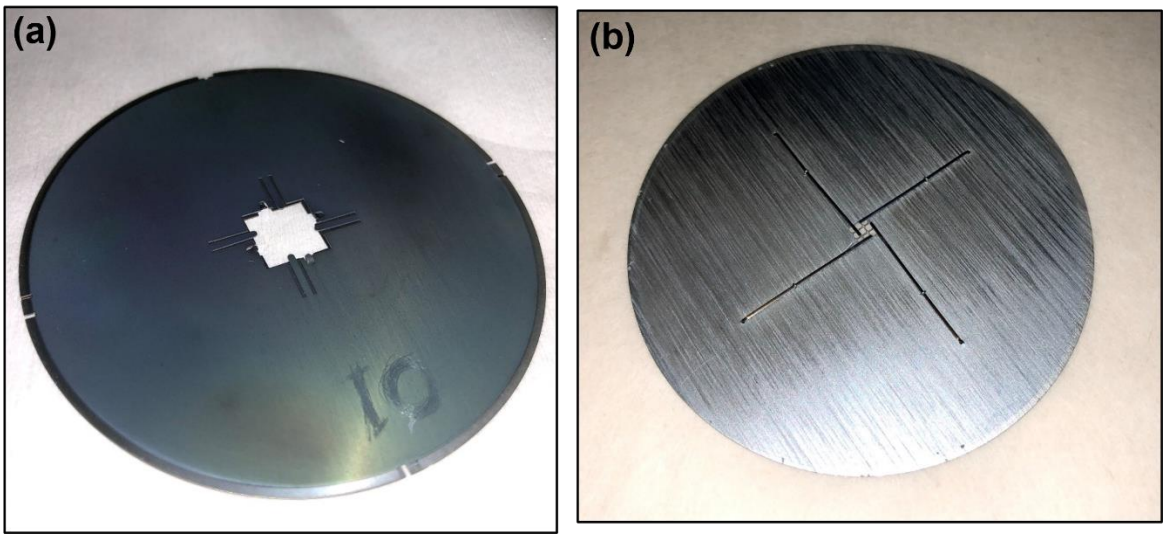

Figure 2.8 – (a) Traditional Mo faceplate used to hold 10 mm x 10 mm substrates, which rely on small pins which contact the surface and hold the substrate in the assembly. (b) Spring-clamp faceplate design used for 3 mm x 3 mm substrates. A grid of wires is used to prevent the substrate from falling through the hole which allows for radiative heating of the substrate.

formal orthorhombic unit cell of $SrZrO_3$, or $(110)_{or}$. Through a miscommunication with the supplier, the crystals that were delivered were oriented in the $(100)_{or}$ plane, corresponding to a $(110)_{pc}$ plane. The preferred growth direction of $BaSnO_3$ is [001] and thus growth on (100)-oriented substrates leads to smooth planar growth. Consequently, $(110)_{pc}$-oriented substrates induce [110] growth and lead to 3D surface faceting of the $BaSnO_3$. Further issues with the substrates can be seen in Fig. 2.9, where the rocking curve XRD measurement of the substrate shows multiple humps indicating poor crystalline quality (again due to the difficult crystal growth). The $SrZrO_3$ substrates were backed with 250 nm of Mo in the same way as other substrates.

Growth calibrations were carried out using 3 mm × 3 mm $DyScO_3$ (110) substrates. The highest mobility measured in the $DyScO_3$ calibration samples was ~100 $cm^2\ V^{-1}\ s^{-1}$, owing to the suboptimal heat uniformity of the smaller substrate holder. The single growth on a $SrZrO_3$

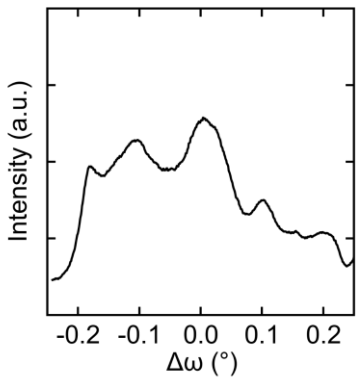

Figure 2.9 – XRD rocking curve scan of the 220 reflection of a $SrZrO_3$ substrate. Multiple asymmetric peaks are seen, indicating poor crystalline quality.

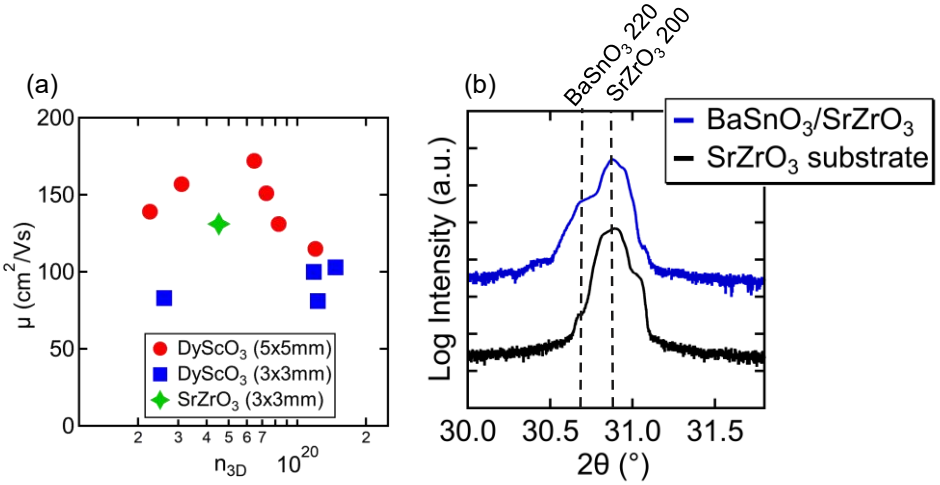

Figure 2.10 – (a) Comparison of mobilities achieved for calibration samples compared to the mobility of the growth on the 3mm x 3mm $SrZrO_3$ substrate. The growths on 3mm x 3mm $DyScO_3$ are severely reduced from what can generally be achieved on 5mm x 5mm $DyScO_3$ substrates. (b) On-axis XRD scan around the 200 (orthorhombic) reflection of $SrZrO_3$ and the $BaSnO_3$ 220 reflection, showing the appearance a shoulder corresponding to the $BaSnO_3$ peak position after film growth.

substrate produced a mobility of 131 $cm^2 V^{-1} s^{-1}$, significantly higher than any of the 3 mm × 3 mm calibrations (Fig. 2.10(a)). As expected, the growth proceeded in a 3D fashion due to the [110] growth direction of the $BaSnO_3$ film. A shoulder corresponding to the $BaSnO_3$ 220 peak

is seen to appear in post-growth XRD (Fig. 2.10(b)). Cross-section STEM shown in Fig. 2.11 shows an abrupt interface and no observable dislocations or extended defects. This confirms that the closely lattice-matched $SrZrO_3$ substrate enabled the growth of a coherently strained $BaSnO_3$ film. The film thickness is roughly the same thickness as that of the calibration samples (~50 nm), but the measured doping density is lower.

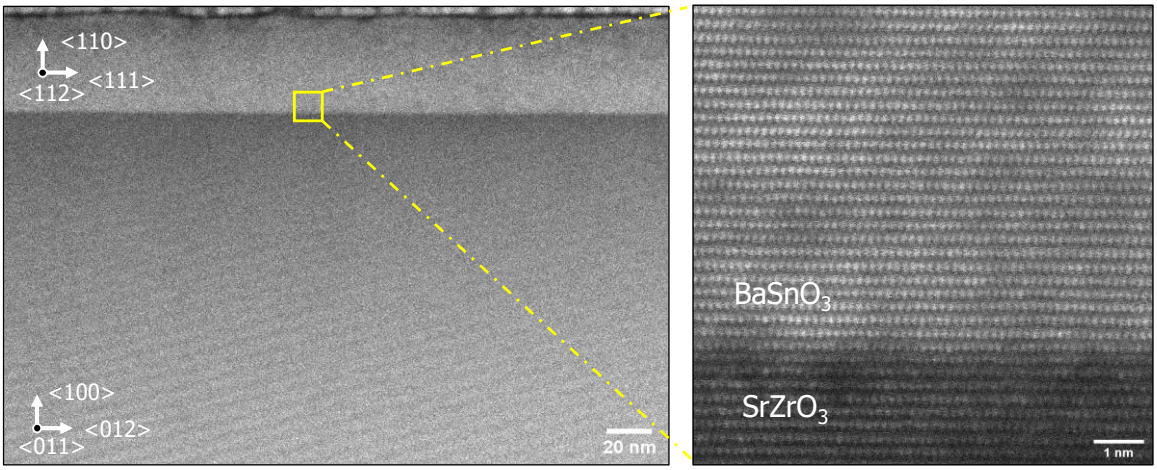

Figure 2.11 – Cross-section STEM images of the $BaSnO_3/SrZrO_3$ interface. A sharp interface is observed with no clearly identifiable extended defects, indicating a fully strained film. STEM images courtesy of Salva Salmani-Rezaie.

2.3.2 $BaSnO_3$ Homoepitaxy

The successful growth of relatively large single crystals of $BaSnO_3$ using a hydrothermal method by collaborators at Clemson University [101] afforded the opportunity to attempt a small number of homoepitaxial growths using the crystals as substrates. These results will not be discussed in detail, as they essentially amount to a single data point, but the experience further highlights some known difficulties in achieving high mobilities in MBE-grown $BaSnO_3$ films.

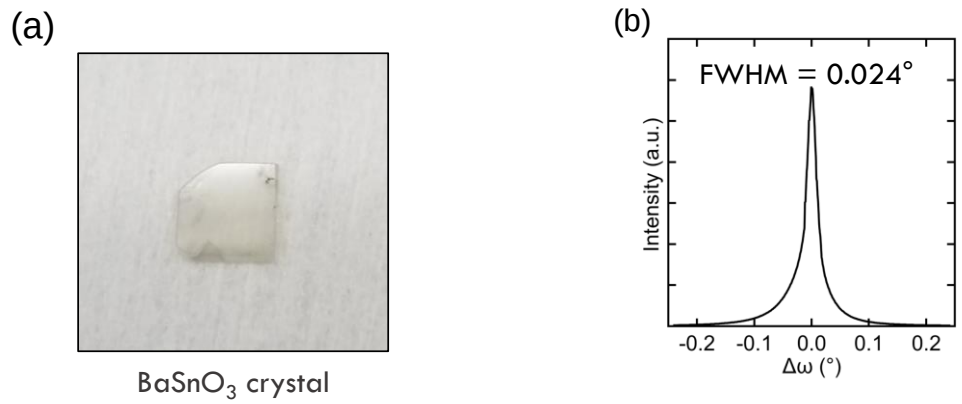

Figure 2.12 – (a) Photograph of the $BaSnO_3$ single crystal used as a substrate for homoepitaxial $BaSnO_3$ growth. (b) XRD rocking curve scan of the 002 reflection of the $BaSnO_3$ single crystal substrate, which exhibits a low FWHM of 0.024° indicating good crystallinity

The crystals used were (100) oriented slabs with approximate dimensions of 5 mm × 5 mm × 0.5 mm. As can be seen in Fig. 2.12(a), these did not have perfect dimensions due to the difficulty in achieving crystals with significantly larger dimensions than 5 mm × 5 mm. A small batch of crystals were cut and polished by a commercial polisher and delivered to us at UCSB. These crystals exhibited excellent crystallinity as seen by the rocking curve scan in Fig. 2.12(b). 250 nm of Mo was deposited on the back of the crystal, as is done for other substrates. AFM revealed that the crystals possessed a rather significant amount of surface deposits even after washing with acetone and isopropanol. Growths were attempted despite this, as a more aggressive cleaning treatment was not advised due to the brittleness of the crystals.

RHEED of the $BaSnO_3$ substrate exhibited streaks, indicating a smooth crystalline surface, though the streaks were somewhat weak and diffuse as a result of the surface deposits [Fig. 2.13]. The RHEED of the La-doped film was sharper and more intense, indicating that the films grew in a 2D fashion and with a smooth surface, despite the substrate surface deposits.

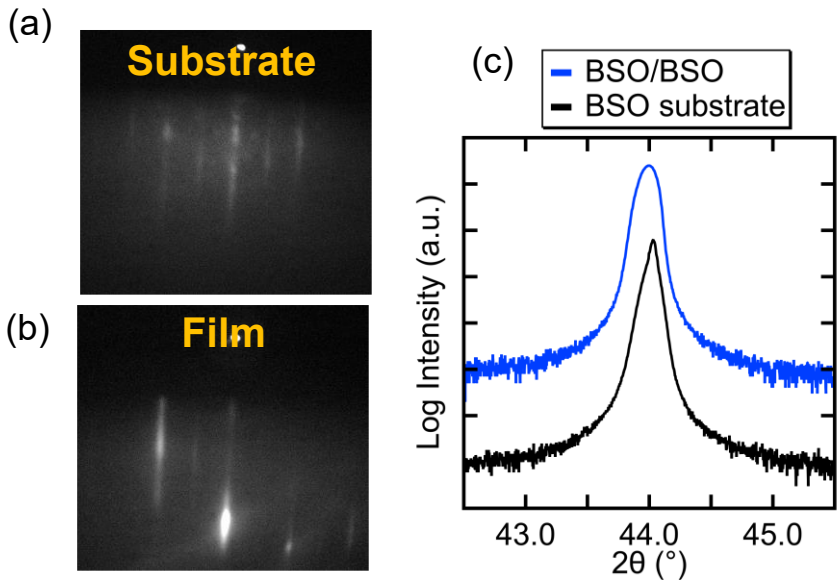

Figure 2.13 – RHEED pattern of (a) the $BaSnO_3$ substrate surface and (b) the epitaxial La-$BaSnO_3$ film. The relatively weak streaks and diffuse background of the substrate are likely due to surface deposits. (c) On-axis XRD scans of the bare $BaSnO_3$ (BSO) substrate and the La-$BaSnO_3$/$BaSnO_3$ heterostructure. The epitaxial film induces a slight broadening of the 002 peak.

XRD of the homoepitaxial film exhibited no additional phases, only a slight broadening of the $BaSnO_3$ peaks relative to that of the bare substrate [Fig. 2.13(c)]. Cross-section STEM was performed to further characterize the homoepitaxial film, as shown in Fig. 2.14. While some extended defects can be seen in the substrate, there is no evidence of relaxation-induced dislocations in the film. The film thickness was measured to be approximately 41 nm, and though the film is homoepitaxial, a contrast at the interface can be clearly observed. In Fig. 2.14(b), a surface pit is seen to extend through almost the entire film thickness. Post-growth AFM also shows pits that are approximately as deep as the film thickness. These pits are likely due to the presence of the surface deposits preventing growth in the regions they covered.

A calibration growth using a $DyScO_3$ (110) substrate was performed immediately prior to the homoepitaxial growth attempt, which exhibited a room temperature mobility of 150 cm^2

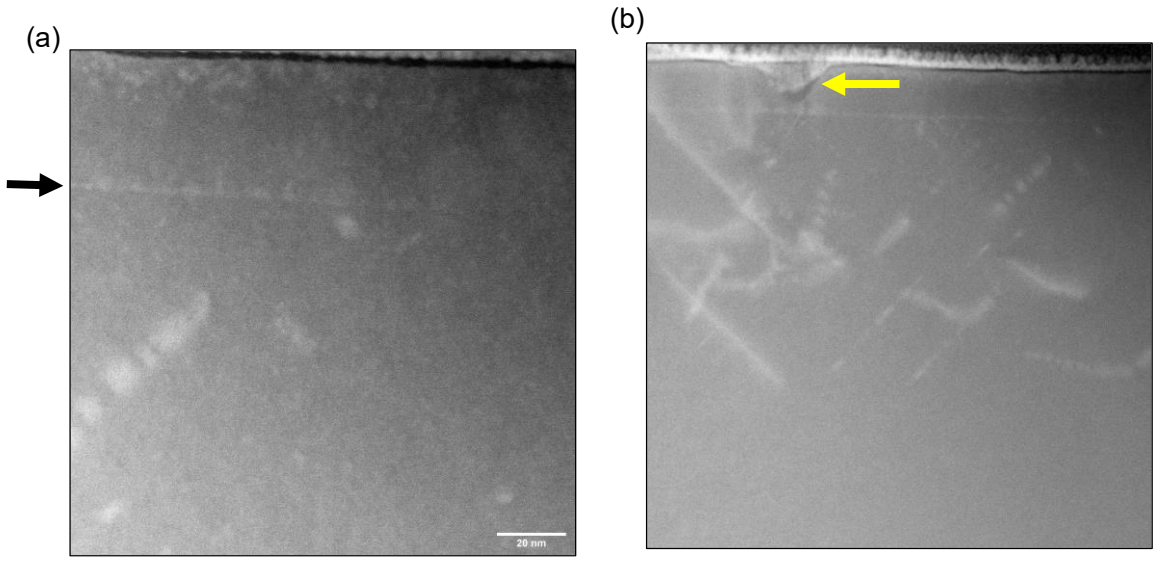

Figure 2.14 – Cross-section STEM images of the $BaSnO_3$ (film) / $BaSnO_3$ (substrate) homoepitaxial sample. In (a) the interface can be seen as a faint horizontal line indicated by the black arrow. Though extended defects can be seen to originate from the substrate, no relaxation-induced dislocations are observed in the film, as is expected for homoepitaxial growth. (b) A surface can be seen (yellow arrow), which nearly extends down to the substrate. STEM images courtesy of Salva Salmani-Rezaie.

V^{-1} s^{-1}. The measured mobility of the homoepitaxial film, however, was only 53 cm^2 V^{-1} s^{-1}. The thickness of the calibration sample was 70 nm, compared to 41 nm of the homoepitaxial film, indicating vastly different growth conditions. The pits are not believed to be the cause of the low mobility, as other samples with surface pits have exhibited high mobility (Appendix A). Instead, the different growth environment experienced by the irregularly-shaped $BaSnO_3$ substrate from that of more uniformly shaped commercial substrates likely resulted in a drastic shift of growth conditions. Specifically, the irregular shape could have led to sub-optimal heat transfer into the film, resulting in a different (and more nonuniform) effective substrate temperature. If the thermal properties of $BaSnO_3$ are markedly different from the other perovskite oxide substrates, this too could lead to a different effective growth temperature and thus different growth conditions from the calibration samples, though it is assumed these

differences are negligible. In any case, further evidence for the shifted growth conditions with the $BaSnO_3$ substrate can be seen by the drastic change in growth rate.

2.3.3 Conclusions: Lattice-matched growths

The elimination of dislocations is likely the cause of the mobility improvement of the growth on the $SrZrO_3$ substrate compared to calibration samples grown on $DyScO_3$. It was believed that growth conditions were as well-calibrated as could be achieved for 3 mm × 3 mm growths which necessitate the suboptimal setup, and thus this single growth represents the most that could be hoped to be learned from such a study, unless a vastly improved substrate holder design could be made or larger substrates of $SrZrO_3$ were made available.

While only a single growth was performed using the first batch of $BaSnO_3$ crystal substrates and thus results by no means represent an extensive study, some very basic observations can be made: (i) as expected, homoepitaxial growth resulted in no misfit dislocations, (ii) the elimination of misfit dislocations did not have a strong influence on mobility improvement which could overcome the drastic limitations caused by sub-optimal growth conditions. Similar to the $SrZrO_3$ growths, this again highlights the fact that, while misfit dislocations undoubtedly reduce mobility in the absence of other mobility-limiting factors, they are likely not the ultimate limiter of mobility in MBE-grown films.

It is noted that a second homoepitaxial growth carried out by Wangzhou Wu on a later batch of $BaSnO_3$ crystal substrates exhibited higher mobility of 115 $cm^2\ V^{-1}\ s^{-1}$. This was performed on a more regularly-shaped crystal with a cleaner surface. Additionally, this crystal substrate was oriented in the less-favorable (110) orientation, similar to the $SrZrO_3$ substrate orientation.

2.4 Stoichiometry control in MBE-grown $BaSnO_3$ films

The reduction of threading dislocations does not scale with improvement in mobility as strongly as would be expected if dislocations were the primary limiter of mobility [80]. The use of undoped buffer layers marginally improves mobility, but even for excessively thick buffer layers (> 150 nm), mobility is limited to below 200 $cm^2\ V^{-1}\ s^{-1}$ [58]. As can be seen in Fig. 2.15, growths on $DyScO_3$ substrates have been able to produce the highest mobility even though $PrScO_3$ is more closely lattice-matched. This in part could be due to the sheer larger number of growths performed and thus calibrated using $DyScO_3$ substrates, but this also highlights the fact that simply reducing the density of threading dislocations from film relaxation doesn't necessarily result in a drastic mobility improvement and that growth

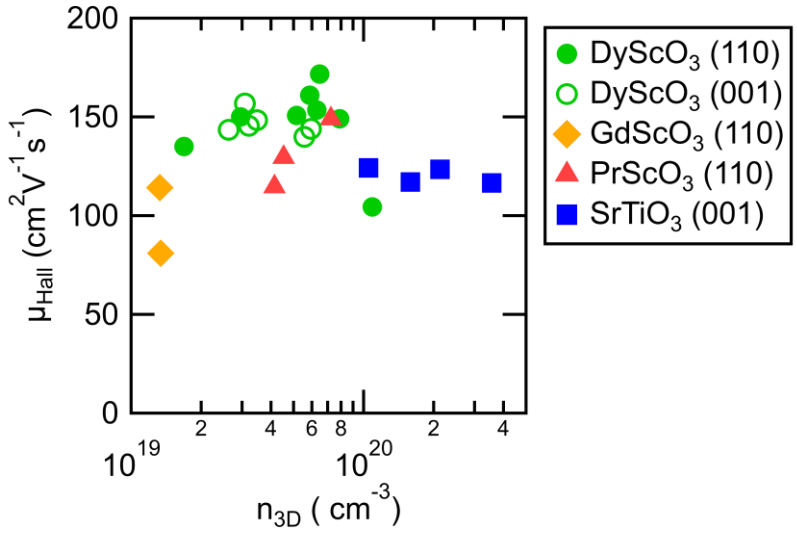

Figure 2.15 – Comparison of maximal La-$BaSnO_3$ film mobilities grown on various commercially available substrates at UCSB by MBE using a SnO_2 source. Though $PrScO_3$ has the lowest lattice mismatch with $BaSnO_3$ (-2.2%), the highest mobilities have been measured on films grown using $DyScO_3$ (110) substrates (-4%).

conditions (and presumably stoichiometry) play a similar role, as was also observed in limited lattice-matched growths.

It has been claimed that growing $BaSnO_3$ using SnO_2 as a source affords an adsorption-controlled growth window [84]. However, it should be noted that this is not synonymous with perfect composition control, only the controlled growth of a single phase. The use of SnO_2 aids in the incorporation and oxidation of Sn to form $BaSnO_3$, as using metallic Sn with an oxidant results in the formation of Sn droplets on the growth surface and poor growth quality [80]. The fact that SnO, the primary species evaporating from SnO_2 [83], is volatile affords the opening of the adsorption-controlled growth window. However, the prevalence of SnO in the vapor of SnO_2 also highlights the fact of the dual valence of Sn: Sn^{4+} (as it exists in SnO_2) is favored in oxidizing conditions, and Sn^{2+} (as it exists in SnO) is favored in reducing conditions. In the high vacuum (i.e. reducing) environment of MBE, the pre-oxidized Sn is provided primarily as Sn^{2+}. In a II-IV perovskite such as $BaSnO_3$, the formal charges of the ions are $A^{2+}B^{4+}(O^{2-})_3$, and thus Sn must take the Sn^{4+} valence to sit on the B-site. The adsorption-controlled growth afforded by the volatility of SnO differs from that exhibited for other perovskites which possess a volatile binary oxide of one of the constituents, such as $PbTiO_3$. The adsorption-controlled growth of $PbTiO_3$ is afforded by the volatility of PbO [102], which contains Pb^{2+}. Pb also exists in the Pb^{2+} charge state in $PbTiO_3$. Similarly, for the hybrid growth of $SrTiO_3$, TTIP supplies Ti in the Ti^{4+} charge state, as it exists in $Sr^{2+}Ti^{4+}(O^{2-})_3$. In contrast, SnO does not supply Sn in the appropriate valence state, and the Sn^{2+} must be further oxidized to Sn^{4+} by an additional oxidant. However, the dual valence of Sn also opens the possibility for it to incorporate on the A^{2+} site as the antisite defect Sn_{Ba}, which has been shown by DFT to be a stable defect in $BaSnO_3$ in oxygen-poor conditions [103]. Therefore, unless sufficiently

oxidizing conditions can be achieved, there is a high propensity for Sn_{Ba} to form when growing $BaSnO_3$ via high-vacuum methods.

In the following study, we grew $BaSnO_3$ films under various oxidant conditions to explore its effects on the stoichiometry of the films. Rather surprisingly, we found it possible to grow moderately high-mobility films without an additional oxidant at all, indicating that the SnO_2 source not only provides Sn but also a significant amount of O. Lattice constant measurements were consistently lower than the stoichiometric value in almost all films, which is likely a consequence of significant amounts of Sn_{Ba} antisite defects even in the highest mobility films achieved here. The additional oxidants shifted the growth conditions but were unable to eliminate Sn_{Ba} defects, likely indicating their presence even in the highest-mobility films grown by MBE.

2.4.1 Description of experiment

La-doped $BaSnO_3$ films were grown by MBE on (110) $DyScO_3$ substrates. Three sets of films were grown, differentiated by the use of an oxidant: a set grown without any co-supplied oxidant ("no oxygen" films), a set using just molecular oxygen, and a set using oxygen RF-plasma. Prior to growth, all samples were annealed at the growth temperature of 850 °C followed by a 10-minute oxygen plasma exposure. For the films grown with a co-supply of oxygen plasma, the growth proceeded directly following the 10-minute plasma anneal, keeping the same conditions for the plasma. The oxygen BEP was held at ~1.0×10^{-5} Torr during the growth of films using molecular oxygen, but the RF plasma source was turned off following the anneal. For the samples grown without any co-supplied oxidant, the chamber was allowed

to pump for 5 minutes following the plasma anneal to reduce background oxygen, followed by growth using only Ba, La, and SnO_2. For each condition, a series of films were grown at different SnO_2/Ba flux ratios by keeping the SnO_2 cell temperature constant and varying the Ba flux. Growth times were adjusted to compensate for the change in growth rate due to difference in Ba flux to achieve films with thicknesses ≥ 35 nm. The growth rate was found to be Ba-limited for all growths regardless of oxidant condition (Fig. 2.16).

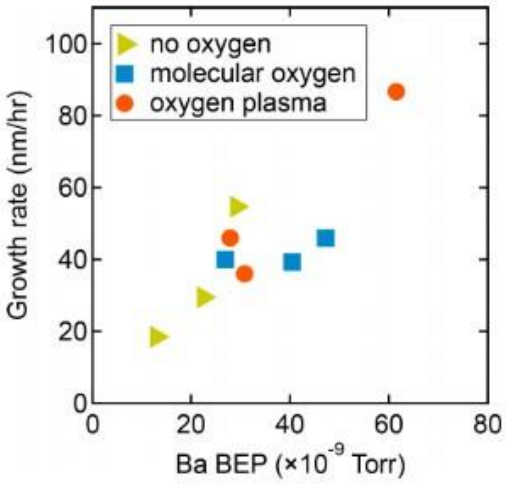

Figure 2.16 – Film growth rates as a function of Ba flux for the films presented in this study. Adapted with permission from ref. [89]

The La flux was adjusted to keep the doping density within the ~$1 \times 10^{19} - 3 \times 10^{20}$ cm^{-3} range, as mobility is relatively independent within this range. It is important to note that the mobile carrier density is affected by the growth parameters that were varied in these experiments, not just the La flux. These include cation flux ratios and the oxygen supply, which determine dopant activation and the concentration of compensating defects [103,104], and the growth rate. As mentioned above, state-of-the-art $BaSnO_3$ films all seem to exhibit some degree of nonuniformity and variability in electrical properties despite nominally identical growth conditions, as is also seen in the literature [84]. As such, differences in mobility values

of a few 10's of $cm^2\ V^{-1}\ s^{-1}$ are not taken as significant and instead systematic trends are the focus of this study. Robust indicators such as insulating behavior and large deviations from high mobility – which here we will define as 120 $cm^2\ V^{-1}\ s^{-1}$ – within this doping range as being indicative of the introduction of defects.

RHEED was used to monitor the growth. Structural characterization of the films was carried out via high-resolution XRD: a triple-axis configuration was used to assess out-of-plane lattice parameters a_{op}, and open detector scans were used to assess film crystallinity. Straight-beam alignments were performed prior to every measurement to eliminate any residual instrumental offset. When XRD thickness fringes were not present, x-ray reflectivity (XRR) was used to calculate film thickness. For films with poor XRR due to the surface morphology, the thickness was estimated from the Ba flux due to Ba-limited growth rate (Fig. 2.16). Electrical measurements were performed in a vdP geometry as described in section 2.1.2.

2.4.2 Results

Figure 2.17 shows XRD data of films grown with different SnO_2/Ba flux ratios and the various oxidant conditions (no oxygen, oxygen, and oxygen RF-plasma). All films exhibit the 002 $BaSnO_3$ reflection, indicating successful epitaxial growth of the $BaSnO_3$ perovskite phase for all growth conditions. The no-oxygen sample grown at SnO_2/Ba = 15 also exhibits a wide hump on the low-angle side of the 002 $BaSnO_3$ peak, which can be seen more clearly in wide-angle scans (Fig. 2.18). This peak may belong to a Ba-rich phase, possibly Ruddlesden-Popper Ba_2SnO_4 [105]. Films grown with oxygen do not exhibit the Ba-rich peaks in XRD. Some films also exhibit weak SnO_2 peaks in wide-angle scans.

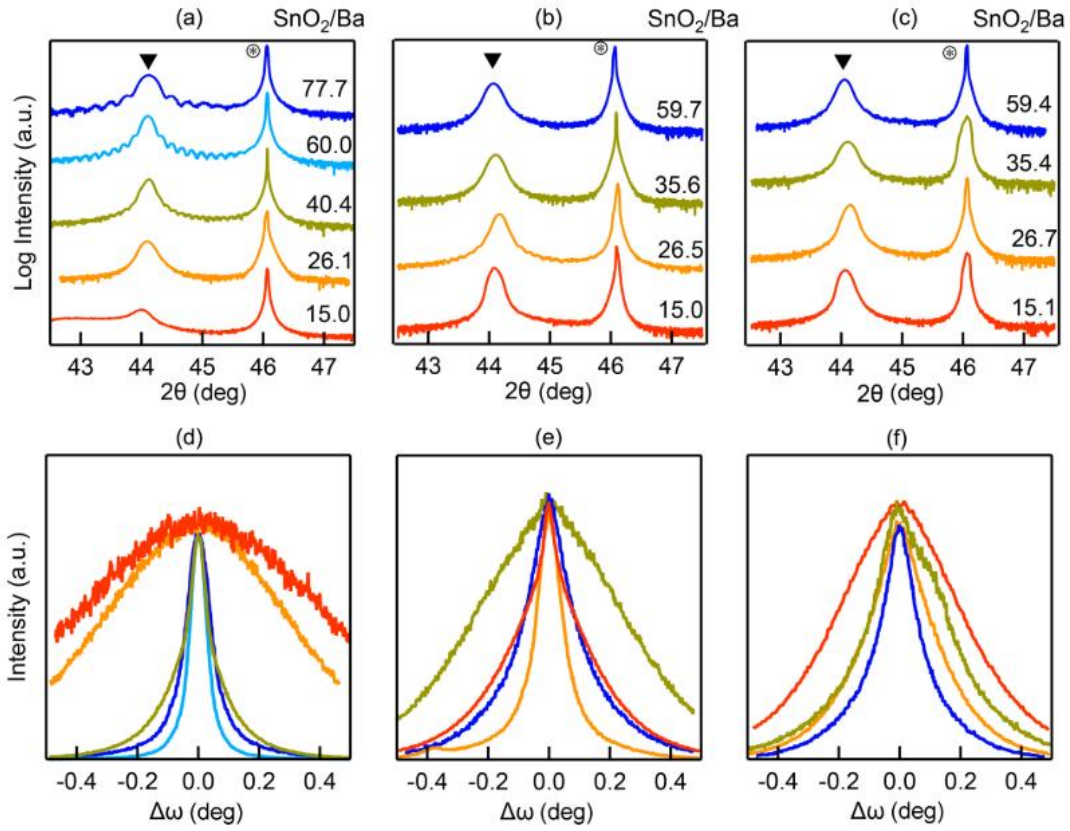

Figure 2.17 – [(a)-(c)] On axis XRD scans around the $BaSnO_3$ 002 reflection for films grown with (a) no additional oxygen (b) molecular oxygen, and (c) oxygen plasma. [(d)-(f)] Rocking curve measurements around the $BaSnO_3$ 002 reflection for films grown with (a) no oxygen, (b) molecular oxygen, and (c) oxygen plasma. The triangles mark the 002 $BaSnO_3$ reflections, and the asterisks mark the 220 $DyScO_3$ substrate reflections. Adapted with permission from ref. [89].

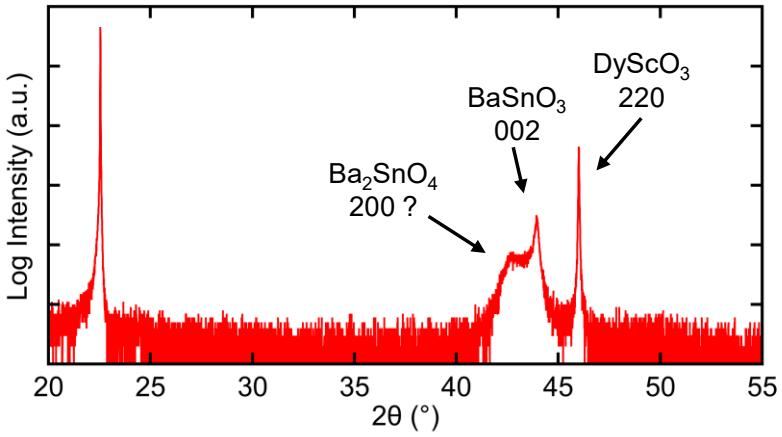

Figure 2.18 – Wide-angle on-axis XRD scan of the no oxygen film grown with flux ratio SnO_2/Ba = 15, showing a broad hump that may correspond to the Ruddlesden-Popper Ba_2SnO_4 002 reflection.

X-ray rocking curves are shown in Figs. 2.17(d)-(f). Their widths represent the crystal surface quality and crystalline perfection of the films' interiors. For example, for the films grown without additional oxygen [Fig. 2.17(d)], the narrow curves are also those that exhibit thickness oscillations in Fig. 2.17(a), indicating smooth surfaces. These films are grown with the highest SnO_2/Ba flux ratios and all have similar full width at half maxima (FWHM) values of 0.097°, 0.068°, and 0.099°. The differ, however, in the width of the lower portion of the rocking curve, which typically contains the diffuse scattering from point defects. The width of the rocking curve wing correlates with the measured mobility, indicating that the point defects giving rise to the intensity in this portion of the rocking curve are also ones that affect the mobility.

Samples grown with additional oxidant show a less systematic relationship between carrier mobility and rocking curve widths. Oxygen tends to reduce the mobility of arriving adatom species on the growing film surface [106]. This negatively affects crystalline perfection and surface quality and both cause broadening of the rocking curves. In addition, for some samples, the 220 peak from $DyScO_3$ substrate displays a shoulder that is reflected in an asymmetry in the film rocking curve, such as for the 35.4 ratio film [Figs. 2.17(c) and (f)].

Figure 2.19 compares the measured a_{op} and Hall mobilities μ. Samples that were too resistive to reliably measure the Hall mobility are displayed as having $\mu = 0$ cm^{-2} V^{-1} s^{-1}. Three important observations can be made: (i) most measured a_{op} are smaller than the reported stoichiometric values for $BaSnO_3$ (indicated by the dotted line), (ii) the mobilities are highest near the minimum in a_{op} , rather than near the apparent stoichiometric value, and (iii) addition of oxygen shifts the growth conditions to achieve films that exhibit the highest mobility to lower SnO_2/Ba ratios, compared to films grown with no additional oxygen. In addition, slightly

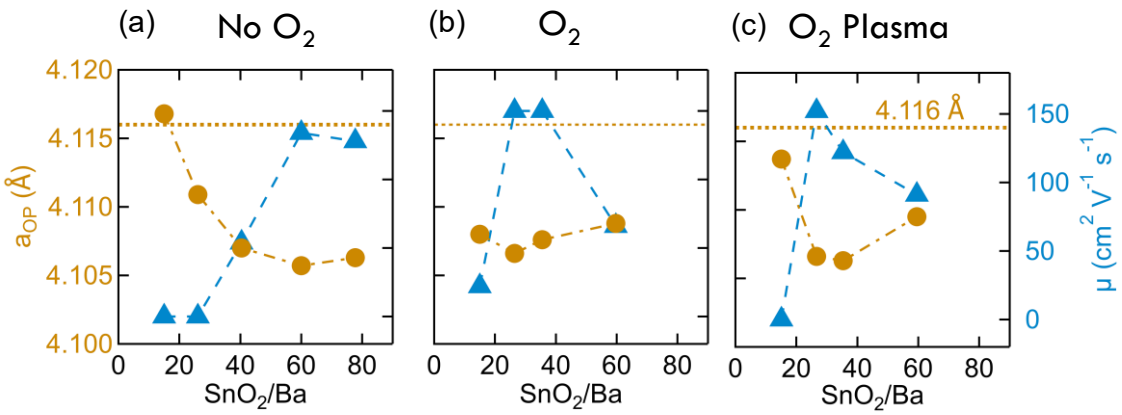

Figure 2.19 – Out-of-plane lattice constant a_{op} (yellow circles, left axis) and the measured Hall mobilities (blue triangles, right axis) as a function of SnO_2/Ba BEP ratio for films grown with (a) no additional oxidant, (b) molecular oxygen, and (c) oxygen plasma. Adapted with permission from ref. [89].

higher mobilities are achieved in the films grown with extra oxygen. As mentioned previously, we note that the small a_{op} is not caused by residual epitaxial coherency strains, as compressively strained films would lead to an expanded a_{op}. The films are confirmed to be fully relaxed, and indeed also show contracted in-plane lattice parameters as seen in a representative RSM in Fig. 2.20.

2.4.3 Discussion

A main result is the successful growth of $BaSnO_3$ without any co-supplied oxidant. This shows that oxygen-containing species needed to form the $BaSnO_3$ perovskite phase are mainly supplied by the flux from the SnO_2 cell, i.e. SnO and a small amount of O_2 The small amount of O_2 in the flux from the SnO_2 cell suggests that films grown without an additional oxidant are grown in oxygen-poor conditions. If SnO is the main source of oxygen, then growth

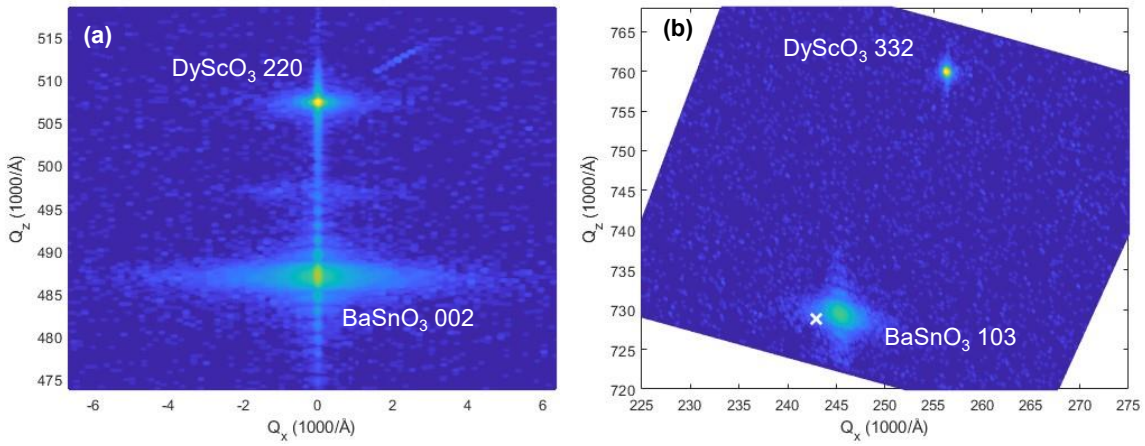

Figure 2.20 – Reciprocal space maps (RSMs) for a no oxygen sample grown with a SnO_2/Ba BEP ratio of 60.0 around (a) on-axis $BaSnO_3$ 002 and $DyScO_3$ 220 peaks, and (b) off-axis $BaSnO_3$ 103 and $DyScO_3$ 332 peaks. The crosses in (b) indicate the expected position of the reflection for a fully relaxed, stoichiometric $BaSnO_3$ film. Adapted with permission from ref. [89].

conditions are likely also Sn-rich. Sn-rich conditions are supported by the Ba-limited growth rates (Fig. 2.16**)**. In the absence of a true MBE adsorption-controlled growth window or for compounds that are not true line compounds, nonstoichiometric growth conditions will induce native point defects, such as vacancies or antisite defects [64,102,107].

Next, we discuss possible defects, beginning with the films grown with no additional oxygen. The deviation of the lattice parameter from its stoichiometric value provides information about the prominent defect(s). Cation vacancies cause a lattice expansion in most perovskites and may in $BaSnO_3$ as well [65,81]. Oxygen vacancies cause virtually no variation in the lattice parameter of $SrTiO_3$ thin films [108], although there are indications that they may cause a moderate lattice expansion in $BaSnO_3$ [93]. In contrast, Sn^{2+} incorporation on the Ba site may lead to a lattice contraction [109], because the Ba site is large compared to the ionic radius of Sn^{2+}. In general, perovskites that incorporate Sn on the *A* site are found to exhibit reduced lattice parameters [110–112]. Therefore, we posit that the small a_{op} are a fingerprint

of Sn_{Ba} formation in these films. Given oxygen-poor, Sn-rich conditions, Sn_{Ba} is a likely mechanism to accommodate Sn excess in the high-mobility films. This is also consistent with DFT calculations for these conditions [103,104,113].

On the low SnO_2/Ba flux ratio side, some films appear to possess a_{op} values that are closer to the stoichiometric values, though their poor electrical properties indicate that these films are not stoichiometric. A more likely scenario for the apparent stoichiometric a_{op} is that another defect, which causes a lattice expansion, compensates for the lattice contraction caused by Sn_{Ba}. According to DFT [103,104], under Sn-rich conditions, Ba vacancies (V''_{Ba}) and Sn_{Ba} are favorable. Donor dopants may under certain conditions also favor cation vacancies [114]. In contrast to Sn_{Ba}, V''_{Ba} are likely to cause a lattice expansion and furthermore to act as acceptors [113]. From the change in lattice parameter seen in Fig. 2.19(a), it is apparent that V''_{Ba} are more favorable under conditions that are less Sn-rich and possibly also more oxygen poor (larger lattice parameter). As the SnO_2/Ba flux ratio is increased their concentration decreases, most likely by incorporation of Sn^{2+} on the empty Ba sites, which causes the lattice parameter to decrease. The increase in mobility with increasing SnO_2/Ba flux can then be explained with Sn_{Ba} filling the negatively charged V''_{Ba}, which should scatter more strongly by ionized impurity scattering and/or trap mobile carriers than the charge-neutral Sn_{Ba}. Ultimately, however, even charge-neutral defects contribute to carrier scattering and reduce their mobilities. We note that another defect candidate causing a lattice expansion could be oxygen vacancies, $V^{\circ\circ}_{O}$. The high degree of La-doping should, however, suppress the formation of $V^{\circ\circ}_{O}$, while promoting compensating V''_{Ba} [104].

This general picture is further confirmed by considering the trends in the films grown with additional oxygen. Lower- than-stoichiometric a_{op} are exhibited by these films as well, pointing

to the presence of Sn_{Ba} defects. Therefore, it appears that even in the presence of additional oxygen during growth, even in the form of an activated plasma, the conditions are still Sn-rich. The main effect of additional oxygen supplied by the molecular or plasma source is to shift the growth conditions. The extra oxygen shifts the growth conditions for high mobility films toward lower SnO_2/Ba ratios. This is consistent with the interpretation discussed above: the extra oxygen alleviates the need to supply a large amount of oxygen via SnO, making the conditions less Sn-rich. Thus, the only way to improve the cation stoichiometry of $BaSnO_3$ films would be achieve vastly more oxidizing conditions, which appears to be difficult to achieve within the constraints of MBE. Already, one difficulty for the films grown with additional oxygen supply is the oxidation of the Ba source material and associated Ba flux instabilities [115].

Finally, it should be noted that the observed variations in carrier density (n_{3D}) of about ~1-4 × 10^{19} cm^{-3} for films grown at different cation flux ratios would indicate that the concentration of electrically active defects from non-stoichiometry is estimated to be less than 1%. This degree of non-stoichiometry is difficult to detect with most thin film physical characterization techniques, while nevertheless being significant enough to strongly affect the electrical properties.

2.4.4 Conclusions

It has been demonstrated that La-doped $BaSnO_3$ films can be grown by MBE using only Ba, La, and SnO_2 effusion sources which exhibit mobilities on par with growths utilizing additional oxidants. Even when oxygen is supplied, however, lattice parameter measurements

indicate that films are nonstoichiometric. It has been argued that the films are Sn-rich and that the origin of this are twofold: SnO is a major source of the oxygen incorporated in the films and the dual valency of Sn facilitates the formation of Sn_{Ba} antisite defects, which can accommodate excess Sn. Moreover, the study showed that films with an apparent stoichiometric lattice parameter are, in fact, also nonstoichiometric, most likely because the effects of two defects on the lattice parameter compensate each other in this regime. Thus, unlike materials that are much closer to line compounds and can be fully oxidized, such as $SrTiO_3$, care should be taken to make claims of an MBE growth window based on lattice parameter measurements. In addition to developing substrates that have a reduced lattice mismatch, the key to achieve $BaSnO_3$ films with higher mobilities will be more oxidizing conditions, which is challenging in MBE.

Chapter 3. Sr_3SnO

Sr_3SnO belongs to a family of antiperovskites predicted to host Dirac fermions at the Fermi level due to a protected band crossing. Not only is the promise of an oxide 3D Dirac semimetal interesting in its own right, but polycrystalline samples have been shown to exhibit superconducting transitions. The combination of superconductivity and topologically nontrivial band structure opens up the possibility that Sr_3SnO is an intrinsic topological superconductor, which brings with it the promise of Majorana fermions. However, superconductivity has only been observed in polycrystalline samples which contain additional phases, and thus it is not certain whether Sr_3SnO itself is the superconducting phase. More synthesis work of crystals or, in this case, thin films is necessary to probe whether a phase-pure Sr_3SnO sample indeed exhibits superconductivity. Along with the interesting electronic structure brought about by the unusual anionic 4- charge state of Sn in these materials is extreme air-sensitivity. As such, though UHV thin film growth environments such as MBE are by nature well-suited for air-sensitive materials, the need to remove samples from vacuum to perform *ex situ* measurements and characterization poses significant experimental difficulties.

Here I describe my very preliminary work in getting the growth of Sr_3SnO off the ground at UCSB. Using very broad strokes, growth conditions for crystalline or semi-crystalline films were eventually found and then further improved upon. The crystal structure of Sr_3SnO has a

surprising degree of similarity to two other very relevant materials: YSZ, which is a possible substrate material, and SrO, which could both be an unintentional secondary phase as well as serve as a wetting layer. This translates into nontrivial overlap in crystallographic peak reflections in XRD, which was eventually addressed. The air-sensitivity is also mitigated by the development of an *in situ* capping layer, afforded by the relative ease and convenience of growing ZrO_2 via a metal-organic precursor, which was already a capability of the growth chamber being used for the antiperovskite growth. Though my work was only preliminary, it served as a basis for the very insightful work in the continuation of Sr_3SnO growth by fellow group member Wangzhou Wu [87,88].

3.1 Previous Experimental Work

We begin by briefly summarizing some of the previous experimental work of growth and characterization of single crystals of various A_3BO antiperovskite oxides, where A = Ca, Ba, or Sr, and B = Sn or Pb. We then discuss the studies reporting superconductivity in polycrystalline samples of $Sr_{3-x}SnO$. We finally detail some thin film growth work on $Sr_{3-x}SnO$, which was used in part as a foundation for the experimental work presented in this chapter.

3.1.1 Single Crystals

Single crystals of Sr_3PbO and Ca_3PbO, both of which are expected to host Dirac dispersions at the Fermi level, have been successfully synthesized and electrically characterized. [116,117] Native hole doping due to A-site deficiency was observed in these samples, which could be mildly controlled with synthesis conditions. Low-temperature magnetotransport measurements

were able to access Shubnikov-de Haas (SdH) oscillations owing to the high mobility of the single crystals (> 1000 $cm^2\ V^{-1}\ s^{-1}$). These measurements in both materials were consistent with the existence of 3D Dirac electrons. As will be a theme for all of the experimental work on antiperovksites, care was taken to protect the crystals from air exposure when necessary.

3.1.2 Superconductivity in polycrystalline $Sr_{3-x}SnO$

In 2016, polycrystalline samples of Sr-deficient Sr_3SnO ($Sr_{3-x}SnO$) were reported to exhibit superconductivity with a T_c of ~5 K [21]. As consistent with other antiperovskite oxides, The Sr vacancies resulted in *p*-type behavior. Subsequent work revealed that the superconducting transition was observed for nominal Sr-deficiencies of $0.35 < x < 0.65$ [22]. Though the T_c was constant for all superconducting compositions, the diamagnetic fraction changed with nominal composition. All samples showed evidence of additional phases beyond the $Sr_{3-x}SnO$ [21–23], including SrO, Sn, and SnO. Metallic Sn has a T_c of 3.7 K, and SnO is predicted to be superconducting only under pressure. The authors claim this is sufficient evidence that the superconducting phase is neither of these impurity phases. Furthermore, it is pointed out that there are two Sr-Sn alloys which are known to be superconducting: $SrSn_3$ (T_c = 5.4 K) and $SrSn_4$ (T_c = 4.8 K), however, much care was taken to demonstrate that the expected signatures of these phases were not present in the XRD of the samples, and thus deemed not to be present as one of the additional phases which could possibly be the superconducting phase. While it is noteworthy that the strongest peaks expected for these phases do not appear present even in synchrotron data, the nature of the polycrystalline, mixed-phase samples along with the

remarkably similar T_c's of the Sr-Sn alloys to those measured in the samples calls in the question the possibility that the $Sr_{3-x}SnO$ might not be the superconducting phase.

3.1.3 $Sr_{3-x}SnO$ films grown by MBE

Prior to the beginning of our work, successful synthesis of the Sr_3SnO and $Sr_{3-x}SnO$ phases by MBE had already been demonstrated [118,119]. These studies grew the materials using elemental Sr and Sn sources, along with a 2 % O_2 in Ar mixture for the oxygen supply. The dilute mixture was used to avoid strongly oxidizing conditions, which are detrimental to achieving the strongly reduced Sn^{4-} charge state, and had been demonstrated to be effective for improving the growth quality of $Sr_{3-x}PbO$ films previously [120]. To protect the films from air exposure such that they could be measured, the authors utilized a vacuum suitcase to transfer the sample to an inert atmosphere glovebox, where Au contacts could be deposited. The remaining surface was covered with Apiezon-N grease. Magnetotransport of the films was characterized at low temperatures, which exhibited a maximum mobility of 270 $cm^2\ V^{-1}\ s^{-1}$ at 10K, and thus no SdH oscillations were observed at the magnetic fields used. It was found that adjusting the Sr/Sn flux ratio used during growth could modulate the carrier density due to the changing the concentration of cation vacancies. No superconductivity was reported down to 2K. XRD measurements revealed no impurity phases.

After the beginning of some of the work described below, other authors reported successful growth of $Sr_{3-x}SnO$ by MBE using SnO (from SnO_2) and Sr sources, without the need for co-supply of oxygen [121]. Again, no impurity phases were obvious in XRD, though the reasoning for ruling out the presence of SrO in the films is not robust: they claim that the presence of SrO

mixed with the Sr_3SnO should exhibit a double-peak at a particular off-axis peak based on powder diffraction data, however, this data being a thin film would imply a certain degree of preferred orientation which can hide such a double-peak feature. Samples were transferred to an *in situ* four-probe electrical measurement system without breaking vacuum, and measured down to 2 K. Samples were metallic but did not exhibit superconductivity. No magnetic field could be applied for Hall measurements.

From this previous work, it can be generally expected that a film which possesses the nominal Sr_3SnO phase likely contains some degree of Sr deficiency, and thus is more correctly $Sr_{3-x}SnO$. As such this is likely the case for the films being presented in the following sections. However, for simplicity, and because no electrical measurements were performed, they will be referred to as Sr_3SnO.

3.2 Growth Considerations and Characterization

3.2.1 Substrates

In order to achieve relatively well-oriented epitaxial growth, a substrate must be chosen that is of similar symmetry to the film material, as well as relatively similar lattice constants such that a loose epitaxial relation can be established. Due to the relatively large Sr_3SnO lattice constant of ~5.16 Å [10,11], most traditional perovskite oxide substrate materials are not viable. Interestingly, there is one oxide material that has an almost identical lattice constant: yttria-stabilized ZrO_2 (YSZ). Though this material is not a perovskite, it is cubic, and can be purchased commercially as a substrate. Another option is $LaAlO_3$ (LAO), which has a cubic lattice constant of ~3.79 Å, which is obviously too strongly mismatched (~ -26%) to achieve

the traditional "cube-on-cube" epitaxial relation. However a different scheme can be used – originally developed by Samal *et al* [120] for the growth of another antiperovskite, Sr_3PbO – which utilizes the fact that the [110] lattice spacing of LAO, which is $\sqrt{2a}$~ 5.36 Å, is relatively close to the [100] lattice parameter of Sr_3SnO (~ 4% mismatch). This induces the epitaxial film to grow with a 45° in-plane rotation relative to the substrate, as illustrated in Fig. 3.1.

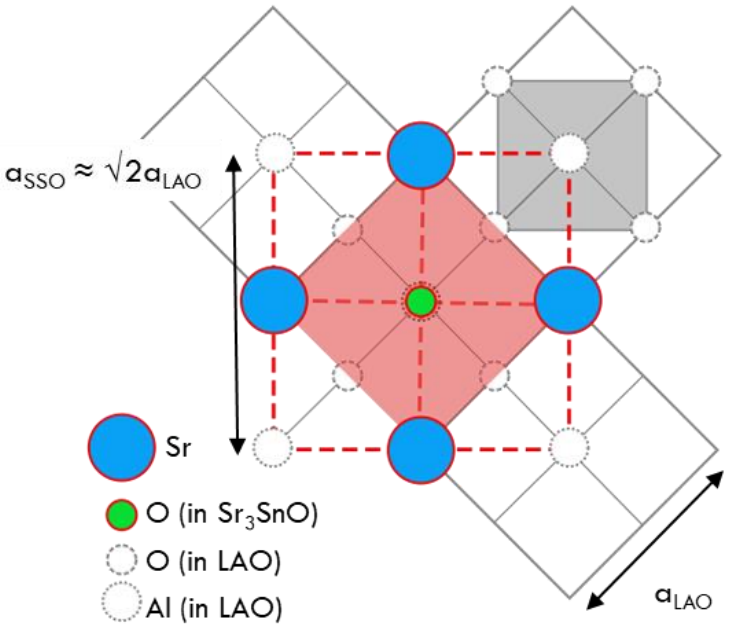

Figure 3.1 – Schematic representation of the epitaxial relationship of a (001) $LaAlO_3$ (LAO) substrate and a (001) Sr_3SnO epitaxial film, indicating the 45° in-plane rotation of the Sr_3SnO layer to access the √2a lattice parameter of the LAO.

3.2.2 Protective capping layer

The need for the development of an *in situ* capping layer was necessary for any sort of *ex situ* measurement to be performed on the films. In order to accurately study the underlying material, there are three (somewhat obvious) requirements that must be met by the capping

layer: (1) It must protect the underlying film from air exposure to a sufficient degree, (2) it must not react with the film at the interface, and (3) the deposition of the capping layer must not harm the film in the process. Thin metallic capping layers could in theory be used for *ex situ* structural measurements such as XRD. However, electrical measurements were an eventual goal of the project, and metallic capping layers could not be used in this case. As such, a fourth requirement was added: (4) The capping layer material must be sufficiently insulating such that electrical measurements are representative of the underlying film only, and not of the capping layer in parallel. Electrical measurements naturally require the ability to make electrical contact with the protected Sr_3SnO layer through the capping layer, which will be addressed later.

With these requirements in mind, the oxide ZrO_2 was found to be an excellent capping layer candidate. ZrO_2 has a wide band gap (> 5 eV) and is a poor oxygen conductor (in the absence of dopants) [122] which partially suffices conditions (1) and (4) (thickness of the layer will be important to ultimately satisfy condition (1)). It is possible to grow ZrO_2 by a chemical vapor deposition method using a metal-organic precursor, zirconium tert-butoxide or ZTB, injected into the growth chamber through a gas-inlet port in the same way other metal-organic precursors are used introduced in hybrid MBE [123]. This method of growth is advantageous for requirement (3) as only a flux of ZTB is necessary to grow ZrO_2 – it is not necessary to co-supply an oxidant, which might harm the underlying oxygen-sensitive film. The temperature of the substrate must be sufficiently high to decompose the MO molecule such that the ZrO_2 grows effectively. However, this range of temperatures is lower than the growth temperatures of the Sr_3SnO layer, which lowers the probability that it might react.

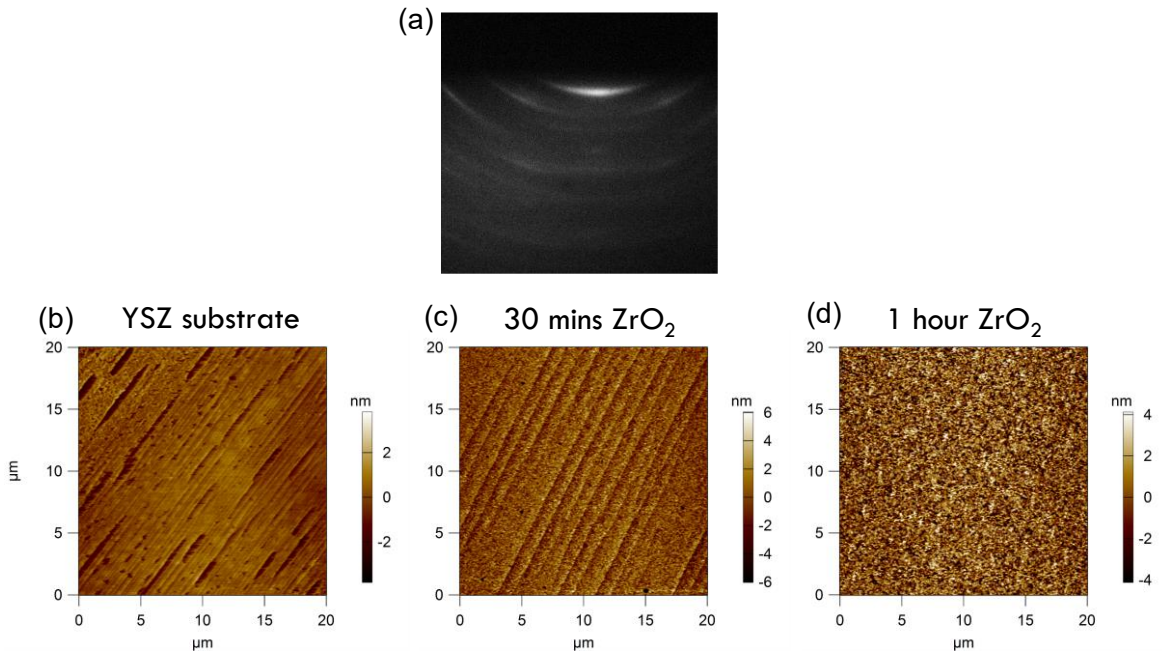

Figure 3.2 – (a) RHEED of ZrO_2 layer grown using ZTB, indicating polycrystalline growth. (b) AFM image of a bare YSZ substrate, and AFM images of a YSZ substrate after (c) 30 minutes of ZrO_2 growth and (d) 1 hour of ZrO_2 growth.

It was found that growth of ZrO_2 proceeded in a polycrystalline fashion. This sometimes appears as a slightly textured polycrystalline form, as seen in the RHEED in Fig. 3.2(a). Due to the poor crystallinity and rough surface, x-ray methods were not useful for determining the thickness of the ZrO_2 film. Instead, AFM was used to determine the length of growth time necessary to eliminate the appearance of the substrate steps, as seen in Fig. 3.2(b).

The necessary growth conditions for a sufficiently protective ZrO_2 layer were explored in tandem with early growth trials of Sr_3SnO by trial and error. It was first confirmed, as had been predicted, that removing a sample of (presumably) Sr_3SnO from vacuum to ambient air would result in its rather rapid oxidation and degradation. This was easily observed as follows: the sample would be removed from the growth chamber with a shiny, specular surface, and over time (~minutes), the surface could be seen to turn dull and opaque. When Sr_3SnO films were

grown, different substrate temperatures and growth times for the ZrO_2 layer were explored. It was found that a substrate temperature of ~375 °C and a growth time of 90 minutes sufficiently protected the underlying film from degradation in air [87].

3.2.3 Characterization methods

RHEED: As a first check of the growth conditions for the Sr_3SnO, and indeed the only characterization tool available before the development of the ZrO_2 capping layer, RHEED was a valuable tool. Without a verified window of growth conditions, the RHEED pattern which resulted from a particular set of conditions could be used as a rough estimate as to how close to "good" growth conditions they were: the closer to crystalline and 2D, the better.

XRD: Once the protective capping layer became viable, XRD was used to determine if the resulting growths actually contained the intended species. As will be shown, this in itself was not trivial.

Cross-section SEM: The most informative characterization tool for the early development of Sr_3SnO growth was cross-section SEM imaging. These were achieved using an SEM system with an in-situ focused ion beam (FIB) source, used for cutting through the ZrO_2 protective layer and exposing the cross-section of the film. This was necessary, as the sample could not be cleaved outside of the SEM as it would oxidize immediately. This also meant that this characterization method was necessarily destructive to the film. Once the underlayer is exposed to air upon removing the sample from the SEM chamber, the oxidation would spread throughout the entire film. Covering the exposed cross-section area with Pt post-imaging was not explored.

3.3 MBE Growth of Sr_3SnO

3.3.1 Growth using Sn source

Early attempts to grow Sr_3SnO via MBE in the Old Oxide system were carried out using metallic Sr and Sn sources along with a small flow of O_2, following recent (at the time) reports of successful growth [118,119]. YSZ substrates were used. Growth conditions consisting of different substrate temperatures and different Sr/Sn flux ratios were first evaluated by the RHEED pattern observed: those which produce either amorphous (hazy) or polycrystalline (rings) patterns were assumed to be far from the optimal conditions. It was found that using a substrate temperature of 450 °C and Sr/Sn ratios of ~6, the phase grown was polycrystalline,

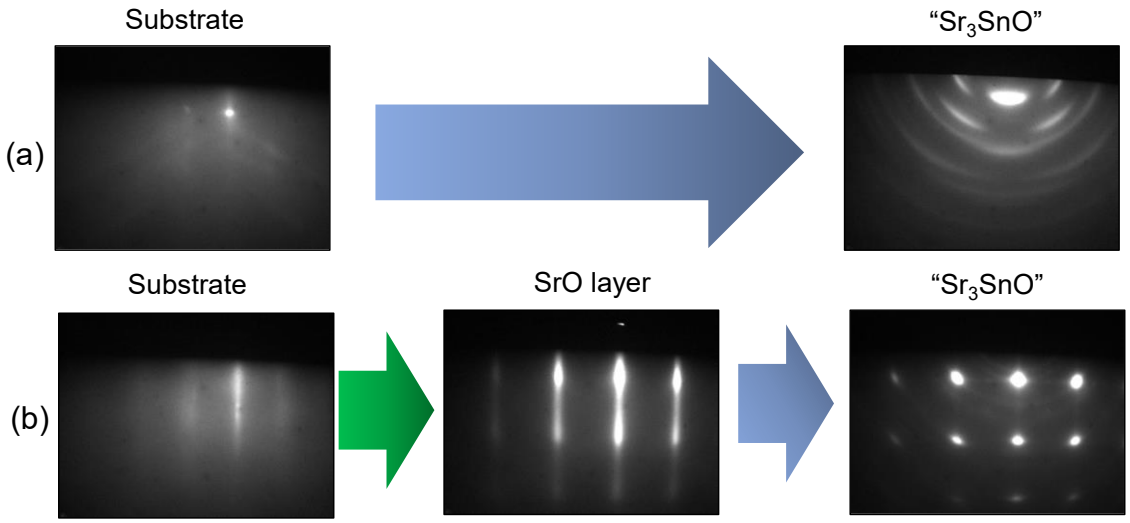

Figure 3.3 – RHEED images of the stages of Sr_3SnO growth attempts using Sn and O_2 sources, with (a) no SrO wetting layer, and (b) with a SrO wetting layer. The presence of the SrO layer resulted in a 3D crystalline phase, while the growth on the bare substrate resulted in a polycrystalline phase.

as seen in Fig. 3.3(a). The use of SrO buffer layers was then explored, again suggested from earlier reports [118]. SrO has a cubic rock salt crystal structure with an almost identical lattice constant to that of Sr_3SnO (~5.16 Å), and perhaps could serve as a wetting layer for the antiperovskite phase. SrO was grown via co-deposition of Sr and O_2-plasma, which produced streaky RHEED patterns (Fig. 3.3(b)). Subsequent attempts to grow Sr_3SnO then produced a spotty RHEED pattern, indicating a three-dimensional crystalline phase had been stabilized. A weak ring-like pattern can also be seen in the RHEED, indicating the presence of a secondary polycrystalline phase.

Most of these early growth attempts using the Sn metal source could not be further characterized, as the ZrO_2 capping layer had not been fully developed yet (indeed, many were used to test whether the capping layer was sufficiently protective). However, a limited number were able to survive *ex situ* measurements once the capping layer was developed. The XRD of one such sample is shown in Fig. 3.4(a). Due to the very similar lattice constants, the YSZ substrate 002 peak dominates over the Sr_3SnO and SrO 002 peaks. While both SrO and YSZ do not exhibit 00-*odd* peaks, Sr_3SnO does, though their intensity is extremely weak: structure factor analysis shows that 001 peaks exhibit only 0.92% of the intensity of 002 peaks. Thus, even though the heterostructure does not exhibit any other peaks that can positively identify the Sr_3SnO phase, this does not necessarily mean it is not present. This sample was also characterized via cross-section SEM, shown in Fig. 3.4(b**)**. First, we see what is proposed to be the SrO layer, which is the relatively thin dark layer immediately above the YSZ substrate. Though it exhibited a streaky (i.e. 2D) RHEED pattern, it appears to have a rough interface with the layer above. Next, the lighter, thicker layer above is the proposed Sr_3SnO layer, and above that, the thick ZrO_2 capping layer, which exhibits some internal porosity. The Sr_3SnO

layer also appears to contain pockets of a secondary phase as told by the different regions of different (darker) contrast which are distributed throughout. The interface between the Sr_3SnO layer and the ZrO_2 is also quite uneven, which is unlikely an effect from intermixing with the ZrO_2, but instead likely represents the as-grown surface profile, which would confirm the 3D-like appearance of the RHEED pattern. However, the roughness of the interface between the SrO and Sr3SnO may indicate some interfacial reaction, as again, the SrO as-grown surface appears 2D from RHEED. Though neither of the phases in the "Sr_3SnO" layer of this sample could be positively identified, as will be shown later, the lighter majority phase is very likely Sr_3SnO. The ZrO_2 here is also of relatively poor quality, likely due to the growth temperature used during its growth.

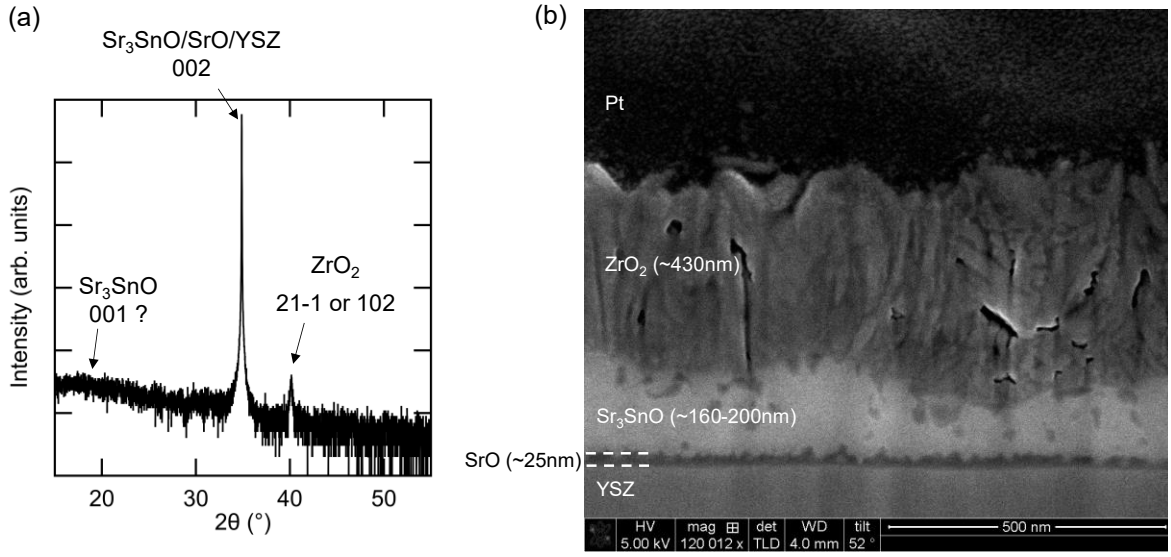

Figure 3.4 – (a) XRD measurement of a $Sr_3SnO/SrO/YSZ$ heterostructure grown using Sn and O_2 sources. The strong YSZ 002 substrate peak hides the lattice-matched 002 peaks of both the SrO and (assumed) Sr_3SnO layer. The 001 Sr_3SnO peak may not be visible in thin, poor-quality films. (b) Cross-section SEM image of the sample in (a), showing the various layers. Multiple phases can be seen in the nominal Sr_3SnO layer. The surface of the Sr_3SnO layer is 3D-like, which explains the appearance of spots in RHEED. The ZrO_2 capping layer is somewhat porous.

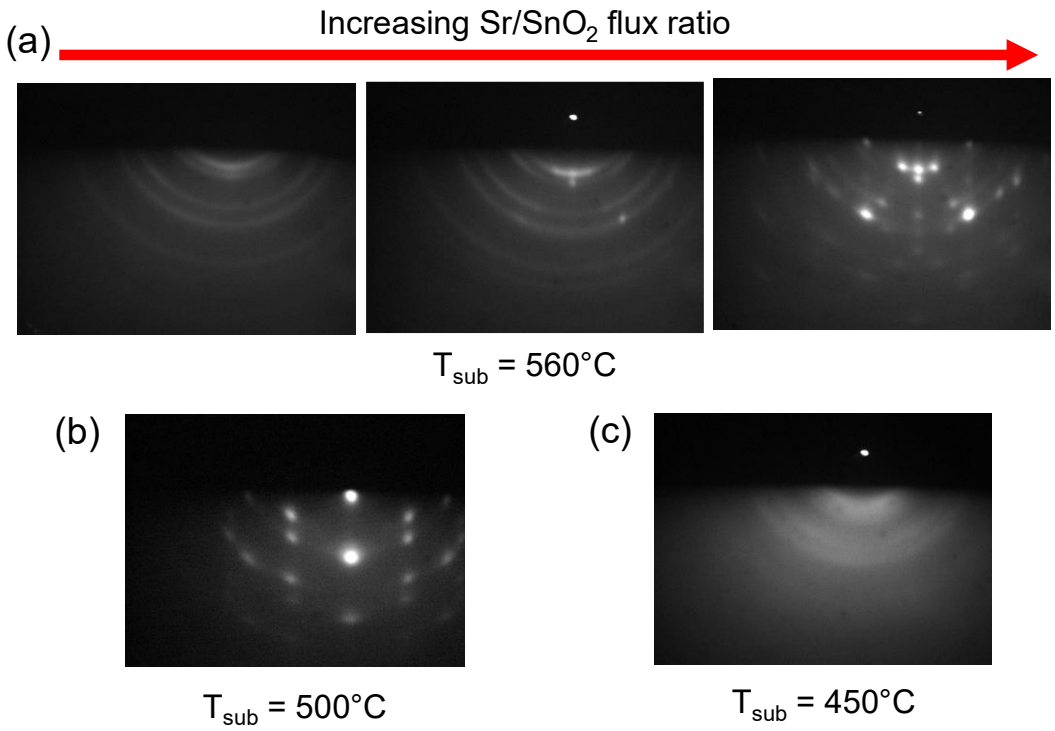

Figure 3.5 – (a) RHEED images after attempts to grow Sr_3SnO at various Sr/SnO_2 BEP ratios at a substrate temperature of 560 °C. (b) RHEED image of an attempted Sr_3SnO layer using high Sr/SnO_2 flux ratio and a substrate temperature of 500 °C, and (c) RHEED image of an attempted Sr_3SnO layer using a similar flux ratio as in (b) at a substrate temperature of 450 °C.

3.3.2 Growths using SnO_2 source

Subsequent growth studies were carried out using SnO_2 as both the Sn and O sources, due to the most abundant species supplied by it being SnO which supplies the stoichiometric ratio of Sn:O. In contrast to $BaSnO_3$, the strongly reducing conditions of the vacuum are highly advantageous for realizing the Sn^{4-} valence state of Sr_3SnO. For these growths, LAO was also used as the primary substrate so as to ensure that the 002 peak (whether from Sr_3SnO or SrO) could be distinguished. As before, initial growth attempts relied primarily on RHEED to find conditions which produced a crystalline phase. Mixed phases of a 3D crystalline phase and a

polycrystalline phase were found at substrate temperatures of 560 °C, which differed from the use of Sn as a source as no SrO buffer/wetting layer was needed to achieve a crystalline phase. Higher Sr/SnO_2 flux ratios produced RHEED patterns which were increasingly dominated by the crystalline spots, indicating that these higher ratio conditions were growing a higher relative amount of the crystalline phase, as seen in Fig. 3.5(a). Growth temperatures lower than 500 °C seemed to produce only polycrystalline films even at high Sr/SnO_2 flux ratios, as seen in Fig. 3.5(c).

It was later found that a higher growth temperature, and even higher flux ratios (~10-30) could achieve relatively streaky RHEED patterns for the nominal Sr_3SnO layers, with some slight spottiness still superimposed. *Ex situ* XRD revealed only a broad 002 peak, as seen in Fig. 3.6(a). To attempt to tease out the peak morphology of purely SrO, films consisting of just SrO were also grown (and capped with ZrO_2) for XRD. SrO consistently produces streaky RHEED patterns, as seen in Fig. 3.6. The XRD of this film showed a similarly broad 002 peak in the same position as would be expected for Sr_3SnO. This indicated that the presence or morphology of a 002 peak alone could not provide sufficient evidence to positively identify the presence of the Sr_3SnO, even though it would be unlikely for a purely SrO film to result from sources of SnO and Sr. A Sr_3SnO sample with a SrO buffer layer was attempted as well, and the resulting RHEED pattern from both layers is shown in Fig. 3.6. Both produce a streaky RHEED pattern, and the Sr_3SnO layer seems to have less of a spotty character than layers grown without the SrO buffer layer. Still, the XRD reveals only a single broad SrO/Sr_3SnO 002 peak, with no obvious peak separation or asymmetry, indicating that the extreme similarity of the lattice constants would not allow for the differentiation of separate SrO and Sr_3SnO

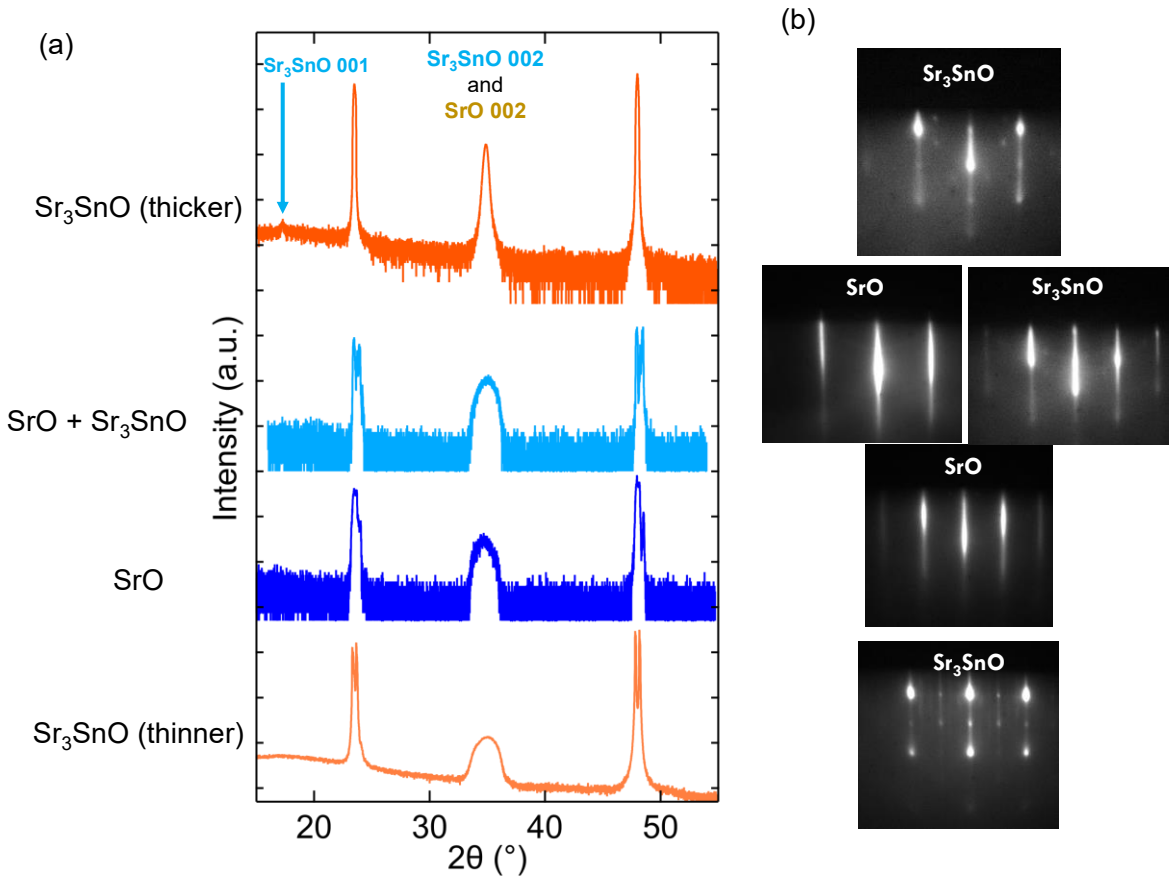

Figure 3.6 – (a) On-axis XRD scans of various films structures as indicated to the left of each scan. The central peak around 35° 2θ could correspond to either SrO 002 or Sr_3SnO 002. The sharp peaks near 24 ° 2θ and 48 ° 2θ are the LAO substrate peaks. The weak Sr_3SnO 001 peak can only be identified in the thickest film. (b) RHEED images of the various layers of the films shown in (a).

phases, and thus again no explicitly positive identification of the presence of Sr_3SnO could be made. Finally, it was found that by growing a nominal Sr_3SnO layer for a long growth time, thus making the layer thicker and increasing the scattering probability of the 001 reflections, a very faint but present 001 peak could be identified, as seen in Fig. 3.6, which confirmed the presence of the Sr_3SnO phase in a <001> oriented fashion. However, the possibility remained that multiple phases could be present.

Cross-section SEM images were taken of these films to further investigate the resultant phases. As can be seen in Fig. 3.7, the nominal "Sr_3SnO" layers possess areas of mixed contrast, indicating the presence of multiple phases. On the other hand, the intentional SrO layers present as single-phase regions with relatively smooth interfaces, as evidenced by Fig. 3.7(b), which corroborates the ubiquity of streaky RHEED patterns observed after SrO growth. The "Sr_3SnO" layers exhibit multiple phases regardless of the presence of SrO buffer/wetting layers, indicating that the mixed phase growth is a result of the growth conditions of the layer itself and not its nucleation conditions. The morphology of these films and the distribution of the secondary phases is quite different from that seen in films grown using metallic Sn (Fig 3.4b). Though purely speculation at this point, this may indicate that a Sr_3SnO phase was successfully grown using the metallic Sn source as well, though it was never confirmed via

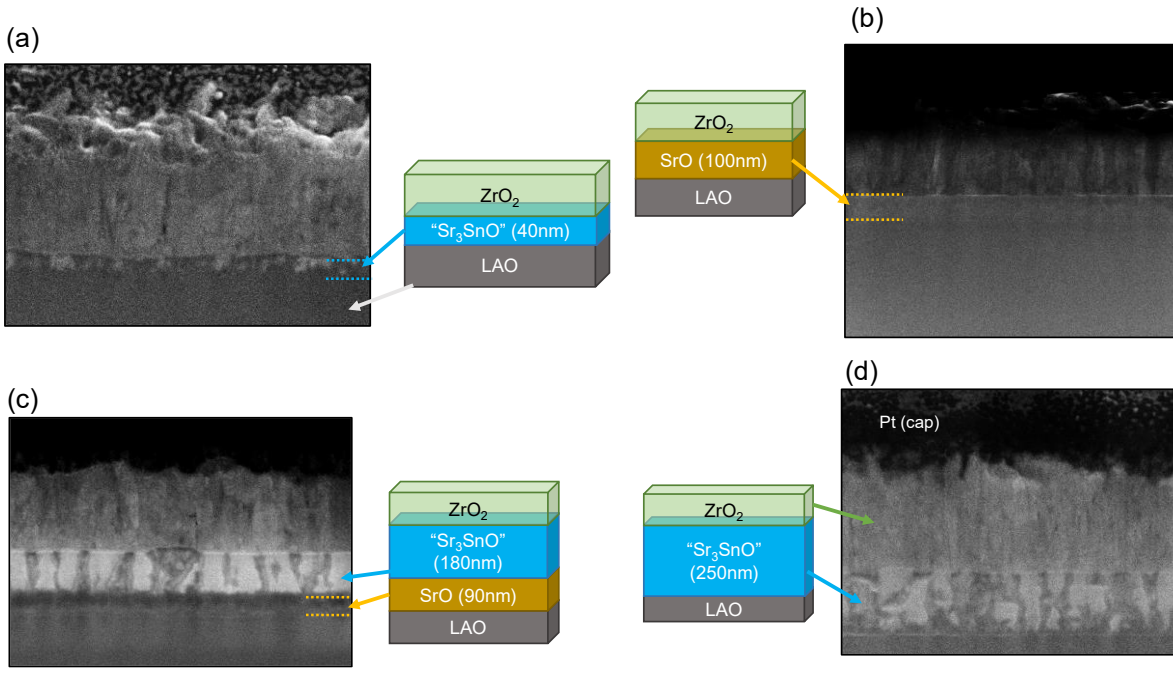

Figure 3.7 – Cross-section SEM images of various Sr_3SnO and SrO film structures as indicated by the schematic cartoons. The XRD and RHEED for these structures was shown in Fig. 3.6.

XRD. This would also indicate that the Sn source resulted in different growth modes, likely one which involved liquid Sn droplets on the surface.

Finally, we note an interesting phenomenon which occurred following the growth of a number of Sr_3SnO layers. Minutes after the growth ended, higher-order reconstructions could be seen to appear along the <110> surface directions, as shown in Fig. 3.8. In most samples which exhibited streaky RHEED, half order reflections along the <110> directions were persistent. However, after some growths, even higher order reconstructions were observed in the <110> directions. It was found that the appearance of the reconstructions was not temperature-dependent, but time-dependent, as they appeared for only a few minutes after growth had stopped, regardless of the substrate temperature, and then would disappear. As the primary streaks of the RHEED pattern were not altered after the appearance of the higher-order reflections, this does not seem to pertain to a phase change. The cause of these temporary higher-order reflections is not known. To speculate, perhaps their appearance signals the ordering of surface adatom species that had not yet incorporated into the film, though the fact that the reconstructions do not appear until minutes after growth makes this unlikely. Another speculative cause might be that they signal a changing stoichiometry of the film, possibly due to post-growth loss of some species due to evaporation. A likely candidate would be Sr, as Sr vacancies are generally expected in Sr_3SnO samples unless growth conditions are tightly controlled.

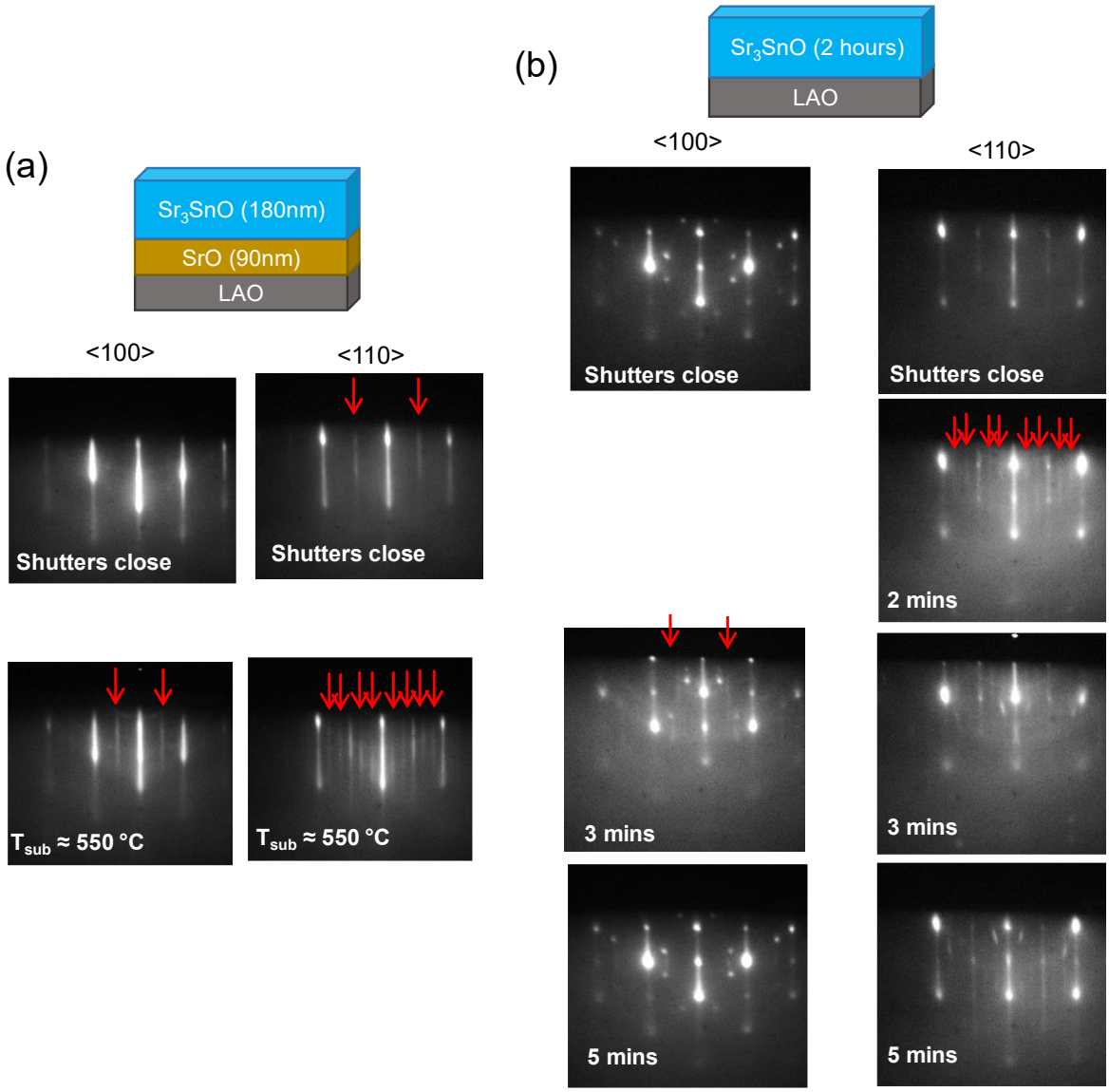

Figure 3.8 – RHEED images after the growth of two different Sr_3SnO samples, showing the appearance of higher-order reconstruction streaks along the <110> azimuths. In (a) the substrate temperature was allowed to cool following growth, and in (b) the temperature was held constant.

3.3.3 Conclusions

In conclusion, very broad growth conditions were identified which produced crystalline or semi-crystalline films. While SrO wetting layers proved useful for achieving better

crystallinity (as told by RHEED) for Sr_3SnO films grown using Sn as a source, this was found not to be necessary for growths using SnO_2 as a source. The extremely weak structure factor of the 001 peaks of Sr_3SnO were eventually observed in thick films, which confirmed that the antiperovskite phase had indeed been grown, though the presence of secondary phases could not be ruled out. Cross-section SEM measurements confirmed that all films presented here consisted of multiple phases. It was also shown that ZrO_2 grown via a CBE approach using the metal-organic ZTB is a viable protective capping layer which allows for *ex situ* structural characterization such as XRD and SEM. A limited number of cross-section SEM measurements on films grown using Sn as a source seemed to indicate a different growth mode compared to SnO_2 source growths. However, these growths also utilized different substrates, and the Sr_3SnO phase was never positively identified by XRD for Sn-source growths, and thus this point remains rather speculative.

Chapter 4. Ferroelectricity and Superconductivity in $SrTiO_3$ films

$SrTiO_3$, though being the first discovered oxide superconductor, still poses many questions to theorists concerning its superconducting mechanism. The extreme diluteness of the carrier density needed to condense into a superconducting state alone places it convincingly in "unconventional" superconductor territory. Furthermore, it lies very near to a ferroelectric transition in its pure bulk form, and this incipient ferroelectricity has in many ways been shown to be tied to the superconducting state. However, much of the past work investigating this link tends to assume – for understandable reasons – that the superconductivity emerges from a homogenously paraelectric, centrosymmetric phase, and the fluctuations or soft-mode dynamics which are present in this state provide the pairing glue [38,52–54]. However, through the many years of experimental research on $SrTiO_3$ (and indeed many perovskite oxides in general) it has been shown that the strongly polarizable lattice has the tendency to form locally polar regions in the nominally paraelectric state. For $SrTiO_3$-based systems which have been tuned into a ferroelectric ground state, these static polar distortions grow and percolate as the ferroelectric transition is approached, eventually coalescing into a globally polarized state [124–126]. It is also from deep in the polar regime where the most enhanced

superconducting T_c's have been reported. However, there are strong indications that these so-called polar nanodomains exist down to the lowest temperatures even in systems which do not exhibit a transition to a globally polarized state [124,125,127–129], and thus there is a strong possibility that superconductivity in $SrTiO_3$ always emerges in the presence of some degree of broken inversion symmetry.

In addition to the interesting structural link, superconductivity in $SrTiO_3$ has also displayed remarkable insensitivity to magnetism. Here we describe a study of alloying magnetic Eu into strained films of $SrTiO_3$, which served as a continuation of a previous study which showed that, up to 3% Eu, the superconductivity in the $Eu_xSr_{1-x}TiO_3$ films was unaffected relative to non-alloyed films [130]. We observe superconductivity survives up to Eu concentrations of at least $x = 0.14$, and no suppression of the superconducting T_c at $x = 0.09$. Also at $x = 0.09$, we observe a loss of a sharp ferroelectric transition seen in strained $SrTiO_3$ films, indicating that the Eu has affected the polarizability of the lattice. The evolution of the superconducting properties along with the loss of global polar order as Eu is added is discussed in terms of possible connections between the superconducting state and broken inversion symmetry.

4.1 Background information

4.1.1 Introduction

The finding that the various methods used to drive $SrTiO_3$ towards a ferroelectric ground state also result in enhanced T_c's (Fig. 4.1) is commonly interpreted as being the result of the ferroelectric quantum critical point (QCP) whose fluctuations putatively lead to Cooper pairing [41,51,52,54,56]. This picture is contradicted by the fact that, in many of the studies,

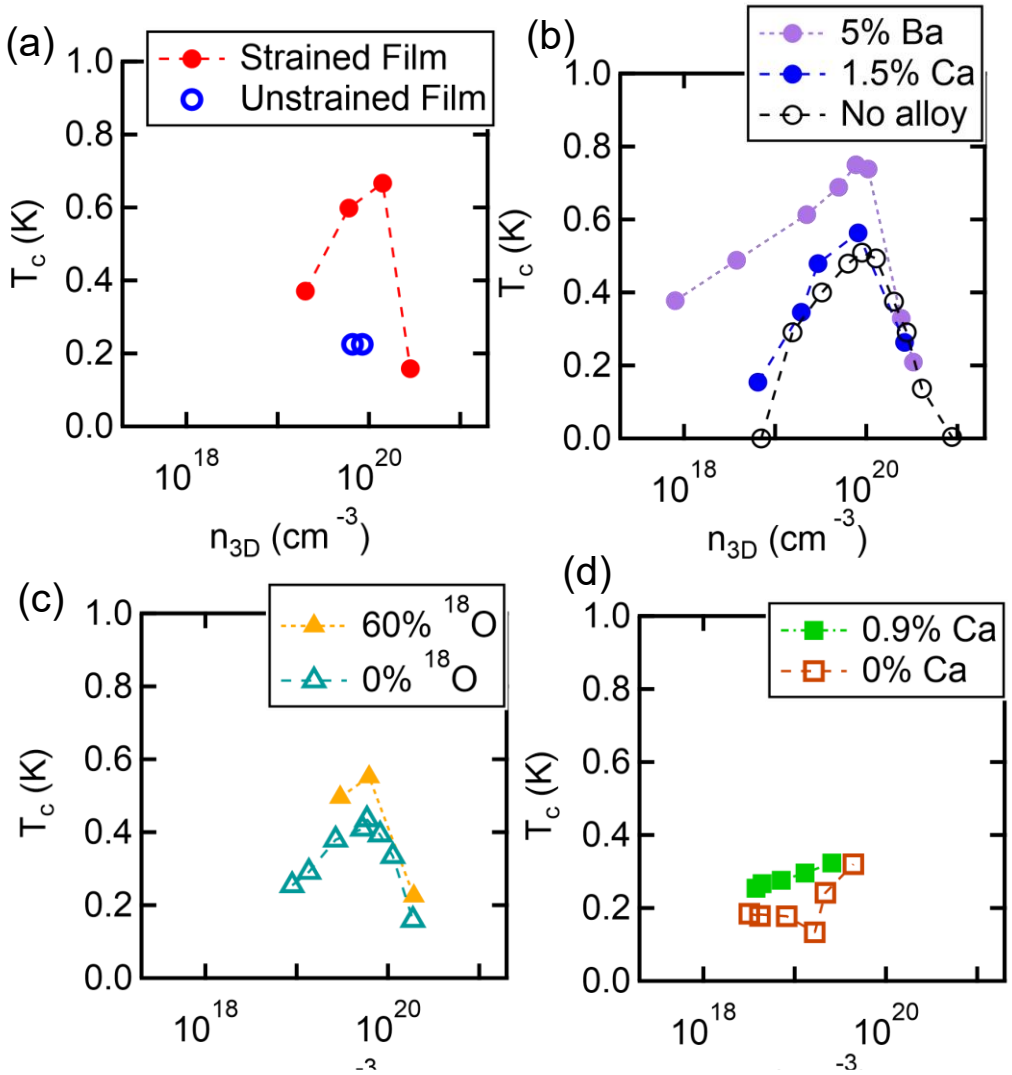

Figure 4.1 – Superconducting domes of $SrTiO_3$ showing enhancement of T_c induced by various ferroelectric tuning methods(taken from reports in the literature): (a) Epitaxial film strain (Sm doped) (ref. [31], (b) Ca- and Ba-substituted $SrTiO_3$ crystals (Nb doped) (ref. [49]), (c) ^{18}O isotopic exchanged $SrTiO_3$ crystals (La-doped) (ref. [49]), (d) Ca-substituted $SrTiO_3$ crystals (reduced) (ref. [41])

superconductivity emerges from a truly polar ground state [31,41,46,49,51], and indeed some of the highest T_c's reported to-date have been observed in samples that were already strongly in the polar regime upon entering the superconducting state [31,46,49]. Due to the presence of broken inversion symmetry, this is reminiscent of superconductivity at the $LaAlO_3/SrTiO_3$

interface [131–133] which is strongly linked to the presence of Rashba-like antisymmetric spin-orbit coupling (ASOC) [133–135] due to the broken inversion symmetry of the interface. There are also signs of local T_c enhancement in $SrTiO_3$ systems near twin boundaries [136] and deformation-induced dislocations [137,138] both of which exhibit locally polar characteristics [127,139].

Ferroelectricity requires broken inversion symmetry. In the case of proper ferroelectrics, the ferroelectric phase transition is characterized by a structural transition to a polar point group which produces a macroscopic polarization that is switchable. At the unit cell level this can be manifested by the displacement of ions from centrosymmetric positions, which lead to local electric dipoles. If these displacements are in-phase and global throughout the crystal, the result is a macroscopic polarization and globally broken inversion symmetry. If spin-orbit effects are present as well, Rashba-like ASOC in noncentrosymmetric (i.e. ferroelectric or polar) superconductors can lead to mixed parity superconducting states, opening the door to possible topological (*p*-wave) superconductivity [140–142].

In an effort to promote the discussion that broken inversion symmetry in the superconducting state of $SrTiO_3$ and related systems is not only possible, but may be *necessary*, we will briefly review some of the properties and experimental findings relevant to this class of materials. We will focus primarily on strained $SrTiO_3$ films but will compare to $Ba_xSr_{1-x}TiO_3$ and $Ca_xSr_{1-x}TiO_3$ crystals as well where relevant, in an effort to highlight some of the key similarities *and* differences of these systems which could perhaps strengthen this idea.

4.1.2 Different types of ferroelectric ground states

As pointed out by Tomioka *et al* [49], the types of the ferroelectric ground states differ among strained $SrTiO_3$ films [46], $Ca_xSr_{1-x}TiO_3$ crystals [41,49], and $Ba_xSr_{1-x}TiO_3$ crystals [49], all of which exhibit enhanced superconducting T_c's in the polar state. Ca^{2+} substitution is known to induce ferroelectricity linked to an off-centering of the Ca^{2+} ion in the larger Sr^{2+} site, leading to a <110> polarization direction [40]. Ba^{2+} substitution, on the other hand, induces a low-temperature phase transition to a rhombohedral *R*3m phase, which exhibits broken inversion symmetry due to Ti^{4+} displacement along a [111] pseudocubic axis [42,49]. Strained [001] $SrTiO_3$ films, on the other hand, exhibit displacement of the Ti atom in the [001] tetragonal direction [46,143] (Fig. 4.2). Though the polar ground state is different in all of

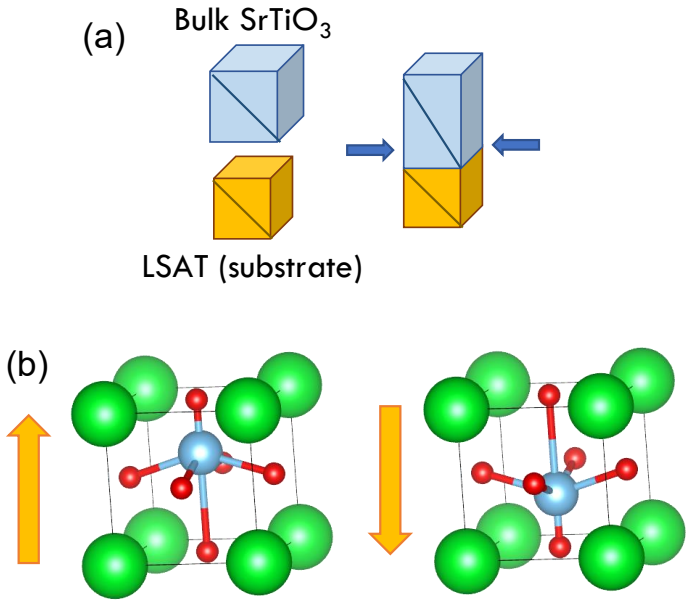

Figure 4.2 – (a) Schematic cartoon illustrating the tetragonality induced by compressive strain of $SrTiO_3$ grown on LSAT substrates. (b) Illustrations of the two possible polar unit cell distortions induced by compressive epitaxial strain of [001] $SrTiO_3$ films (displacements not to scale)

these examples, they all result in an enhancement of the superconductivity relative to (nominally) paraelectric $SrTiO_3$ [31,41,46,49] (Fig. 4.1).

4.1.3 Polar metals

The presence of metallicity and ferroelectricity (or ferroelectric order) has long been thought to be mutually exclusive, though originally proposed by Anderson and Blount in 1965 [144]. The presence of free carriers would be expected to screen the various electrostatic interactions responsible for stabilizing the ferroelectric order, preventing the displacement of the ions and prohibiting the breaking of inversion symmetry. However, in recent years the existence of a number of polar metals has been shown [145,146], in which the structural order parameter of ferroelectricity (broken inversion symmetry) persists even in a metallic state. In order for charge carriers to propagate freely, the total electric field (polarization) must be fully screened by localization of some of the carriers at the boundaries, but the structural order parameter can still exist so long as the carrier screening of the local dipoles is incomplete or sufficiently weak. For doped semiconductors which become polar metals, increasing the carrier concentration leads to an increasingly stronger screening effect of the structural polarity and a reduction in the polar displacements [147]. Above some critical carrier concentration, the carriers will be able to sufficiently screen the structural polarity such that it will be become unfavorable, and the polar metal state will be destroyed for a centrosymmetric metal [145].

Measurements of the dielectric constant as a function of temperature can often be used to identify a transition to a polar state by the presence of an peak at the transition temperature [41,45]. However, these are not possible in the presence of charge carriers. An

alternative measurement is optical second harmonic generation (SHG), which is sensitive to the breaking of inversion symmetry [46,72]. A ferroelectric transition appears as a sharp increase in the detected second harmonic intensity, due to the sudden appearance of a noncentrosymmetric structure (Fig. 4.3**)**. Structural characterization at low temperatures can be another method to identify the presence of a polar space group [49,148]. Thermodynamic probes can also show a kink or behavior change at the transition temperature, including heat capacity [148], thermal expansion [41,149], and sound velocity [41]. Raman spectroscopy can be used as well [41]. Resistive anomalies or kinks are commonly observed at the transition temperature [31,41,46,49,51,148,150], and are likely a result of the sudden turning-on of carrier localization to screen the spontaneous polarization.

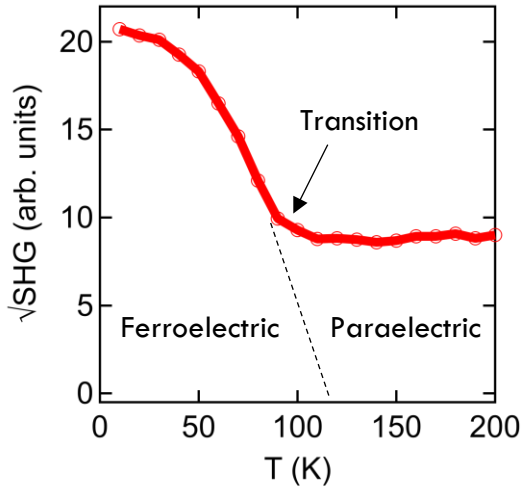

Figure 4.3 – Representative SHG measurement of a ferroelectric transition in a compressively strained $SrTiO_3$ film.

4.1.4 Nanodomains and the order-disorder transition

The ferroelectric transition in $SrTiO_3$ (and $BaTiO_3$) was originally believed to be well-described by a displacive model, in which a long-range polarization develops spontaneously at the phase transition due to the softening of a transverse optical (TO) phonon mode. However, evidence has been continuously growing that point to the existence of locally polar regions in the paraelectric phase of perovskites believed to be governed by a displacive dynamics [124,128,129,151–154] which would instead imply an order-disorder phase transition model, or more likely a combination of order-disorder and soft mode models [155,156]. The dominant interactions that cause these polar nanodomains to form and coalesce may be different among different perovskite systems [125,145,156], but they share the commonality of being partially due to a highly polarizable lattice, and the general behavior of them is the same: at temperatures above the transition temperature T^*, in the nominally paraelectric phase, there exist microscopic regions of correlated polarization, i.e. polar nanodomains. The polarization directions between domains are uncorrelated and random and thus the global state is one that averages out to a nonpolarized, high-symmetry state. At T^*, the existing dipolar regions reorient, forming a long-range ordered state. The phase transition is thus one from a globally random, locally ordered phase to a globally ordered phase.

For $Ca_xSr_{1-x}TiO_3$ (> 0.2% Ca), the transition is known to be strongly of the order-disorder type [41,126]. Dipole-dipole (short range) interactions between off-center Ca atoms form polarized clusters (nanodomains) above the ferroelectric transition temperature T^*, which grow and percolate as temperature is lowered, eventually coalescing into a global ferroelectric state below T^*. For $SrTiO_3$ and $Ba_xSr_{1-x}TiO_3$, dipole-dipole interactions induced by *A*-site off-centering do not play a role in forming nanodomains in the paraelectric phase. Nonetheless, as

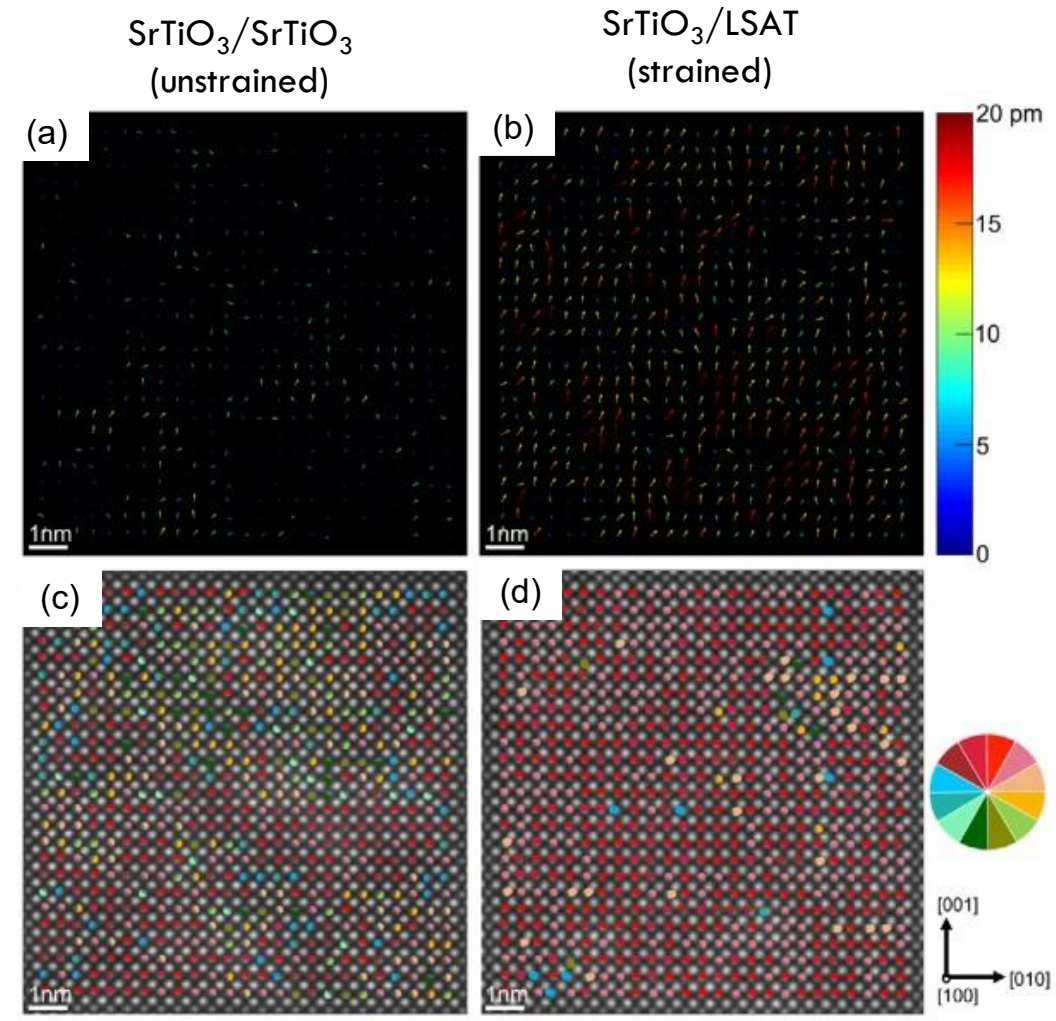

Figure 4.4 – Cross-section HAADF-STEM images overlaid with off-center Ti polarization vectors for $SrTiO_3$ films grown on (a),(c) $SrTiO_3$ and (b),(d) LSAT. The arrows in the top row of figures indicate the magnitude and orientation of the polarization vectors. The images in the bottom row display the direction of the polarization vectors overlaid on the HAADF image, with the color representing a 30° interval of polarization directions. (e) schematic illustrating how the polarization vector is measured (right) and representative zoomed-in region (left). Adapted with permission from ref. [124]

mentioned above, numerous signatures of polar nanodomains have been found in the paraelectric phase of these nominally displacive ferroelectrics, and recently they have been visualized using high-resolution scanning transmission electron microscopy (STEM) in the paraelectric phase [124,125,157–159]. For $Ba_xSr_{1-x}TiO_3$ (and $BaTiO_3$) the cause of the local structural distortions has been attributed to local strains from point defects [154,159].

In $SrTiO_3$, the nanodomains manifest as off-centered Ti columns, as illustrated in Fig. 4.4. These nanodomains are *static*, in that they do not fluctuate on the time scale of the STEM measurements (10s-100s of seconds) and perhaps longer. The picture of point defects being the underlying source of the nanodomains is not as strongly supported for $SrTiO_3$. No large concentrations of impurities exist other than dopants, which have actually been shown to break up nanodomains [125]. Instead, it is likely that long-range electrostatic interactions are what lead to the formation of nanodomains and ultimately to the ferroelectric transition in $SrTiO_3$, rather than more short-range interactions such as local strains or dipolar impurities [125,145,160]. Indeed, at least for strained $SrTiO_3$, the presence of polar nanodomains may actually be a *requirement* for the entrance to a ferroelectric phase, i.e., a high configurational entropy makes the ferroelectric phase transition unfavorable. For films that do not exhibit a ferroelectric transition due to over-doping, nanodomains are absent at room temperature [125], though they may form at lower temperatures.

The purely displacive model for the ferroelectric phase transition is thus not applicable for $SrTiO_3$, and likely as well for many other prototypical displacive perovskites. Some authors have even argued that, due to the ubiquity of components of both displacive and order-disorder dynamics in many perovskite oxides, classification as one or the other is too restrictive and unnecessary [161].

4.1.5 Relaxor ferroelectrics

The discussion of locally polar regions draws similarities to the relaxor ferroelectrics, which do not exhibit a spontaneous macroscopic polarization in the ground state, but instead consist of locally ordered but globally disordered polar nanoregions (within a single crystal domain) [162–165]. Relaxors have been heavily studied for years, and thus we will not attempt provide any significant insights here, other than mentioning that the dynamics of relaxors upon cooling are very similar to that of the order-disorder transition of "true" ferroelectrics: at high enough temperatures, there are no correlated regions, and the entire matrix is truly paraelectric. As the temperature lowers but stays above a characteristic "freezing" temperature T_f, locally polar domains start to form, which possess a random distribution of dipole moment directions and thus the global polarization is zero. As T_f is approached, the domains continue to grow and percolate to some degree – however, upon cooling through T_f, and in the absence of strong external electric field, the domains are prevented from coalescing into a macroscopically polarized domain, and thus no true phase change is experienced. Instead, the dynamics between the domains slow down and they remain in a globally disordered but locally ordered state [163].

Many true ferroelectric perovskites are transformed into relaxors when compositional disorder is introduced, the most seminal being based around mixtures involving $PbTiO_3$ [163–165], but also mixtures of many other perovskite oxides [40,42,166,167]. Unintentional intrinsic impurities in strained $SrTiO_3$ films produces a crossover to a relaxor state as well [168]. Strained $SrTiO_3$ films grown on $NdGaO_3$ (~1.2% compressive strain) via PLD do

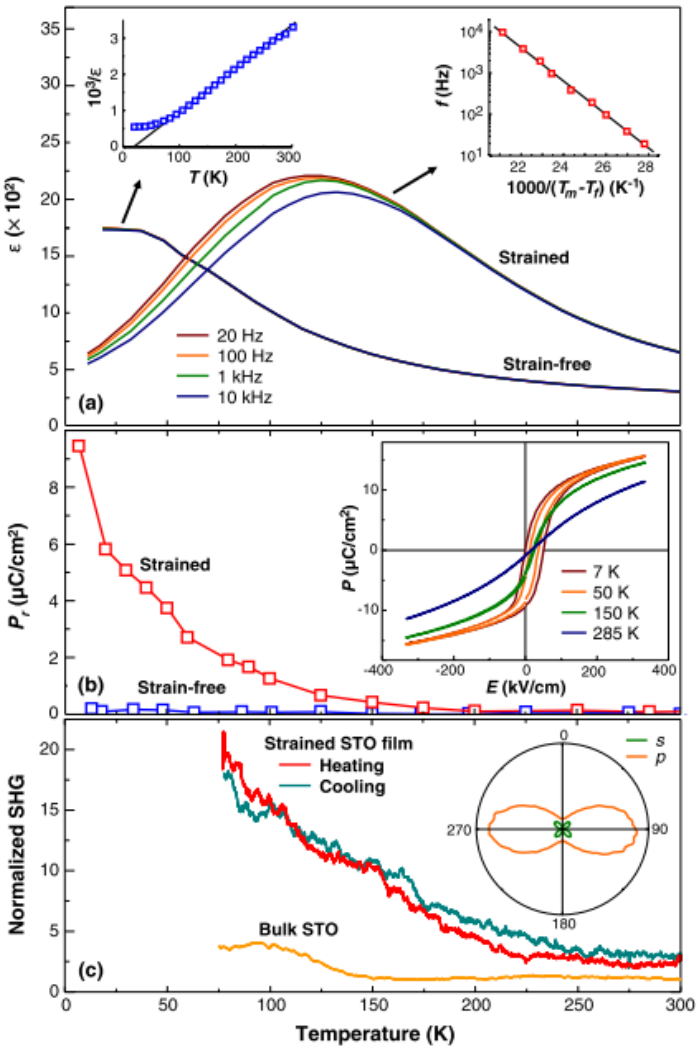

Figure 4.5 – (a),(b) Temperature dependence of (a) dielectric constant and (b) remanent polarization of 60-nm-thick $SrTiO_3$ (STO) film on $NdGaO_3$ (strained) and 100-nm-thick $SrTiO_3$ film on $SrTiO_3$ (strain-free) (c) SHG signals for the strained $SrTiO_3$ film and a $SrTiO_3$ crystal. Insets: (a) Curie-Weiss law and Vogel-Fulcher law fits, (b) *P*-*E* hysteresis loops of the strained film, and (c) SHG polar plots. Adapted with permission from ref. [168].

not exhibit a sharp SHG transition (Fig. 4.5**)**, which is inconsistent with MBE-grown films [46]. The undoped PLD-grown films also exhibit the key dielectric properties of a relaxor ferroelectric, i.e. a broad, frequency-dependent hump in the dielectric constant as a function of temperature and 'slim-loop' hysteresis curves [162], again in contrast to strained films grown

via MBE [45]. This is likely the result of energetic point defects introduced by PLD and highlights the sensitivity of the global ferroelectric transition in $SrTiO_3$ to disorder.

4.1.6 Destruction of ferroelectricity and superconductivity

If superconductivity does indeed rely on the presence of broken inversion symmetry, then the destruction of the polar phase would be expected to result in the suppression of superconductivity.

In strained $SrTiO_3$ films grown below a critical thickness (~40 nm), ferroelectricity and superconductivity both disappear simultaneously [169]. The ferroelectricity is suppressed by depolarization fields which the thinner films feel more strongly [160], though the presence of free carriers likely contributes to destabilizing the ferroelectricity at larger thicknesses than in undoped films [72]. However, there is *a priori* no reason the superconductivity should disappear in this thickness regime in the absence of strong carrier depletion (which was mitigated in this study).

The ferroelectric ground state in strained films is also suppressed above a certain critical carrier density in $SrTiO_3$ films [31,46]. Above a carrier density of $\sim 3 \times 10^{20}$ cm^{-3}, no signatures of a global ferroelectric transition are observed, and no nanodomains are seen to exist at room temperature [125]. As the carrier density is increased in the underdoped films, both the length scale of the nanodomains and the magnitude of the correlated Ti displacements is seen to decrease, indicating the progressively stronger screening effects of the charge carriers until finally the carriers completely screen the local (and global) polarity [125] (Fig. 4.6). The influence of disorder from the dopant atoms may contribute to the total ferroelectric

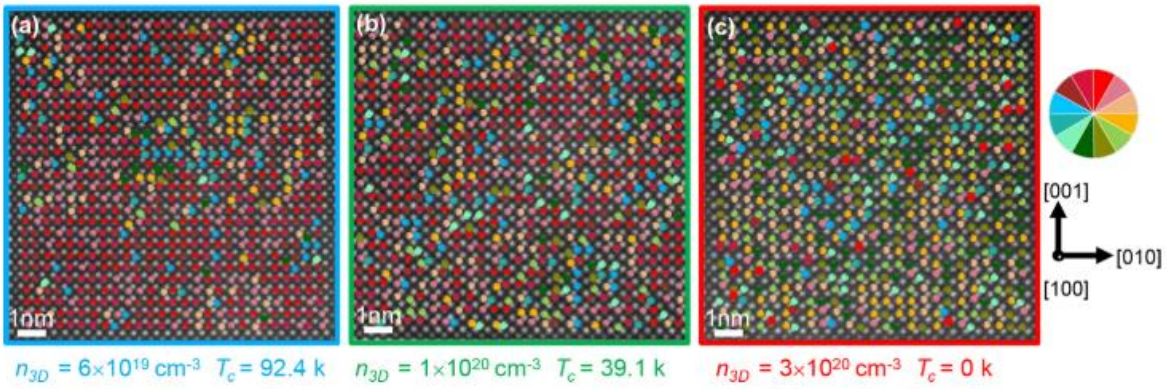

Figure 4.6 – Polarization orientation maps of Sm-doped $SrTiO_3$ films with carrier concentrations of (a) 6×10^{19} cm^{-3}, (b) 1×10^{20} cm^{-3} , and (c) 3×10^{20} cm^{-3} . HAADF-STEM images obtained from cross-sectional sample. The color scale corresponds to 30° intervals of polarization directions. Adapted with permission from ref. [125].

suppression to some degree as well. At the carrier density where no nanodomains are seen at room temperature, the superconducting T_c is un-enhanced and increasing the carrier density any further results in a total loss of superconductivity. Thus, the critical carrier density where both room temperature nanodomains and the global ferroelectric transition are suppressed coincides with the suppression of superconductivity. For $Ba_xSr_{1-x}TiO_3$ crystals, the loss of ferroelectricity at a critical carrier concentration also appears to roughly coincide with the critical carrier concentration for suppressing superconductivity as well [49].

For $Ca_xSr_{1-x}TiO_3$ crystals, superconductivity survives up to higher carrier densities than the critical concentrations at which the ferroelectric transition is lost (as told by resistive anomalies) [41,49]. However, thermal expansion measurements indicate that a smeared anomaly continues to survive above this resistive anomaly critical carrier concentration [149], which may be consistent with a relaxor-like state (i.e. locally polar). Thus, the presence of some degree of local polarity may remain at carrier densities above that which destroys the global transition, and thus superconductivity may still be present in a locally polar phase.

4.1.7 Possibility of broken inversion symmetry in paraelectric $SrTiO_3$

If the source of superconductivity is indeed linked to the presence of broken inversion symmetry, then nominally paraelectric bulk $SrTiO_3$ with no impurities (other than dopants or oxygen vacancies) would not be expected to exhibit superconductivity. Polar nanodomains have been visualized in unstrained undoped $SrTiO_3$ at room-temperature, which have a smaller length scale than those in strained films [124](Fig 4.4(c)). The existence of these at room temperature would imply that they remain to low temperatures as well and likely grow larger. SHG of bulk $SrTiO_3$ crystals exhibits a small but finite signal which gradually increases as temperature is lowered [168](Fig. 4.5(c)). Bulk $SrTiO_3$ exhibits signatures of polar regions at low temperatures via Raman spectroscopy [128] and resonant piezoelectric spectroscopy [127] as well. Their presence shows that the nominally paraelectric low temperature phase from which superconductivity emerges actually possesses locally broken inversion symmetry. It should be noted that this should not be conflated with a relaxor-like state, however, as dielectric constant measurements clearly show different behavior between bulk $SrTiO_3$ and relaxors. Instead, this simply suggests that states of locally polar order may be exhibited in a variety of forms.

In strained $SrTiO_3$ films which exhibit even a small degree of strain relaxation, a sharp ferroelectric transition seen in SHG is lost. However, nanodomains are still observed at room temperature, and *enhanced* superconducting T_c's remain [157]. The length scale of the nanodomains remains comparable to fully strained films, though they are more likely to take random polarization directions than preferably in- and out-of-plane as in fully strained films.

Thus, though a global ferroelectric transition may appear to be destroyed by strain relaxation (at least as told by SHG), the presence of large regions of locally broken inversion symmetry remains and the superconducting T_c's remain enhanced relative to unstrained films.

Taken all together, there is strong evidence that the examples of globally polar superconducting $SrTiO_3$ do not necessarily represent a vastly different structural phase than the nominally paraelectric superconducting $SrTiO_3$, but rather the two represent extrema of a continuous spectrum in which the length scale of the polar order changes from local domains to global. The differences in T_c, then, are simply manifestations of the length scale of the polar regions. The overall polar displacements contained within the polar regions may play a role as well. All of this points to a motivation to reconsider the models of superconductivity in $SrTiO_3$ in that it may always co-exist with broken inversion symmetry, and conversely may not exist once even small regions of local polarity are lost.

4.1.8 Magnetic insensitivity

Superconductivity in $SrTiO_3$ films exhibits other peculiarities as well. These include coexistence of the superconducting state with magnetism [132,170], upper critical field (H_{c2}) values that exceed the paramagnetic (Pauli or Clogston-Chandrasekhar) limit [29,171–173], and an apparent insensitivity of T_c to suppression by the presence of magnetic impurities [29,31,130]. The latter is in direct violation of the Abrikosov-Gor'kov (AG) theory of paramagnetic impurities in an s-wave superconducting host [174]. The high H_{c2}'s could be related to thin film effects [171] or purely multiband effects [29,175,176], and the sensitivity to magnetic impurities could be somewhat explained by multiband effects [177]. However,

there are possibilities that ASOC induced by the presence of broken inversion symmetry (particularly for the cases involving $SrTiO_3$ interfaces) could contribute to these effects as well [170,178–183]. Certain theories have even emerged that hint at the possibility of topological superconductivity induced by the Rashba ASOC [184,185], though it should be stressed that this is essentially impossible to prove through magnetic response alone [140]. Still, the unique responses with possible explanations lying in Rashba ASOC are intriguing for the implications of noncentrosymmetric superconductivity.

4.2 Description of MBE growth and characterization

4.2.1 Description of the present study

Previously, it was shown that strained Sm-doped $Eu_xSr_{1-x}TiO_3$ films still exhibited no suppression of the superconducting properties attributed to the magnetic Eu up to 3% [130]. These films also exhibited sharp SHG upturns (for those which were fully strained) of the global ferroelectric transition as well. As Eu^{2+} is magnetic – as well as the Sm^{3+} dopant atoms – this seemed to indicate that AG theory was being violated. The response of a superconductor to different kinds of disorder can be useful for identifying underlying symmetry. For instance, sensitivity to non-magnetic disorder is a signature of unconventional superconductivity [186,187]. On the other hand, spin-triplet superconductivity may be relatively insensitive to magnetic disorder [140,179]. In order to further probe this unusual response to magnetism, films with even higher amounts of Eu^{2+} were grown and characterized for the present study. It is found that superconductivity is eventually suppressed above Eu concentrations of ~14%. Remarkably, rather than purely being an effect of the magnetism, the

suppression may result from the effect of Eu suppressing the polarizability of the lattice and destroying the (local) broken inversion symmetry.

4.2.2 $EuTiO_3$ capping layer

A majority of previous studies of $SrTiO_3$ films strained on LSAT substrates utilized films with thicknesses on the order of ~180 nm [31,46,130]. While these demonstrated that it was possible to achieve fully strained films at such thicknesses, partial strain relaxation was occasionally observed and in general was not easily predictable. As mentioned above, sharp SHG transitions can be broadened by even a small degree of strain relaxation [157], making identification of the ferroelectric transition difficult. It was deemed necessary to produce fully strained films for the present study such that SHG could be reliably utilized to probe the presence of the global FE transition, and thus necessitates the growth of thinner films which have a lower likelihood of relaxing.

A main reason for the use of relatively thick $SrTiO_3$ films was to avoid the well-known issue of strong surface depletion at low temperatures [188,189], which would strongly influence the observed low-temperature properties. This depletion of carriers limits the study of superconducting properties due to the strong carrier density dependence of T_c in $SrTiO_3$ [35], such that in films thinner than ~100 nm, superconductivity could not be observed due to too many carriers being depleted. The strong depletion also manifests in non-uniformity of the carrier density throughout the thickness of the film, which can complicate interpretations of low-temperature transport and the superconducting T_c [189].

In order to satisfy both of these limitations – i.e. thin, fully strained films that do not exhibit strong carrier depletion – it was found to be necessary to include a capping layer to separate the $SrTiO_3$ surface from air and thus reduce surface depletion effects. Through work lead by Hanbyeol Jeong, using a thin (~10 nm) capping layer $EuTiO_3$ was found to solve this problem. $EuTiO_3$ has a similar lattice constant to $SrTiO_3$, and both Eu and Sr exist in 2+ valence states. Thus, the $EuTiO_3$ capping layer will not relax on $SrTiO_3$ and the similarity of valence states avoids the formation of a polar discontinuity. The utilization of the $EuTiO_3$ capping layer allowed for strained $SrTiO_3$ films to exhibit superconductivity down to as thin as 40nm, which had not previously been possible/reported. Additionally, it was found that doping the $EuTiO_3$ was necessary to achieve Ohmic contacts and to avoid band-bending effects such that the underlying $SrTiO_3$ film could be electrically characterized. Following from the success of this strategy, the $Eu_xSr_{1-x}TiO_3$ films of the present study were kept thin (to avoid relaxation) and were capped with $EuTiO_3$ (to suppress carrier depletion). One remaining note is that the superconducting T_c's of the thin, $EuTiO_3$-capped $SrTiO_3$ films were found to be slightly suppressed relative to thicker, uncapped strained $SrTiO_3$ films [189]. The precise reason requires further study. It could be purely a thickness-related effect [169], but it could also be related to the presence of the (antiferromagnetic) $EuTiO_3$ capping layer, or a combination of both. The superconducting properties of the present Eu-alloyed heterostructures will thus be quantitatively compared only to those of analogous $EuTiO_3/SrTiO_3$/LSAT heterostructures [169,189].

4.3 Growth of $Eu_xSr_{1-x}TiO_3$ films

4.3.1 Methods: Hybrid MBE growth and characterization

Heterostructures of $EuTiO_3/Eu_xSr_{1-x}TiO_3$/LSAT were grown via hybrid MBE, which has been described previously and will briefly be described here. Prior to the growth of the samples used for this study, calibration samples were grown to identify the optimal growth conditions for achieving stoichiometric Sm-doped $Eu_xSr_{1-x}TiO_3$ and Sm-doped $EuTiO_3$ films at the growth temperature of 1000 °C (thermocouple temperature). Along with lattice parameter measurements, the presence of the (2 × 1) RHEED surface reconstruction is also indicative of stoichiometric growth conditions, for both $SrTiO_3$ and $EuTiO_3$ [71]. The optimal TTIP/*A* ratio is slightly different for $SrTiO_3$ and $EuTiO_3$, and as may be expected, the optimal TTIP/(Sr+Eu) ratio for $Eu_xSr_{1-x}TiO_3$ was found to roughly interpolate between the optimal ratios for the two end members.

Before each growth, BEP flux measurements were performed for the Sr, Eu, and Sm cells overnight. Growths were performed utilizing 10 mm × 10 mm (001) LSAT substrates backed with 300 nm of Ta for improved heat conduction. The substrate was annealed at 1050 °C for 20 minutes prior to cooling to the growth temperature of 1000 °C. The Sr, Eu, and Sm effusion cells were heated to ~10-20 °C higher than their intended growth temperatures prior to growth to facilitate outgassing as well as to ensure full temperature equilibration at the growth temperature to achieve a consistent, well-conditioned flux once growth was initiated. The TTIP flux is also conditioned prior to growth by opening the gas injection line isolation valve a few hours before growth and performing a beam flux calibration procedure, which also serves to flush the gas line and thus achieve a conditioned flow. The Sm:$Eu_xSr_{1-x}TiO_3$ layers were grown

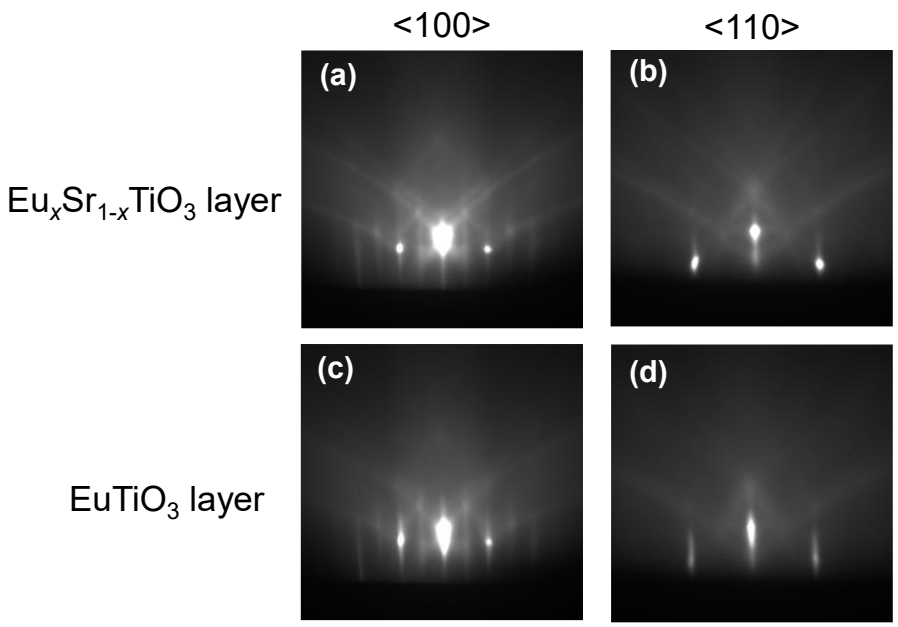

Figure 4.7 – RHEED images taken along the <100> and <110> surface azimuths after the growth of the (a),(b) $Eu_xSr_{1-x}TiO_3$ and (c),(d) $EuTiO_3$ layers of a single heterostructure sample grown on LSAT

to thicknesses of 70-100nm to prevent strain relaxation. The Sm:$EuTiO_3$ capping layer was grown immediately following Sm: $Eu_xSr_{1-x}TiO_3$ layer after allowing the Eu effusion cell to heat up to from the lower alloying flux temperature to the higher temperature needed for pure $EuTiO_3$ growth, also including an overheating step for temperature equilibration. The Sm dopant cell temperature was kept at the same temperature as was used for the $Eu_xSr_{1-x}TiO_3$ layer. The thermocouple temperature was maintained at 1000 °C during the entire process. The Sm:$EuTiO_3$ capping layer was grown to be ~10 nm.

RHEED is utilized to monitor the growth in-situ. Fig. 4.7 shows representative diffraction patterns for stoichiometric Sm:$Eu_xSr_{1-x}TiO_3$ and Sm:$EuTiO3_3$ layers (both belonging to the same heterostructure sample), displaying the (2 × 1) surface reconstruction. RHEED intensity oscillations at the beginning of growth were generally observed for both the $Eu_xSr_{1-x}TiO_3$ layers

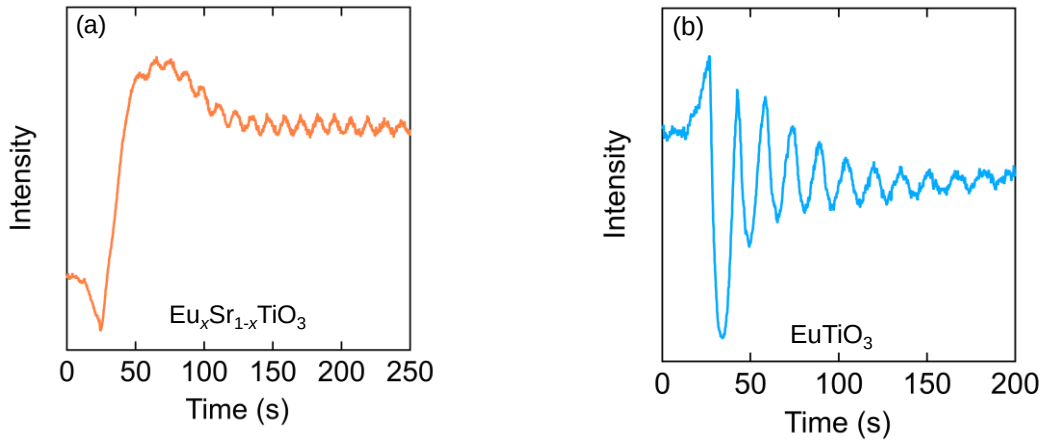

Figure 4.8 – RHEED intensity oscillations at the beginning of growth of a (a) $Eu_xSr_{1-x}TiO_3$ layer and (b) $EuTiO_3$ layer, indicating layer-by-layer growth

and the $EuTiO_3$ cap layers (Fig. 4.8), and can be utilized as a real-time measurement of the growth rate such that the thickness of the layer can be relatively well controlled.

For the present study, two series of strained Sm:$EuTiO_3$/$Eu_xSr_{1-x}TiO_3$ heterostructures were grown. In the first series (Series A), the alloy concentration of Eu in the Sm:$Eu_xSr_{1-x}TiO_3$ layer was kept constant at a nominal value of x = 0.05 (5% Eu) and the Sm^{3+} dopant concentration was varied. In the second series (Series B), the Sm^{3+} dopant concentration was kept nominally constant in the optimally doped range (determined by the doping density of the sample in Series A that produced the highest superconducting T_c) and x was varied. The nominal Eu concentration was estimated by the ratio of Sr/Eu beam equivalent pressures (BEPs) used during growth and corresponded to x = 0.05, 0.10, and 0.20 for series B. The relative Sr/Eu stoichiometry of the films was also determined by x-ray photoelectron spectroscopy (XPS), which estimated the stoichiometry of these be closer to x = 0.09, 0.14, and 0.30, respectively [90]. Note that the optimally doped sample from series A (sample A3) is also used

as the $x = 0.09$ sample in Series B (sample B1). Summaries of film parameters and measured properties are presented in Tables 4.1-4.3.

On-axis x-ray diffraction (XRD) measurements were carried out using a Philips Panalytical X'pert thin film x-ray diffractometer to assess out-of-plane lattice parameters and film thicknesses via Laue thickness fringes. The evolution of ferroelectric order was measured using optical second harmonic generation (SHG) from 10 K to 200 K. Ultrafast laser pulses with 800 nm center wavelength, 40 fs duration, and 10 kHz repetition rate were focused to a spot size of 30 μm, as described previously [46]. Each point shown is the average of many points taken continuously as the temperature is changed. The SHG intensity shown is the average of the points within a chosen temperature interval.

Al shadow masks were used to deposit Ti(50nm)/Au(250nm) ohmic contacts on the corners of the sample by electron beam evaporation. Sheet resistance (R_S), Hall carrier density (n_{3D}), and Hall mobility (μ) were measured from 300 K to 2 K in van der Pauw (vdP) geometry using a Quantum Design Dynacool system. Longitudinal resistance (R) measurements between 14 mK and 1 K were performed in a dilution refrigerator (Oxford Instruments Triton) using low-frequency lock-in techniques. The superconducting transition temperature T_c was defined as the temperature at which $R/R_n = 0.05$, where R_n is the resistance measured at 1 K. Upper critical field (H_{c2}) measurements at 20 mK were performed on the Series A samples with the highest measured T_c values. Sample A1 was measured with $\boldsymbol{H}$ oriented out of the plane of the sample (oop), while samples A2 and A3 were measured with $\boldsymbol{H}$ oriented in the plane of the sample (ip) (i.e., $\boldsymbol{H} \parallel \boldsymbol{n}$ and $\boldsymbol{H} \perp \boldsymbol{n}$, respectively, where $\boldsymbol{n}$ is the film surface normal). Here H_{c2} is defined as the field at which $R/R_n = 0.5$. Only one orientation of H_{c2} was measured for each sample due to sample degradation between scans [90].

4.3.2 Results: Series A

Results from the XRD measurements of Series A films are shown in Fig. 4.9. All exhibit a single 002 film peak indicating that both the Sm:$EuTiO_3$ cap and the Sm:$Eu_xSr_{1-x}TiO_3$ are fully strained to the LSAT substrate, with the out-of-plane lattice parameter a_{op} close to the value expected for fully strained, stoichiometric films ($a_{op} = 3.930 \pm 0.001$ Å). Laue fringes indicate good crystallinity and smooth surfaces of the heterostructures. The exception is sample A2, which exhibits a small degree of strain relaxation ($a_{op} \approx 3.927$ Å). The strain relaxation in A2 causes the slight dampening of the Laue thickness fringes, which are stronger in the other

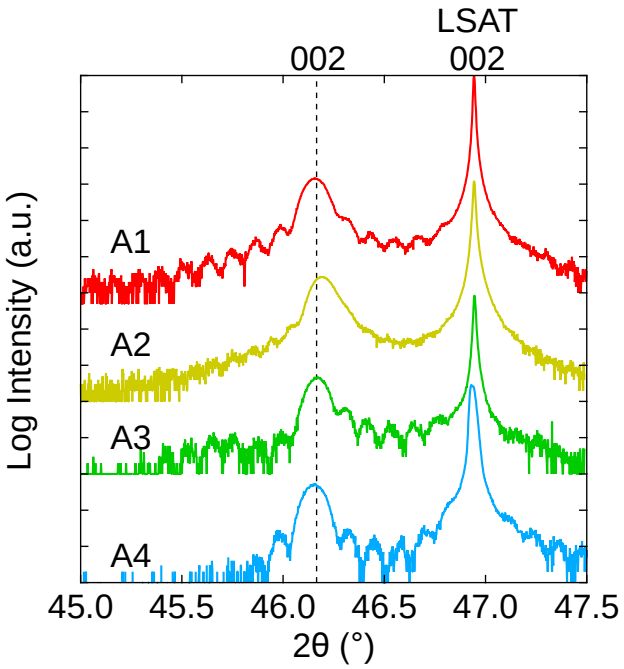

Figure 4.9 - XRD for Series A films. The dotted line represents the fully strained, stoichiometric 002 lattice parameter. Adapted with permission from ref. [90].

Table 4.1 - Summary of properties for Series A samples. The Sm:$Eu_xSr_{1-x}TiO_3$ thickness was measured via XRD thickness fringes and subtracting the estimated thickness of the Sm:$EuTiO_3$ capping layer. Adapted with permission from ref. [90].

Sample	n_{RT} (cm^{-3})	$Eu_xSr_{1-x}TiO_3$ Film Thickness (nm)	T_c (mK)
A1	6.3×10^{19}	68	290
A2	7.4×10^{19}	92	330
A3	9.8×10^{19}	75	400
A4	1.2×10^{20}	68	75

samples. The period of the thickness fringes corresponds to the total thickness of the heterostructure, and the measured thickness values for the Sm:$Eu_xSr_{1-x}TiO_3$ layer are given in Table 4.1, after subtracting the estimated thickness of the Sm:$EuTiO_3$ capping layer. A representative reciprocal space map of sample A4 is shown in Fig. 4.10.

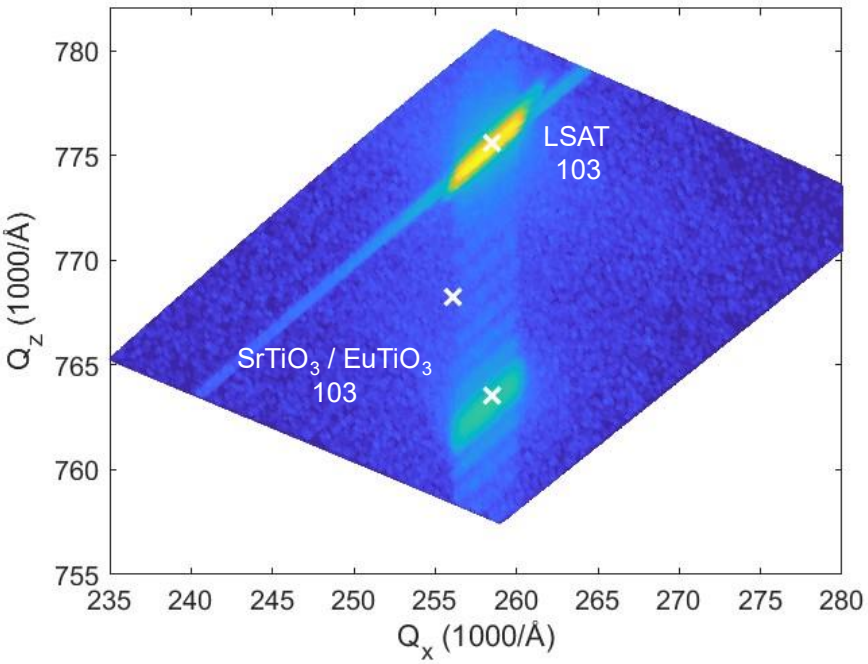

Figure 4.10 - Summary of properties for Series A samples. The Sm:$Eu_xSr_{1-x}TiO_3$ thickness was measured via XRD thickness fringes and subtracting the estimated thickness of the Sm:$EuTiO_3$ capping layer. Adapted with permission from ref. [90].

The room temperature 3D carrier density values n_{RT} for the Series A films were calculated from the Hall resistance, using the total heterostructure thickness as both layers contribute to conduction in the normal state [189]. The n_{RT} values were estimated to be 6.3×10^{19} cm^{-3}, 7.4×10^{19} cm^{-3}, 9.8×10^{19} cm^{-3}, and 1.2×10^{20} cm^{-3} for samples A1 - A4, respectively (Table 4.1). Figure 4.11(a) shows R_s as a function of temperature (T) for Series A films, all of which exhibit metallic behavior down to 2 K. In Fig. 4.11(b), the slight upturn in R_s around ~7 K - 8 K

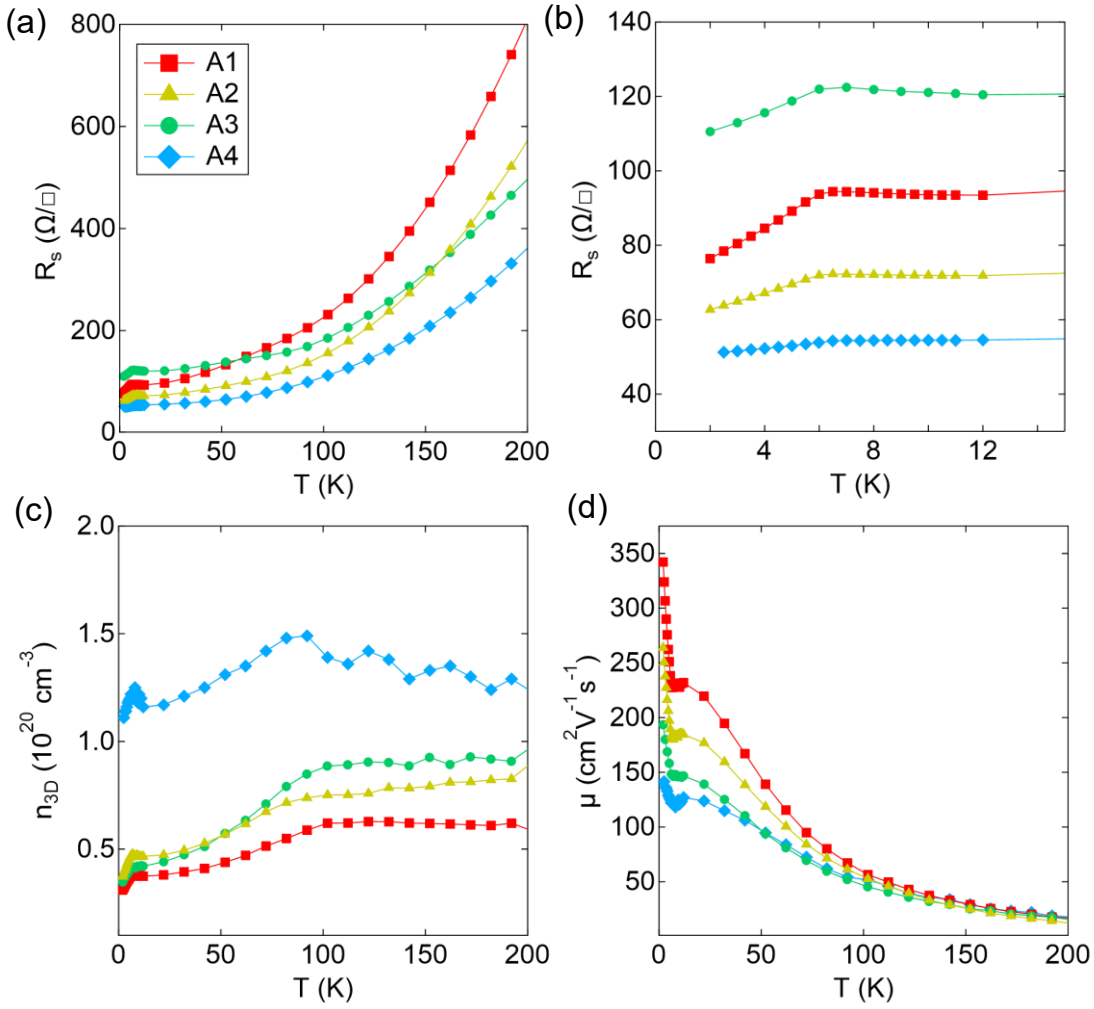

Figure 4.11 - Normal state transport measurements for Series A films. (a) sheet resistance R_S from 200 K to 2 K, (b) zoomed in R_s below 15 K, showing the kink at the Neél temperature T_N of the Sm:$EuTiO_3$ capping layer. (c) n_{3D} as a function of temperature and (d) mobility μ as a function of temperature. Adapted with permission from ref. [90].

followed by a downward kink reflects conduction in the Sm:$EuTiO_3$ layer as it goes through an antiferromagnetic transition [76,190], indicative of parallel conduction in both the Sm:$EuTiO_3$ and Sm:$Eu_xSr_{1-x}TiO_3$ layers. Figure 4.11(c) shows n_{3D} as a function of temperature. An abrupt downturn in $n_{3D}(T)$ starting around ~100 K is observed in all films, which has been attributed to the ferroelectric transition causing localization of some fraction of the mobile carriers needed to screen the polarization [31,46]. The Hall mobility μ at low temperatures roughly scales with n_{RT} as seen in Fig. 4.11(d), consistent with ionized impurity scattering. The normal state transport behavior exhibited by the films mimics that of comparable heterostructures with 0% Eu [189], indicating that the presence of 9% Eu has minimal effects on the normal state transport properties.

Figure 4.12(a) shows R/R_n for the Series A samples A1, A2, and A3. The measurement for sample A4 is shown separately in Fig. 4.12(b**)**. The extracted T_c values as a function of n_{RT} are shown in Fig. 4.12(c**),** along with values from Sm:$EuTiO_3$-capped Sm:$SrTiO_3$ films of comparable thickness from Ref. [169]. The T_c steadily increases with n_{RT} to a maximum of

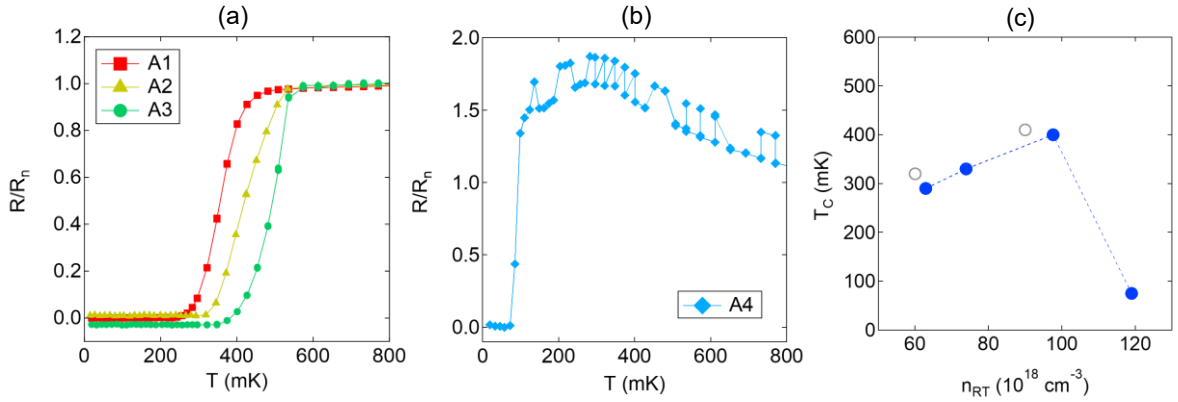

Figure 4.12 - Normalized resistance R/R_n as a function of temperature for (a) samples A1-3 and (b) sample A4. The alternating high and low values of R in the normal state are due to artifacts from the lock-in amplifier, and the slight upturn in R before the superconducting transition is occasionally observed in films with non-enhanced T_c. (c) T_c versus n_{RT} for series A films, along with values from comparable Sm:$EuTiO_3$–capped Sm:$SrTiO_3$ films grown on LSAT from ref. [189]. Adapted with permission from ref [90].

400 mK in the optimally doped sample with n_{RT} = 9.8 × 10^{19} cm^{-3} (A3), followed by a sharp drop-off of T_c at higher doping densities. The superconducting dome of these 9% Eu samples is similar to that of the superconducting domes exhibited by strained $SrTiO_3$ in the high-doping regime [31] in that the peak occurs at similar n_{RT} values and a sharp drop-off in T_c is observed on the overdoped side. The T_c's are also essentially unsuppressed when comparing to strained $SrTiO_3$ films [grey circles in Fig. 4.12(c)] [169]. We note again that thinner films capped with Sm:$EuTiO_3$ have generally lower T_c's than thicker films (see refs. [31,189]), but all T_c's are enhanced compared to unstrained Sm:$SrTiO_3$ films [31]. R/R_n as a function of magnetic field for the Series A samples are shown in Fig. 4.13, and the extracted H_{c2} values are given in Table 4.2 along with values of other previously reported strained $Eu_xSr_{1-x}TiO_3$ films for

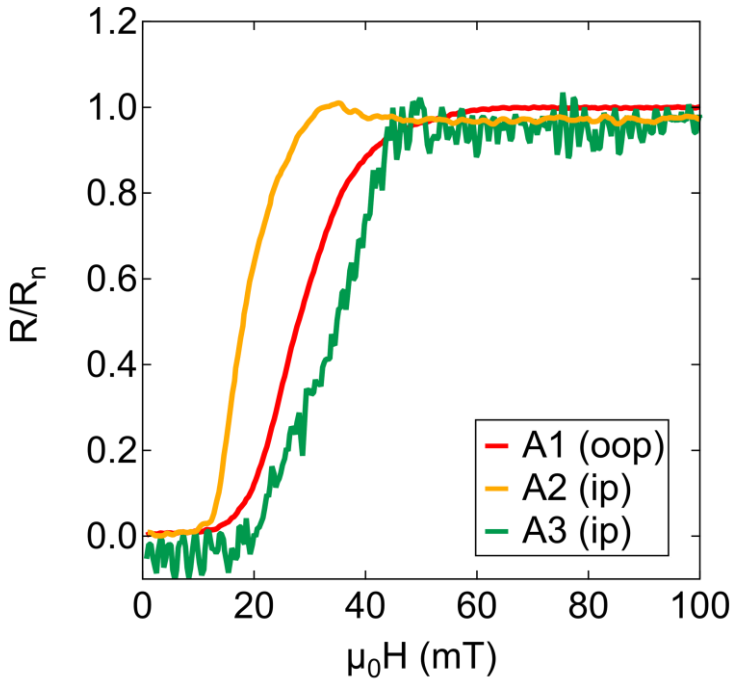

Figure 4.13 - Critical field measurements for films A1-3, measured at 20 mK. Measurements were taken by first ramping the field to 0.1T and then slowly ramping down. Adapted with permission from ref. [90].

Table 4.2 - Properties of strained Sm^{3+}-doped $Eu_xSr_{1-x}TiO_3$ films and heterostructures. Samples marked with a * were capped with ~10 nm Sm: $EuTiO_3$. The thin capped samples are from ref. [189] and the thick uncapped Eu-alloyed samples are from ref. [130]. Adapted with permission from ref. [90].

Thickness (nm)	n_{RT} (cm^{-3})	x (%Eu)	ip H_{c2} (T)	oop H_{c2} (T)	T_c (mK)	Ref.
70*	9×10^{19}	0	1.2	0.77	410	[189]
40*	6×10^{19}	0	2.7	1.0	320	[189]
170	8×10^{19}	0.5	1.4	1.0	600	[130]
167	7×10^{19}	2	1.0	0.6	550	[130]
187	5×10^{19}	3	0.6	0.4	500	[130]
68*	**6.3×10^{19}**	**9**	**-**	**0.028**	**290**	this work (**A1**)
92*	**7.4×10^{19}**	**9**	**0.018**	**-**	**330**	this work (**A2**)
75*	**9.8×10^{19}**	**9**	**0.035**	**-**	**400**	this work (**A3**)

comparison [130,169]. As can be seen from Table 4.2, the H_{c2} values for these 9% Eu films are strongly suppressed, even compared to the films with (nominally) 3% Eu [130]. Though H_{c2} measurements for both in-plane (ip) and out-of-plane (oop) field orientations could not be collected for all samples, the similarity in the oop and ip H_{c2} values suggest that the normally-observed anisotropy of H_{c2} in parallel and perpendicular fields for thin film $SrTiO_3$ has been suppressed.

4.3.3 Results: Series B

Normal state transport measurements for Series B are shown in Fig. 4.14. All films were nearly optimally doped with n_{RT} estimated to be 9.8×10^{19} cm^{-3}, 8.3×10^{19} cm^{-3}, and 8.2×10^{19} cm^{-3} for samples B1, B2, and B3, respectively (sample B1 is the same as sample A3 from

Series A). Figures 4.14(a,b) show $R_s(T)$, which again is qualitatively similar to that of Sm:$EuTiO_3$-capped Sm:$SrTiO_3$ films with 0% Eu. The lack of any additional anomalies in $R_s(T)$ would suggest that up to x = 0.30 Eu, no spontaneous magnetic ordering occurs. This has also been confirmed by SQUID magnetometry measurements [90]. As can be seen from Fig. 4.14(c) increasing the Eu content also has negligible effect on the low-temperature Hall mobility, as the curves essentially fall on top of each other. Figure 4.14(d) shows n_{3D} as a

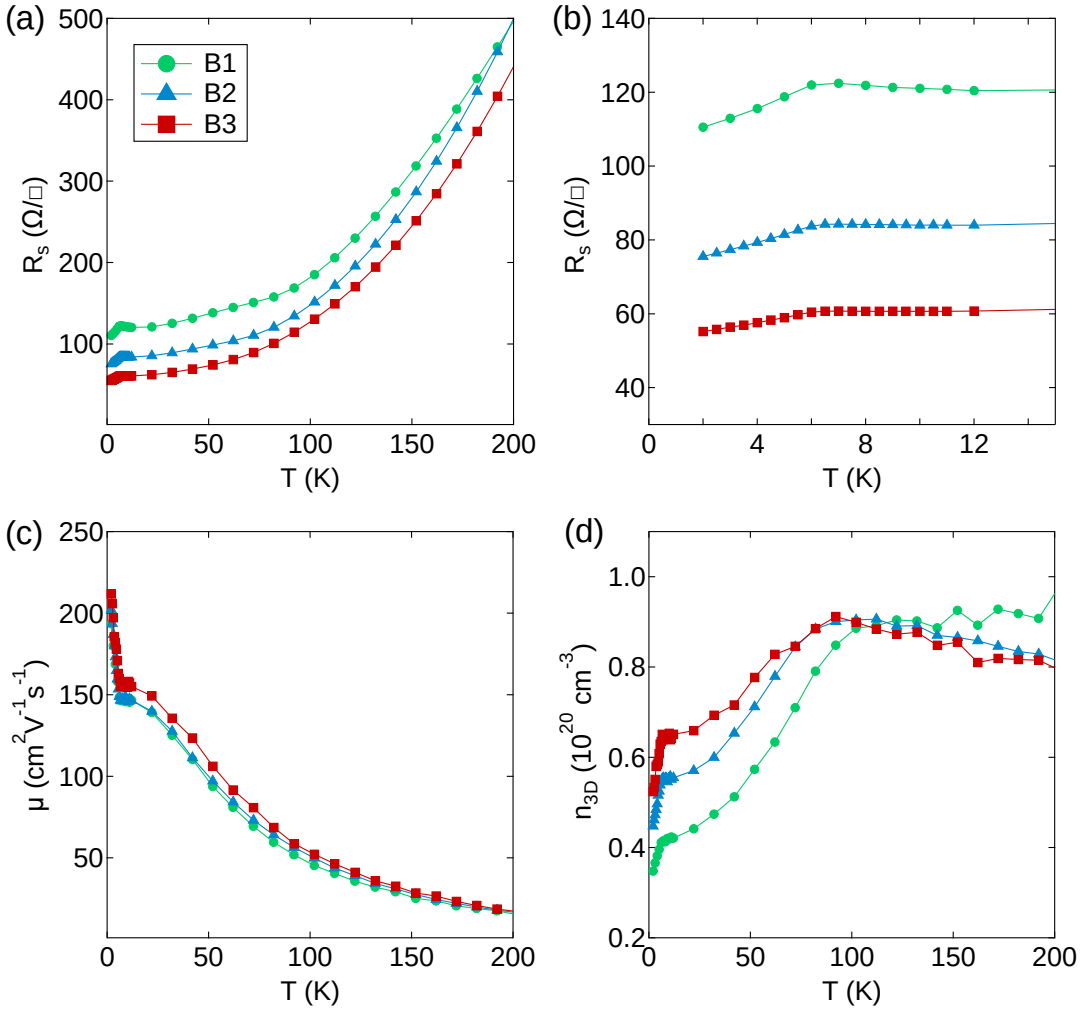

Figure 4.14 - Normal state transport properties as a function of temperature for series B. (a) R_s from 200 K to 2K, (b) zoomed-in R_s from 15 K to 2 K, (c) mobility and (d) n_{3D}. Adapted with permission from ref. [90].

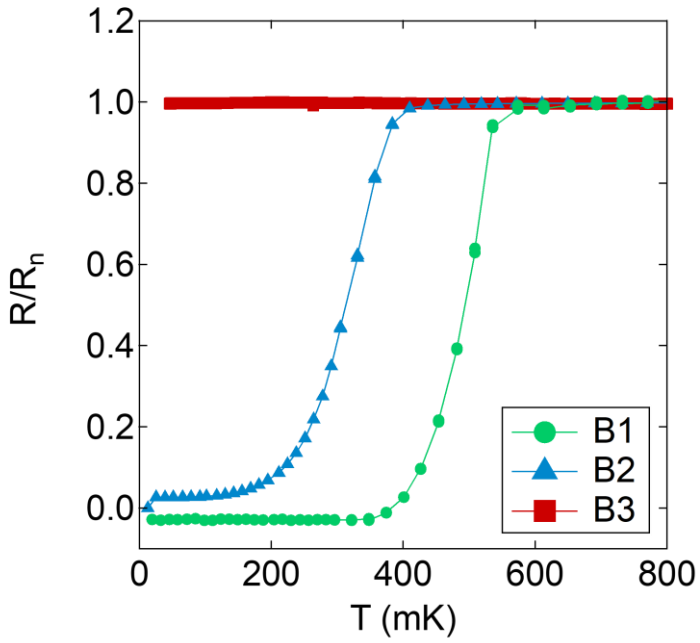

Figure 4.15 - Superconducting transitions measurements for Series B films. Measurements were taken on heating from base temperature. The small offsets of the resistance from zero are measurement artifacts. Adapted with permission from ref. [90].

Table 4.3 - Summary of properties for Series B samples. The average Eu-Eu distance $l_{Eu\text{-}Eu}$ was calculated using the Eu concentration x as measured by XPS. Adapted with permission from ref. [90].

Sample	BEP x	XPS x	n_{RT} (cm^{-3})	$Eu_xSr_{1-x}TiO_3$ Film Thickness (nm)	T_c (mK)	$l_{Eu\text{-}Eu}$ (Å)
B1	0.05	0.09	9.8×10^{19}	75	400	8.7
B2	0.10	0.14	8.3×10^{19}	83	180	7.5
B3	0.20	0.30	8.2×10^{19}	92	0	5.8

function of temperature for Series B. All films possess similar n_{3D} at elevated temperatures and exhibit carrier depletion beginning around ~100 K. As the Eu content increases, the degree of carrier depletion decreases, explaining the different R_s values in Fig. 4.14(b). The superconducting transitions for Series B films are shown in Fig. 4.15. The T_c of sample B1 (A3) is 400 mK, comparable to that of Sm:$EuTiO_3$-capped Sm:$SrTiO_3$ films with 0% Eu, while

that of sample B2 is suppressed to ~180 mK, and sample B3 does not exhibit a superconducting transition. A summary of Series B film properties is given in Table 4.3.

Figure 4.16(a) shows the SHG intensity measurements scaled by film thickness for the Series B films, along with a measurement of a comparable sample structure with 0% Eu shown for comparison (sample A in refs. [169,189]). A sharp upturn in the SHG signal is clearly seen in the 0% Eu sample, whereas the transition is less pronounced the Eu-alloyed films, although remanences of it still exist. As mentioned above, sharp SHG transitions can be broadened by even a small degree of strain relaxation [157], however, as can be seen from the XRD data shown in Fig. 4.16(b), here, all films are fully strained and stoichiometric. Thus, the presence of Eu in concentrations of $x \geq 0.09$ apparently suppresses sharp SHG upturns associated with a global ferroelectric transition. This persistent finite signal at low temperatures can be attributed to the presence of polar nanodomains [157,168]. The change in the films'

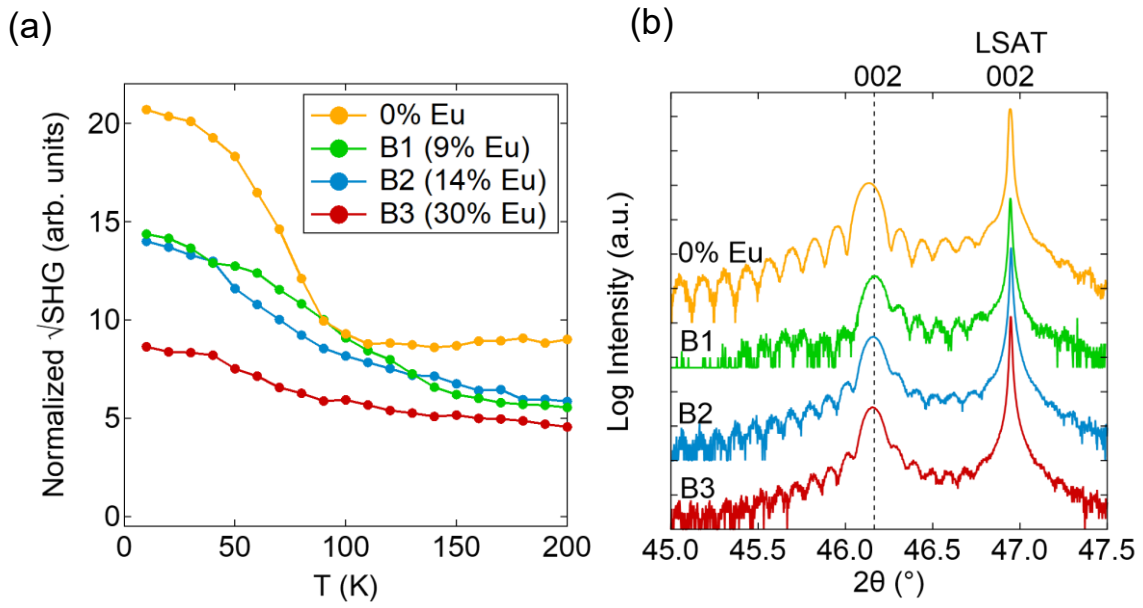

Figure 4.16 - (a) SHG signal normalized to film thickness as a function of temperature for Series B, alongside a comparable Sm:$EuTiO_3$/Sm:$SrTiO_3$/LSAT heterostructure, which displays the signatures of a global ferroelectric transition (sample A from ref. [189]). (b) On-axis XRD scans for the Series B, along with scan of the 0% Eu sample in (a). Adapted with permission from ref. [90].

ferroelectric ordering behavior is also indicated by scanning transmission electron microscopy studies (Fig. 4.17), which show no polar nanodomains at room temperature for the $x = 0.09$, at least within the detection limits of the method, in contrast to a $x = 0$ film which shows moderate Ti displacements that are correlated.

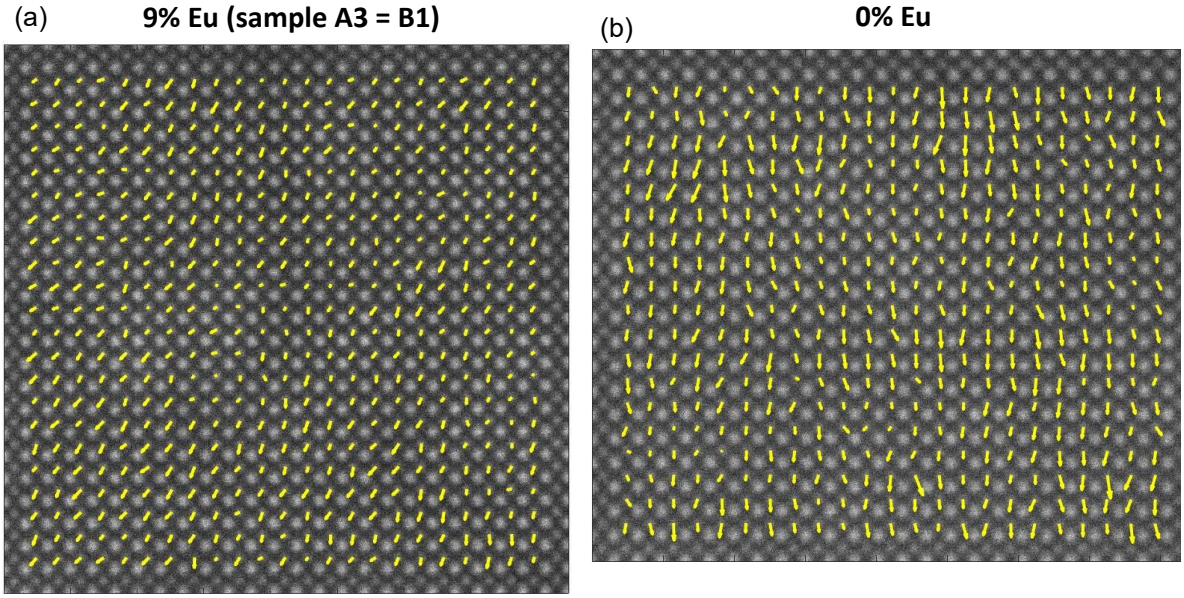

Figure 4.17 - HAADF-STEM images taken at room temperature of sample (a) A3 and (b) comparable $EuTiO_3/SrTiO_3$ sample (sample A from refs. [168, 186]. The overlaid arrows represent the off-centering displacement vector of the Ti columns, and their magnitudes have been magnified 8 times. Adapted with permission from ref. [90].

4.3.4 Discussion: Ferroelectric Transition

As mentioned in the introduction, the ferroelectric transition in strained $SrTiO_3$ has both displacive (soft-mode) and order-disorder characteristics, the latter being evidenced by the presence of nanodomains above the transition, which are an essential precursor to the ferroelectric transition. The SHG in Fig. 4.16(a) would indicate that the addition of $x \geq 0.09$ Eu has led to a crossover upon which a long-range ordered state cannot be established, although the steadily increasing SHG signal with decreasing temperature of the moderate-Eu films

indicates that the degree of polarization is still increasing. It is reasonable to assume that Eu produces minimal crystalline disorder in $SrTiO_3$ due to its almost identical ionic radius to Sr, which is supported by the similar crystallinity exhibited by all films in XRD [Fig. 7(b)] and the relatively unchanging normal state transport properties across series B (Fig. 4.14). Although both $SrTiO_3$ and $EuTiO_3$ are considered incipient ferroelectrics due to a soft mode instability, $SrTiO_3$ is much closer to its quantum critical point. Studies of $Eu_xSr_{1-x}TiO_3$ solid solutions have found that the dielectric constant (ϵ') becomes strongly reduced in going from $x = 0$ to $x = 0.2$, and the $\epsilon'(T)$ behavior changes from that of $SrTiO_3$, which has a saturating $\epsilon'(T)$ as T approaches 0 K, to relaxor-type behavior with a very broad $\epsilon'(T)$ peak around ~30 K [167]. The $0 \leq x \leq 0.25$ range has correspondingly exhibited a strong increase in the frequency of the soft transverse optical phonon mode [191]. This supports the idea that the addition of Eu to the $SrTiO_3$ host lattice decreases the polarizability and leads to a crossover from a uniform polar ferroelectric ground state to a state with only locally dipolar regions. A similar SHG signal is seen in PLD-grown, strained $SrTiO_3$ films, which exhibits relaxor-like behavior [168](Fig. 4.5) , thus implying the presence of locally polar regions.

4.3.5 Discussion: Superconducting properties

It is rather remarkable that replacing 9% of non-magnetic Sr^{2+} with magnetic Eu^{2+} results in virtually no suppression of T_c [Fig. 4.12(c)] and that superconductivity survives up to at least 14%. In an s-wave superconductor, AG theory states that the introduction of magnetic impurities should cause an immediate and continuous suppression of T_c as a function of impurity concentration [174] with typical critical concentrations being on the order of ~ 1

at.% [192]. While the addition of magnetic Eu^{2+} does eventually suppress the T_c, there is an initial regime in which it has virtually no effect. In fact, the situation is more analogous to Anderson's theorem for the effect of *non*magnetic impurities on s-wave superconductors, in which the impurities impose virtually no suppression of T_c up to a certain critical concentration, above which the impurities begin to have larger effects than simply increasing scattering rates [193]. It should be noted, however, that the AG theory tends to hold most strongly for binary and pseudobinary systems. For ternary systems, it has been suggested that the existence of distinct crystallographic sites allows for spatial separation between the conduction electrons and the magnetic sublattice, which could reduce the effect of the exchange interaction [192]. Another possible source of resistance to the effect of magnetic impurities is Kondo screening. However, Kondo screening is typically manifested by an upturn in resistivity, which we do not see between 2 K and 300 K.

Unlike T_c, the magnetic response of the superconducting $x = 0.09$ film does display markedly different behavior from that of doped, strained $SrTiO_3$ or even $Eu_xSr_{1-x}TiO_3$ with $x \leq 0.03$. As seen in Table 4.2, though the T_c values at $x = 0.09$ are relatively unsuppressed, the H_{c2} values are suppressed by an order of magnitude (or more) and values are similar to those of bulk $SrTiO_3$ [194,195]. This suggests a crossover into a different type of superconducting regime associated with the Eu alloying. Interestingly, the suppression of H_{c2} by moderate Eu alloying correlates with the suppression of a global ferroelectric transition. Notably, fully strained films with $x \leq 0.03$ exhibit the signatures of a global ferroelectric transition in SHG along with large H_{c2} values [130]. One possible explanation for enhanced H_{c2}'s at low x is that when ASOC is present due to inversion symmetry breaking, spins are pinned and there will be an additional energy cost for pair-breaking for certain magnetic field orientations [140]. As

the long-range ordered ferroelectric state is lost, any enhancement of H_{c2} by ASOC would then diminish. At this point, however, this suggestion is purely speculative. We also note that both ip and oop H_{c2}'s are reduced in magnitude while the effect of ASOC on H_{c2} should be strongly directional.

4.3.6 Conclusions

We have shown that films of Sm-doped $Eu_xSr_{1-x}TiO_3$ remain superconducting up to Eu concentrations of at least $x = 0.14$. The crossover from formation of a long-range ferroelectric state induced by strain to one that contains only locally polar order is supported by the suppression of a strong upturn in SHG intensity. The strongly suppressed H_{c2}'s in this regime suggests that the long-range polar phase may provide protection from magnetic depairing, which is lost when the polar domains become randomly oriented, adding to the growing evidence that polar order influences the superconductivity of $SrTiO_3$. The eventual total suppression of superconductivity between $0.14 < x < 0.30$ may also be connected to the suppression of polar order, but at this point we can only speculate. The results show, however, that suppressing ferroelectricity, i.e., driving the films closer to a putative quantum critical point, in this case via Eu alloying, does not promote superconductivity, contrary to the suggestions of some of the theoretical proposals. There are very few theories that directly connect superconductivity to spin-orbit coupling [196,197] although there are recent suggestions of a more indirect link via a modification of the phonon coupling [56]. It is hopeful that the results motivate further theoretical studies in the role of static polar order in the superconductivity of $SrTiO_3$.

Chapter 5. Summary and future directions

5.1 $BaSnO_3$

5.1.1 $BaTiO_3$/$BaSnO_3$ heterostructures

Attempts to reduce interfacial traps in heterostructures of high-k (ferroelectric) $BaTiO_3$ on La-doped $BaSnO_3$ channels were carried out by growing both layers in the same growth chamber without breaking vacuum between the growth of the layers. Secondary phases were observed to have formed which were not exhibited in calibration samples of either $BaSnO_3$ or $BaTiO3_3$, indicating they are likely formed by an interfacial reaction between the $BaSnO_3$ and $BaTiO_3$. A possible cause could be remnant Sn droplets on the surface of the $BaSnO_3$, though this is purely speculation. Some of these phases could be suppressed by post-growth annealing.

All samples suffered from carrier depletion due to the $BaTiO_3$ capping layer, as would be somewhat expected due to the ferroelectric polarization of $BaTiO_3$. The reduced carrier density lead to a strong reduction in mobility or insulating behavior due to the reduced screening effect. It is unlikely that the interfacial defects were the main cause for the lower mobility as interfacial and surface scattering has been shown to be relatively negligible in $BaSnO_3$ films (at least above thicknesses of ~20nm). Mobility may have been relatively less affected by the depletion

had a higher carrier density in the channel been used. However, for depletion mode MOSFET's, high channel densities will not allow for complete pinch-off.

5.1.2 Lattice-matched growths

The very limited lattice-matched growths presented here resulted in differing behavior, though both grew fully coherent films with no relaxation-induced dislocations. The growth on $SrZrO_3$ substrates resulted in a noticeable improvement of the mobility relative to calibration samples, though the mobility of 130 $cm^2\ V^{-1}\ s^{-1}$ is far below that maximum mobility that has been achieved in other films. It is likely that the use of the smaller (and less-optimized) substrate limited the growth quality due poor thermal coupling during growth. This highlights the fact that mobilities in $BaSnO_3$ films are equally as sensitive to defects produced by poorly-controlled growth conditions as to the presence of relaxation-induced dislocations. The growth on a $BaSnO_3$ substrate, on the other hand, resulted in a severely reduced mobility relative to calibration samples. This in part could be attributed to the poor surface quality of the substrate. However, the vastly different growth rate of the sample also points to the possibility that the growth conditions were shifted for this growth, likely due to the irregular shape of the $BaSnO_3$ crystal. Again, these results seem to indicate that the reduction of threading dislocations is of minor importance when poorly-controlled growth conditions produce a high degree of nonstoichiometric defects.

5.1.3 Stoichiometry in MBE-grown $BaSnO_3$ films

It was demonstrated that La-doped $BaSnO_3$ films with moderately high mobility could be grown using only SnO_2, Ba, and La effusion sources. The use of an additional oxidant (molecular oxygen or RF-plasma) shifted the growth conditions to lower SnO_2/Ba flux rations and only marginally improved mobility. This implies that a significant amount of the oxygen incorporated into the film comes from SnO regardless of the use of the additional oxidant, which also leads to extremely Sn-rich conditions. The excess Sn can be incorporated on the A-site as Sn_{Ba} antisite defects, and indeed formation of these defects may even be somewhat preferred due to the ability for Sn to remain in the Sn^{2+} charge state, which it favors in reducing (UHV) environments, over Sn^{4+}, which is needed for Sn to sit on the B-site. The presence of Sn_{Ba} defects was elucidated by the strongly reduced lattice parameters due to the smaller ionic radius of Sn^{2+} sitting in the much larger Ba^{2+} site. Interestingly, the region where the highest concentration of Sn_{Ba} is expected (i.e. where the lattice parameter is most reduced) also coincides with the highest mobility films. The poor electrical properties of films with 'stoichiometric' lattice parameters is explained as being due to a higher concentration of expanding defects such as Ba vacancies, which compete with the Sn_{Ba} and average out to what appears to be a 'stoichiometric' lattice parameter. As Sn_{Ba} are charge neutral defects, they would be expected to have less of a detrimental effect on mobility than charged defects such as vacancies.

Thus, these results indicate that Sn_{Ba} may pose an upper limit to the mobility of MBE-grown films, as all indications are that they exist regardless of how much additional oxidant is supplied, ozone included (Fig. 5.1). The dual valence of Sn, which prefers the Sn^{2+} state in the

UHV environment of MBE, must be overcome by providing strongly oxidizing conditions, which may be difficult to achieve in UHV MBE.

5.1.4 Future directions

The successful utililization of a metal-organic precursor which contains Sn^{4+} bonded to oxygen, such as SnTB, would be a very likely route to achieving fully oxidized $BaSnO_3$ films. Other MO sources for Sn have been used, but they are unable to produce mobility on-par with what can be achieved with SnO_2 sources (Fig. 5.1). This could be in part due to the MO used, which contains no oxygen. SnTB was found to be difficult to reliably deliver to the growth substrate without degrading, and so improvement of the delivery of SnTB would be necessary. The development of a different molecule that has the desired Sn^{4+} bonded to oxygen which possesses more desirable thermal properties could also be a route forward.

Realistically, however, the most important obstacle for the further development of $BaSnO_3$ for possible device usage will be the development of a lattice-matched substrate that can be easily and commercially produced. The presence of threading dislocation not only poses an ultimate limit to mobility of bare films, but also degrades the properties of epitaxial heterostructures for possible high power-density FETs. For epitaxial high-k barrier layers, the misfit dislocations likely penetrate through the barrier layer and serve as a leakage path. The dislocations also serve as a severe source of scattering and necessitate a relatively high carrier density in a channel to maintain high mobility. However, this high channel density needed to maintain mobility may be higher than can be reliably pinched off in FET devices. Thus,

reducing dislocations may allow for more overlap between the carrier density regions which allow for high mobility and those which can be effectively gated.

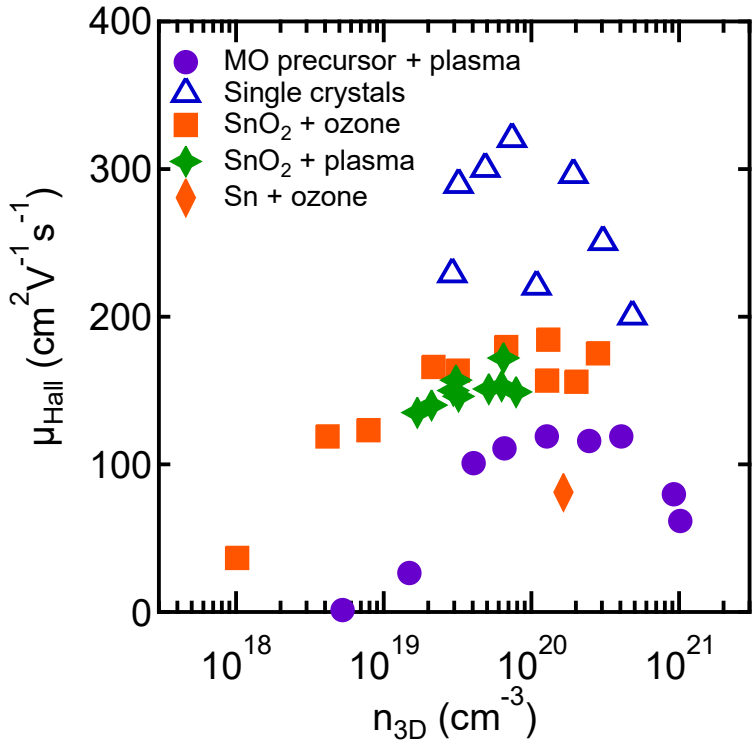

Figure 5.1 - Comparison of maximal mobilities achieved for MBE-grown $BaSnO_3$ films using various Sn and oxidant sources, compared to single crystals. Data adapted from refs [6,78,80,84,198].

5.2 Sr_3SnO

5.2.1 Summary: Sr_3SnO growth

It was demonstrated that the using SnO_2 and Sr sources, Sr_3SnO could be grown via MBE. Though this had been achieve by other groups as well [121], it was shown by cross-section SEM that multiple phases can easily coexist in the films, which cannot be identified with XRD

alone. Furthermore, this weakened the idea that a true adsorption-controlled growth window could be achieved using this growth method. It was also demonstrated that depositing an insulated ZrO_2 protective capping layer using a metal-organic ZTB source in the same growth chamber could effectively protect the air-sensitive Sr_3SnO films from degradation such that *ex situ* structural measurements could be performed.

5.2.2 Continued work: phase pure growth conditions and electrical measurements

Continuation of the Sr_3SnO work was carried out by Wangzhou Wu, who was able to identify growth conditions which achieved single-phase Sr_3SnO as told by SEM cross-sections [87]. Wu was also able to electrically characterize the films by removing the samples from the chamber load lock directly into glovebag filled with inert N_2. The sample would then be assembled onto a measurement puck in the inert atmosphere, and then quickly delivered to the physical property measurement system (PPMS) while still in the glovebag. Controllable doping was also demonstrated by using In^{5-} instead of Sr vacancies, which avoided the issue of introducing secondary phases by changing the Sr/SnO_2 flux ratio [88]. The same order of magnitude of carrier density reported to produce superconductivity in the polycrystalline samples [22] was achieved using this method in films, but no superconductivity was observed [88].

5.2.3 Future Directions: Improvement of the capping layer

Though the indications so far make it unlikely that Sr_3SnO is an intrinsic topological superconductor, a topological Dirac oxide is an interesting material system to explore in itself. This, however, would require a much more robust method for electrical measurement and device fabrication than the very energy intensive glovebag technique.

Though the ZrO_2 capping layer was found to be adequate to allow for structural measurements, early attempts at device fabrication through the ZrO_2 failed. The proposed method for contacting the protected Sr_3SnO layer through the cap was quite simple: using a combined ion mill and sputter system available in the UCSB Nanofab, the areas of the sample intended for contact deposition would first be etched down by the ion mill to expose the Sr_3SnO. Then, without breaking vacuum, metallic contact layers would be sputtered, which would cover up the now-exposed Sr_3SnO areas and thus protect them once removed from the vacuum. The details of lithography for such a method may take some development but the idea itself was very straightforward. Unfortunately, it was found that samples would degrade during the processing. For the sample processing, the samples spent a significantly larger amount of time in ambient air than normal, as well as being placed in numerous liquid baths during the lithographic process. Thus, it seems likely that the ZrO_2 was not as fully protective as originally believed. Porosity in MO-grown ZrO_2 is a documented issue [123] (Fig. 3.4b), in part due to the narrow temperature window that produces both ample growth rates and fully-dense films. Small deviations from this window can introduce porosity. Further calibration of the growth conditions needed for achieving fully dense ZrO_2 could thus be beneficial, though the degree of control necessary might not be possible as the substrate heater in the MBE system is not well-controlled at such low temperatures. The degradation issue may have been caused most

directly by incomplete coverage of the ZrO_2, possibly leaving Sr_3SnO on the edges unprotected which would oxidize, and this oxidation could then spread throughout the film. The effect of the narrow temperature window for fully dense growth could be exacerbated at the edges of the sample, where a temperature gradient likely exists. As it was found that a relatively thick film (> ~100nm) is required to protect at least the interior areas of the film from fast oxidation, the inability to grow such a thick and dense film on the edges may ultimately limit ZrO_2 grown using ZTB from serving as a robust protective layer. Deposition methods which are more physical in nature than chemical – such as sputtering – may be better suited to achieve full edge coverage if such a capability was available without the need to break vacuum, though there could be other difficulties encountered.

5.3 $SrTiO_3$

5.3.1 Summary: ferroelectricity and superconductivity in $Eu_xSr_{1-x}TiO_3$ films

Superconductivity in Sm-doped $Eu_xSr_{1-x}TiO_3$ films survives up to $x = 0.14$, despite the high concentrations of magnetic Eu^{2+} which would be expected to destroy the superconductivity in a conventional *s*-wave superconductor. The eventual suppression of superconductivity can more likely be attributed to the crossover from a globally ferroelectric state to a locally polar state due to the reduction of the polarizability of the lattice introduced by Eu alloying. Though superconducting T_c is not suppressed at $x = 0.09$, the loss of a global ferroelectric state is observed, and severely reduced H_{c2} values are measured as well. This may indicate that, though the length scale of the locally polar regions may be sufficient for maintaining the enhanced

T_c's, the influence of Rashba-like ASOC is suppressed by the reduction in 'average' broken inversion symmetry across the crystal, thus limiting the resistance to magnetic depairing from the applied field.

These results cast doubt on the theoretical proposals which would indicate that driving the films closer to a putative ferroelectric QCP promotes the superconductivity, as we see instead see suppression. These results also provide yet another piece of evidence that *static* broken inversion symmetry may be a key component of superconductivity in $SrTiO_3$, and that this broken inversion symmetry need not be global if locally polar domains of some critical size (relative to the Cooper pair spacing) is maintained.

5.3.2 Future Directions

In the context of Eu-alloyed $SrTiO_3$ films, more in-depth measurements of the behavior of H_{c2} with x under various orientations would have been desirable, had the $EuTiO_3$ capping layers not experienced degradation. Mapping the H_{c2} as a function of T can also provide useful information about the superconducting state.

More broadly, it would be extremely interesting to investigate the behavior of polar nanodomains as a function of temperature using high resolution STEM. Some attempts have been performed [124], but the mechanical noise introduced by cooling systems is not trivial to overcome, though it is possible to do and indeed is currently being pursued. The evolution of nanodomains as temperature is lowered, particularly in films which do not exhibit a global ferroelectric transition in SHG, would be very interesting to explore. Having information about the general length scale of the nanodomains at temperatures closer to the superconducting

transition may provide information as to how local polarity plays into the superconducting state.

Another area that was not explored in this thesis – but nonetheless remains somewhat unanswered – is the effect of the $EuTiO_3$ capping layer on the T_c's of films. So far, the only $EuTiO_3$-capped $SrTiO_3$ films measured for superconductivity have been thinner than ~100 nm. As shown in ref. [169], the depolarization field experienced by thin films can destroy ferroelectricity (and the superconductivity) below some critical thickness. However, upon approaching this critical thin-ness, it is likely that the depolarization fields may suppress the Ti displacements as well, which is somewhat supported by the limited STEM measurements performed on the thinner films. As mentioned, these thinner capped films exhibited enhanced T_c's but which were lower than the enhanced values measured in thicker, uncapped films. Thus, it would be interesting to grow thicker $SrTiO_3$ films, cap them with 10 nm of $EuTiO_3$ and measure the T_c's. If they are still suppressed relative to comparably thick, uncapped films, then this would indicate that the $EuTiO_3$ is in part responsible for the suppression. If not, then the reduced polarization of thinner films is responsible for the reducing the enhancement of the T_c, providing even more evidence for the importance of static polarization in $SrTiO_3$ superconductivity.

Ultimately, the link of broken inversion symmetry and superconductivity in $SrTiO_3$ is most exciting for the possibility of realizing a spin-triplet superconductor, and thus possible intrinsic topological superconductivity. To the knowledge of this author, the only direct evidence for such a state would be provided by the NMR Knight shift in the superconducting state. The requirement of refrigeration below 2K to access the superconductivity of $SrTiO_3$ presents an experimental difficulty for such a measurement.

Appendix A

SnO_2 cell clogging, cell damage, and pits in $BaSnO_3$ films

During the calibration growth stage of one of my early growth campaigns, it was found difficult to achieve μ higher than ~70 $cm^2\ V^{-1}\ s^{-1}$ regardless of how high SnO_2/Ba flux ratio was used (Fig. A.1). It was also found that the growth rate was not scaling with Ba flux as generally expected (not shown). Lowering the growth temperature allowed for higher μ to be accessed, up to ~ 120 $cm^2\ V^{-1}\ s^{-1}$ (Fig. A.1), and the growth rate then roughly scaled with Ba flux. This seemed to indicate that an excessive amount of Sn was being desorbed by the higher growth temperatures, though these growth temperatures had historically been able to produce higher mobilities without the problem of high Sn desorption. The maximum μ at the lower temperatures was also far below what could typically be achieved, and the flux ratios necessary to achieve the maximal mobilities at the time was also excessively high.

AFM measurements of the lower-temperature films are shown in Fig. A.2. In the films grown at SnO_2/Ba ratios above 40, pits can be seen to form, beginning as micropipe-like features in the sample grown at ratio 62, and getting larger in diameter as the flux ratio becomes more Sn-rich. The most likely cause was determined to be Sn droplets that had formed on the surface growing film, which etched away the underlying film. The largest pits in the highest ratio film were approximately 15 nm deep in a 40 nm thick film, indicating that they did not

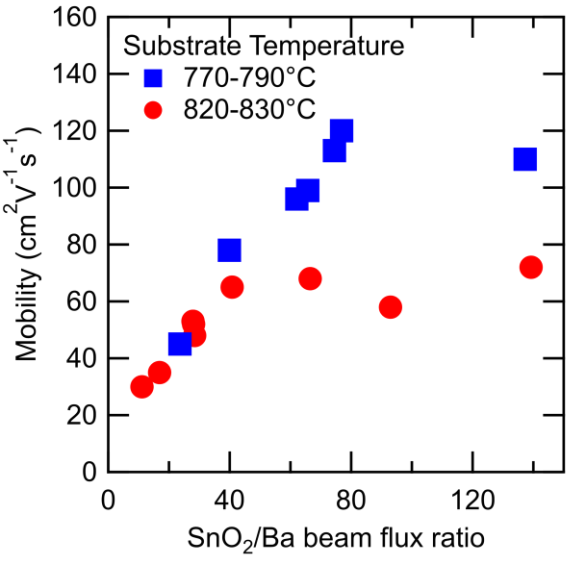

Figure A.1 - Mobilities of $BaSnO_3$ calibration growths as a function of SnO_2/Ba flux ratio grown at different substrate temperatures, grown using the clogged SnO_2 cell.

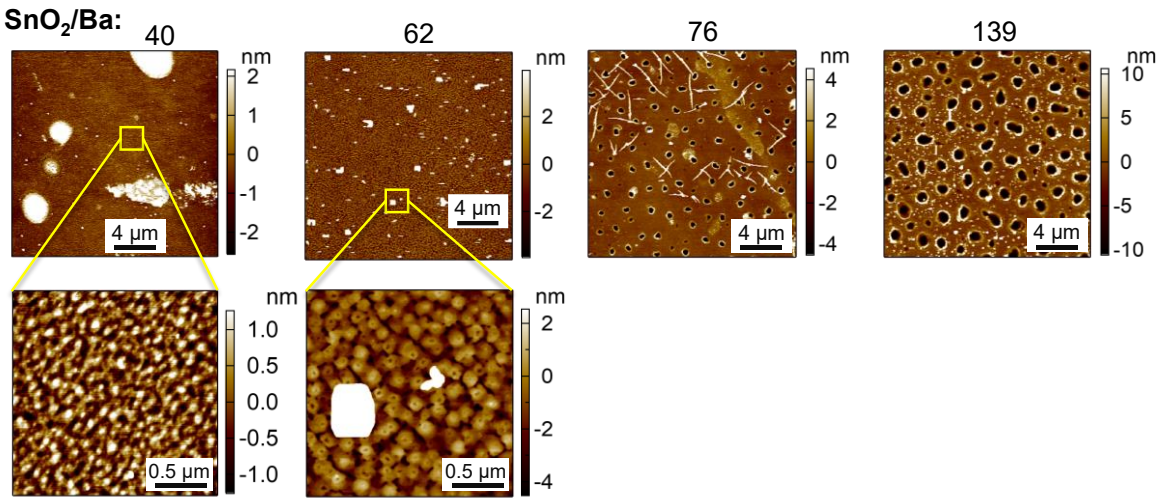

Figure A.2 - AFM images of $BaSnO_3$ film surfaces grown at lower substrate temperatures for various SnO_2/Ba flux ratios. Micropipe features can be seen to form in the film grown with a ratio of 62, and these grow into larger and larger surface pits with higher flux ratios.

extend down to the substrate. Thus, they likely formed over the course of the growth and become larger as growth proceeded. They may have even served as a source of Sn incorporation during growth, as desorbing them at higher temperatures was detrimental to the total growth rate as well as mobility. This ordeal highlighted an intriguing fact about $BaSnO_3$ film mobilities as well: in this mobility regime, the mobility was much more sensitive to the film stoichiometry than macroscopic defects like surface pits. In other words, the maximal mobility was set by the maximal Sn incorporation that could be achieved with the current growth and flux conditions. The maximal mobility was achieved at SnO_2/Ba of ~80, and as the flux ratio increased, little change in the mobility is seen as more Sn cannot be incorporated into the film, it simply forms droplets on the surface. The larger size of the pits (which would essentially function as a higher density of surface scattering centers for the mobile electrons) had essentially no effect on degrading the mobility of the films.

This unusual behavior of the growth conditions signaled that the composition of the SnO_2 flux had shifted, and inspection of the SnO_2 cell being used explained why. Shown in Fig. A.3(a), the mouth of the cell was severely clogged with a large SnO_2 deposit. Despite the use of a hot-lip crucible with a base-tip temperature gradient of 100 °C, it seemed that SnO_2 had preferentially deposited on the mouth of the cell, likely during the idle periods of the cell when the shutter was closed. This was a likely explanation for the drastically different flux composition that produced the Sn droplets in the films, and also why a significantly higher SnO_2 BEP was needed. Flux BEP measurements only measure the total pressure of all species coming from the cell, it cannot give information about the relative composition. Switching to another SnO_2 cell that was not clogged (for reference, one that looks like Fig. **A.3(b)**) allowed for the growth of higher μ films using lower flux ratios.

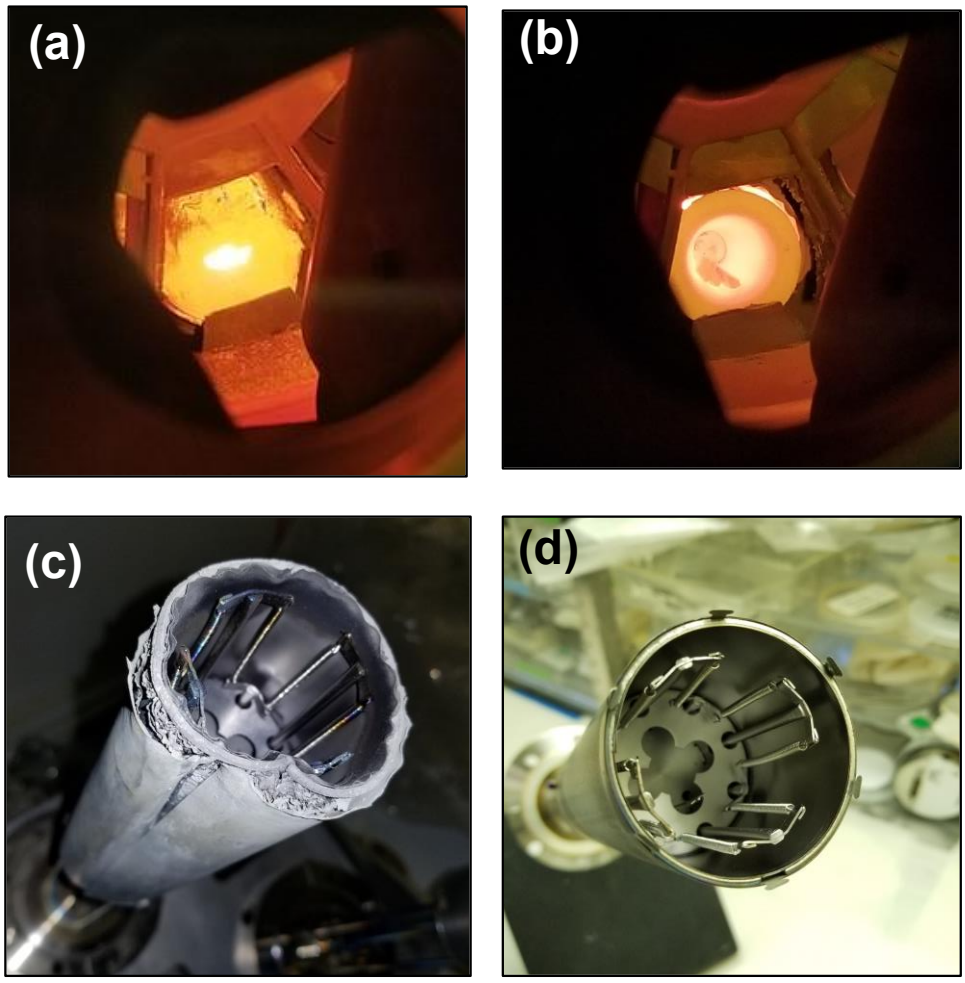

Figure A.3 - Photographs of (a) the mouth of a clogged SnO_2 effusion cell in operation at high temperatures, (b) mouth of a normal (non-clogged) effusion cell in operation at high temperatures, (c) effusion cell unloaded from the MBE chamber with crucible removed, showing the damaged heat shielding from contact with SnO_2 at high temperatures, and (d) undamaged effusion cell unloaded from the MBE chamber with crucible removed, for comparison.

The reason as to why this severe buildup occurred was determined to be that the cell idle temperature had simply been too high. Idling at too high a temperature would cause persistent sublimation of the source, which would then buildup on the slightly cooler outer regions of the cell, including the shutter and surrounding recesses of the cell port. The hot-lip temperature gradient of 100 °C was apparently not sufficient to prevent this. Typical temperatures of the SnO_2 (base) that produced growth-level fluxes were in the 1100 – 1200 °C range. An alumina

crucible must be used for SnO_2 due to the propensity for reaction with metal crucibles, and PBN was also not deemed a viable option. Ceramic crucibles are more subject to cracking under thermal stress, and thus slower ramp rates must be used compared to metal and PBN crucibles. For SnO_2, a ramp rate of 2 °C/minute was found to avoid cracking. This naturally resulted in extremely long heat-up times to the growth temperature if the idle temperature was low, and thus a high idle temperature of 900 °C was utilized. However, after the discovery of the clogged cell, the SnO_2 idle temperature was lowered to 700 °C. The now-longer heat-up times were mitigated by programming the SnO_2 cell to automatically begin warming up early in the morning on a growth day, such that it was at ~ 900 °C by the time the grower begun setting up for the growth.

A further discovery from the severely clogged SnO_2 cell was how damaging SnO_2 could be to the Mo and Ta metal components of the cell at the elevated temperatures. A photo of one of the SnO_2 cells after being removed from the chamber is shown in Fig. A.3(c). A significant amount of degradation is seen, which is not expected as these cells are designed to be able to withstand the high temperatures used. Thus, it was determined that SnO_2 is highly reactive with metals (at least Mo and Ta) at such high temperatures, and direct contact SnO_2 buildup with the outer metallic part of the cell should be avoided as much as possible. This problem was relayed to engineers at E-Science Inc., who developed an alumina crucible with an extended lip that covered the top outer portions of the Mo heat shielding of the cell (Fig. A.4). After utilizing the overflow lip crucible and also using a lower idle temperature for the SnO_2 cell, cell clogging was no longer observed and cell damage was minimized. In general terms, before using the new crucibles and the lower idle temperatures, the effusion cells used for SnO_2 were found to be in need of some degree of repair after almost every single growth campaign.

After the buildup mitigation strategies were put in place, SnO_2 cells could be re-used without maintenance after every growth campaign.

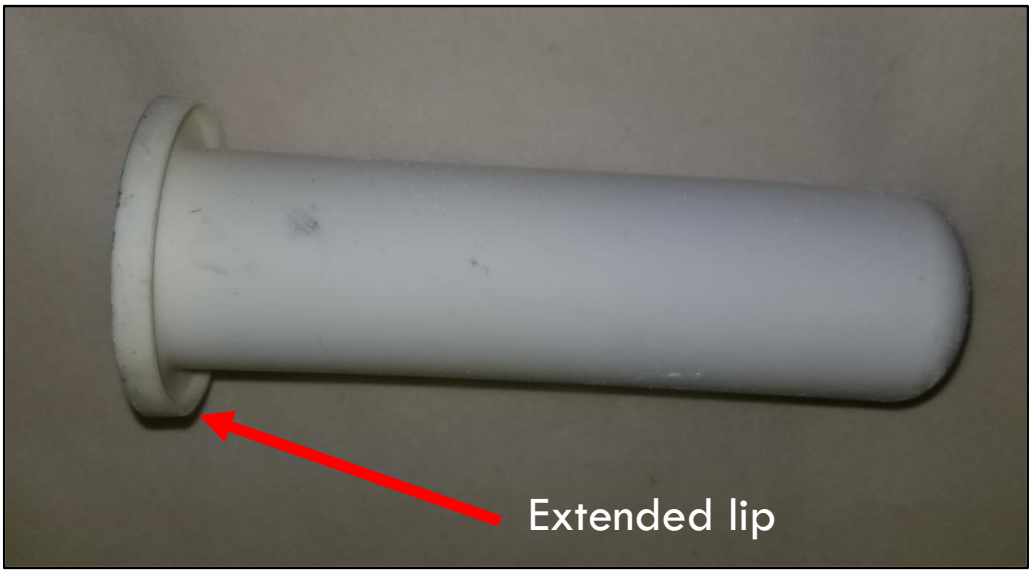

Figure A.4 - Photograph of a 120cc alumina crucible with extended lip used for SnO_2 source material to prevent damage to the effusion cell heat shielding.

References

[1] A. J. Smith and A. J. E. Welch, *Some Mixed Metal Oxides of Perovskite Structure*, Acta Crystallogr. **13**, 653 (1960).

[2] H. Mizoguchi, H. W. Eng, and P. M. Woodward, *Probing the Electronic Structures of Ternary Perovskite and Pyrochlore Oxides Containing Sn4+ or Sb5+*, Inorg. Chem. **43**, 1667 (2004).

[3] T. Schumann, S. Raghavan, K. Ahadi, H. Kim, and S. Stemmer, *Structure and Optical Band Gaps of (Ba,Sr)SnO3 Films Grown by Molecular Beam Epitaxy*, J. Vac. Sci. Technol. A Vacuum, Surfaces, Film. **34**, 050601 (2016).

[4] D. J. Singh, D. A. Papaconstantopoulos, J. P. Julien, and F. Cyrot-Lackmann, *Electronic Structure of Ba(Sn,Sb)O3: Absence of Superconductivity*, Phys. Rev. B **44**, 9519 (1991).

[5] S. James Allen, S. Raghavan, T. Schumann, K.-M. Law, and S. Stemmer, *Conduction Band Edge Effective Mass of La-Doped BaSnO3*, Appl. Phys. Lett. **108**, 252107 (2016).

[6] H. J. H. M. Kim, U. Kim, H. J. H. M. Kim, T. H. Kim, H. S. Mun, B. G. Jeon, K. T. Hong, W. J. Lee, C. Ju, K. H. Kimy, and K. Char, *High Mobility in a Stable Transparent Perovskite Oxide*, Appl. Phys. Express **5**, 3 (2012).

[7] H. J. Kim, U. Kim, T. H. Kim, J. Kim, H. M. Kim, B.-G. Jeon, W.-J. Lee, H. S. Mun, K. T. Hong, J. Yu, K. Char, and K. H. Kim, *Physical Properties of Transparent Perovskite Oxides (Ba,La)SnO 3 with High Electrical Mobility at Room Temperature*, Phys. Rev. B **86**, 165205 (2012).

[8] W.-J. Lee, H. J. Kim, J. Kang, D. H. Jang, T. H. Kim, J. H. Lee, and K. H. Kim,

Transparent Perovskite Barium Stannate with High Electron Mobility and Thermal Stability, Annu. Rev. Mater. Res. **47**, 391 (2017).

[9] Z. Xia, C. Wang, N. K. Kalarickal, S. Stemmer, and S. Rajan, *Design of Transistors Using High-Permittivity Materials*, IEEE Trans. Electron Devices **66**, 896 (2019).

[10] A. Widera and H. Schäfer, *Übergangsformen Zwischen Zintlphasen Und Echten Salzen: Die Verbindungen A3BO (MIT A = Ca, Sr, Ba Und B = Sn, Pb)*, Mater. Res. Bull. **15**, 1805 (1980).

[11] J. Nuss, C. Mühle, K. Hayama, V. Abdolazimi, and H. Takagi, *Tilting Structures in Inverse Perovskites, M3TtO (M = Ca, Sr, Ba, Eu; Tt = Si, Ge, Sn, Pb)*, Acta Crystallogr. Sect. B Struct. Sci. Cryst. Eng. Mater. **71**, 300 (2015).

[12] T. Kariyado and M. Ogata, *Low-Energy Effective Hamiltonian and the Surface States of Ca 3 PbO*, J. Phys. Soc. Japan **81**, 064701 (2012).

[13] T. H. Hsieh, J. Liu, and L. Fu, *Topological Crystalline Insulators and Dirac Octets in Antiperovskites*, Phys. Rev. B **90**, 081112 (2014).

[14] Y. Obata, R. Yukawa, K. Horiba, H. Kumigashira, Y. Toda, S. Matsuishi, and H. Hosono, *ARPES Studies of the Inverse Perovskite Ca3PbO: Experimental Confirmation of a Candidate 3D Dirac Fermion System*, Phys. Rev. B **96**, 155109 (2017).

[15] A. Ikeda, T. Fukumoto, M. Oudah, J. N. Hausmann, S. Yonezawa, S. Kobayashi, M. Sato, C. Tassel, F. Takeiri, H. Takatsu, H. Kageyama, and Y. Maeno, *Theoretical Band Structure of the Superconducting Antiperovskite Oxide Sr3−xSnO*, Phys. B Condens. Matter **536**, 752 (2018).

[16] T. Kawakami, T. Okamura, S. Kobayashi, and M. Sato, *Topological Crystalline Materials of J=3/2 Electrons: Antiperovskites, Dirac Points, and High Winding*

Topological Superconductivity, Phys. Rev. X **8**, 041026 (2018).

[17] Y. Fang and J. Cano, *Higher-Order Topological Insulators in Antiperovskites*, Phys. Rev. B **101**, 245110 (2020).

[18] T. Kariyado and M. Ogata, *Three-Dimensional Dirac Electrons at the Fermi Energy in Cubic Inverse Perovskites: Ca 3 PbO and Its Family*, J. Phys. Soc. Japan **80**, 083704 (2011).

[19] C.-K. Chiu, Y.-H. Chan, X. Li, Y. Nohara, and A. P. Schnyder, *Type-II Dirac Surface States in Topological Crystalline Insulators*, Phys. Rev. B **95**, 035151 (2017).

[20] R. Arras, J. Gosteau, D. Huang, H. Nakamura, H. J. Zhao, C. Paillard, and L. Bellaiche, *Spin-Polarized Electronic States and Atomic Reconstructions at Antiperovskite Sr3SnO(001) Polar Surfaces*, Phys. Rev. B **104**, 045411 (2021).

[21] M. Oudah, A. Ikeda, J. N. Hausmann, S. Yonezawa, T. Fukumoto, S. Kobayashi, M. Sato, and Y. Maeno, *Superconductivity in the Antiperovskite Dirac-Metal Oxide Sr3-XSnO*, Nat. Commun. **7**, 3 (2016).

[22] M. Oudah, J. N. Hausmann, S. Kitao, A. Ikeda, S. Yonezawa, M. Seto, and Y. Maeno, *Evolution of Superconductivity with Sr-Deficiency in Antiperovskite Oxide Sr3−xSnO*, Sci. Rep. **9**, 1831 (2019).

[23] J. N. Hausmann, M. Oudah, A. Ikeda, S. Yonezawa, and Y. Maeno, *Controlled Synthesis of the Antiperovskite Oxide Superconductor Sr 3− x SnO*, Supercond. Sci. Technol. **31**, 055012 (2018).

[24] L. Fu and C. L. Kane, *Superconducting Proximity Effect and Majorana Fermions at the Surface of a Topological Insulator*, Phys. Rev. Lett. **100**, 096407 (2008).

[25] M. Leijnse and K. Flensberg, *Introduction to Topological Superconductivity and*

Majorana Fermions, Semicond. Sci. Technol. **27**, 124003 (2012).

[26] M. Schmidbauer, A. Kwasniewski, and J. Schwarzkopf, *High-Precision Absolute Lattice Parameter Determination of SrTiO 3 , DyScO 3 and NdGaO 3 Single Crystals*, Acta Crystallogr. Sect. B Struct. Sci. **68**, 8 (2012).

[27] K. Van Benthem, C. Elsässer, and R. H. French, *Bulk Electronic Structure of SrTiO3: Experiment and Theory*, J. Appl. Phys. **90**, 6156 (2001).

[28] H. P. R. Frederikse and W. R. Hosler, *Hall Mobility in SrTiO3*, Phys. Rev. **161**, 822 (1967).

[29] Y. Ayino, J. Yue, T. Wang, B. Jalan, and V. S. Pribiag, *Effects of Paramagnetic Pair-Breaking and Spin-Orbital Coupling on Multi-Band Superconductivity*, J. Phys. Condens. Matter **32**, 38LT02 (2020).

[30] P. Moetakef and T. A. Cain, *Metal–Insulator Transitions in Epitaxial Gd1−Sr TiO3 Thin Films Grown Using Hybrid Molecular Beam Epitaxy*, Thin Solid Films **583**, 129 (2015).

[31] K. Ahadi, L. Galletti, Y. Li, S. Salmani-Rezaie, W. Wu, and S. Stemmer, *Enhancing Superconductivity in SrTiO 3 Films with Strain*, Sci. Adv. **5**, 1 (2019).

[32] O. N. Tufte and P. W. Chapman, *Electron Mobility in Semiconducting Strontium Titanate*, Phys. Rev. **155**, 796 (1967).

[33] H. Yamada and G. R. Miller, *Point Defects in Reduced Strontium Titanate*, J. Solid State Chem. **6**, 169 (1973).

[34] J. F. Schooley, W. R. Hosler, and M. L. Cohen, *Superconductivity in Semiconducting SrTiO3*, Phys. Rev. Lett. **12**, 474 (1964).

[35] J. F. Schooley, W. R. Hosler, E. Ambler, J. H. Becker, M. L. Cohen, and C. S. Koonce, *Dependence of the Superconducting Transition Temperature on Carrier Concentration*

in Semiconducting SrTiO3, Phys. Rev. Lett. **14**, 305 (1965).

[36] C. S. Koonce, M. L. Cohen, J. F. Schooley, W. R. Hosler, and E. R. Pfeiffer, *Superconducting Transition Temperatures of Semiconducting SrTiO3*, Phys. Rev. **163**, 380 (1967).

[37] X. Lin, G. Bridoux, A. Gourgout, G. Seyfarth, S. Krämer, M. Nardone, B. Fauqué, and K. Behnia, *Critical Doping for the Onset of a Two-Band Superconducting Ground State in SrTiO3−δ*, Phys. Rev. Lett. **112**, 207002 (2014).

[38] M. N. Gastiasoro, J. Ruhman, and R. M. Fernandes, *Superconductivity in Dilute SrTiO3: A Review*, Ann. Phys. (N. Y). **417**, 168107 (2020).

[39] K. A. Müller and H. Burkard, *SrTiO3: An Intrinsic Quantum Paraelectric below 4 K*, Phys. Rev. B **19**, 3593 (1979).

[40] J. G. Bednorz and K. A. Müller, *Sr1−xCaxTiO3: An XY Quantum Ferroelectric with Transition to Randomness*, Phys. Rev. Lett. **52**, 2289 (1984).

[41] C. W. Rischau, X. Lin, C. P. Grams, D. Finck, S. Harms, J. Engelmayer, T. Lorenz, Y. Gallais, B. Fauqué, J. Hemberger, and K. Behnia, *A Ferroelectric Quantum Phase Transition inside the Superconducting Dome of Sr1−xCaxTiO3−δ*, Nat. Phys. **13**, 643 (2017).

[42] V. Lemanov, E. Smirnova, P. Syrnikov, and E. Tarakanov, *Phase Transitions and Glasslike Behavior*, Phys. Rev. B - Condens. Matter Mater. Phys. **54**, 3151 (1996).

[43] M. Itoh, R. Wang, Y. Inaguma, T. Yamaguchi, Y. J. Shan, and T. Nakamura, *Ferroelectricity Induced by Oxygen Isotope Exchange in Strontium Titanate Perovskite*, Phys. Rev. Lett. **82**, 3540 (1999).

[44] H. Uwe and T. Sakudo, *Stress-Induced Ferroelectricity and Soft Phonon Modes in SrTi*

O3, Phys. Rev. B **13**, 271 (1976).

[45] A. Verma, S. Raghavan, S. Stemmer, and D. Jena, *Ferroelectric Transition in Compressively Strained SrTiO 3 Thin Films*, Appl. Phys. Lett. **107**, 192908 (2015).

[46] R. Russell, N. Ratcliff, K. Ahadi, L. Dong, S. Stemmer, and J. W. Harter, *Ferroelectric Enhancement of Superconductivity in Compressively Strained SrTiO3 Films*, Phys. Rev. Mater. **3**, 91401 (2019).

[47] A. Stucky, G. W. Scheerer, Z. Ren, D. Jaccard, J.-M. Poumirol, C. Barreteau, E. Giannini, and D. van der Marel, *Isotope Effect in Superconducting N-Doped SrTiO3*, Sci. Rep. **6**, 37582 (2016).

[48] Y. Tomioka, N. Shirakawa, K. Shibuya, and I. H. Inoue, *Enhanced Superconductivity Close to a Non-Magnetic Quantum Critical Point in Electron-Doped Strontium Titanate*, Nat. Commun. **10**, 738 (2019).

[49] Y. Tomioka, N. Shirakawa, and I. H. Inoue, *Superconductivity Enhancement in Polar Metal Regions of Sr0.95Ba0.05TiO3 and Sr0.985Ca0.015TiO3 Revealed by Systematic Nb Doping*, Npj Quantum Mater. **7**, 111 (2022).

[50] C. Herrera, J. Cerbin, A. Jayakody, K. Dunnett, A. V. Balatsky, and I. Sochnikov, *Strain-Engineered Interaction of Quantum Polar and Superconducting Phases*, Phys. Rev. Mater. **3**, 124801 (2019).

[51] C. W. Rischau, D. Pulmannová, G. W. Scheerer, A. Stucky, E. Giannini, and D. van der Marel, *Isotope Tuning of the Superconducting Dome of Strontium Titanate*, Phys. Rev. Res. **4**, 013019 (2022).

[52] S. E. Rowley, C. Enderlein, J. F. de Oliveira, D. A. Tompsett, E. B. Saitovitch, S. S. Saxena, and G. G. Lonzarich, *Superconductivity in the Vicinity of a Ferroelectric*

Quantum Phase Transition, (2018).

[53] Y. Kedem, *Novel Pairing Mechanism for Superconductivity at a Vanishing Level of Doping Driven by Critical Ferroelectric Modes*, Phys. Rev. B **98**, 220505 (2018).

[54] J. M. Edge, Y. Kedem, U. Aschauer, N. A. Spaldin, and A. V. Balatsky, *Quantum Critical Origin of the Superconducting Dome in SrTiO3*, Phys. Rev. Lett. **115**, 247002 (2015).

[55] C. Enderlein, J. F. de Oliveira, D. A. Tompsett, E. B. Saitovitch, S. S. Saxena, G. G. Lonzarich, and S. E. Rowley, *Superconductivity Mediated by Polar Modes in Ferroelectric Metals*, Nat. Commun. **11**, 4852 (2020).

[56] M. N. Gastiasoro, T. V. Trevisan, and R. M. Fernandes, *Anisotropic Superconductivity Mediated by Ferroelectric Fluctuations in Cubic Systems with Spin-Orbit Coupling*, Phys. Rev. B **101**, 174501 (2020).

[57] J. Cheng, H. Yang, N. G. Combs, W. Wu, H. Kim, H. Chandrasekar, C. Wang, S. Rajan, S. Stemmer, and W. Lu, *Electron Transport of Perovskite Oxide BaSnO 3 on (110) DyScO 3 Substrate with Channel-Recess for Ferroelectric Field Effect Transistors*, Appl. Phys. Lett. **118**, 042105 (2021).

[58] J. Park, H. Paik, K. Nomoto, K. Lee, B.-E. E. Park, B. Grisafe, L.-C. C. Wang, S. Salahuddin, S. Datta, Y. Kim, D. Jena, H. G. Xing, and D. G. Schlom, *Fully Transparent Field-Effect Transistor with High Drain Current and on-off Ratio*, APL Mater. **8**, 011110 (2020).

[59] S. M. Sze and K. K. Ng, *Physics of Semiconductor Devices* (John Wiley & Sons, Inc., Hoboken, NJ, USA, 2006).

[60] L. J. van der Pauw, *A Method of Measuring Specific Resistivity and Hall Effect of Discs of Arbitrary Shape*, Philips Res. Reports **13**, (1958).

[61] T. A. Cain, A. P. Kajdos, and S. Stemmer, *La-Doped SrTiO 3 Films with Large Cryogenic Thermoelectric Power Factors*, Appl. Phys. Lett. **102**, 182101 (2013).

[62] Y. Kozuka, Y. Hikita, C. Bell, and H. Y. Hwang, *Dramatic Mobility Enhancements in Doped SrTiO3 Thin Films by Defect Management*, Appl. Phys. Lett. **97**, 8 (2010).

[63] D. G. Schlom, *Perspective: Oxide Molecular-Beam Epitaxy Rocks!*, APL Mater. **3**, 062403 (2015).

[64] J. Y. Tsao, *Materials Fundamentals of Molecular Beam Epitaxy* (Elsevier, 1993).

[65] B. Jalan, P. Moetakef, and S. Stemmer, *Molecular Beam Epitaxy of SrTiO3 with a Growth Window*, Appl. Phys. Lett. **95**, 032906 (2009).

[66] J. H. Haeni, C. D. Theis, and D. G. Schlom, *RHEED Intensity Oscillations for the Stoichiometric Growth of SrTiO3 Thin Films by Reactive Molecular Beam Epitaxy*, J. Electroceramics **4**, 385 (2000).

[67] B. Jalan, R. Engel-Herbert, N. J. Wright, and S. Stemmer, *Growth of High-Quality SrTiO3 Films Using a Hybrid Molecular Beam Epitaxy Approach*, J. Vac. Sci. Technol. A Vacuum, Surfaces, Film. **27**, 461 (2009).

[68] B. Jalan, J. Cagnon, T. E. Mates, and S. Stemmer, *Analysis of Carbon in SrTiO3 Grown by Hybrid Molecular Beam Epitaxy*, J. Vac. Sci. Technol. A Vacuum, Surfaces, Film. **27**, 1365 (2009).

[69] M. Brahlek, A. Sen Gupta, J. Lapano, J. Roth, H. Zhang, L. Zhang, R. Haislmaier, and R. Engel-Herbert, *Frontiers in the Growth of Complex Oxide Thin Films: Past, Present, and Future of Hybrid MBE*, Adv. Funct. Mater. **28**, 1702772 (2018).

[70] A. P. Kajdos, N. G. Combs, and S. Stemmer, *Hybrid Oxide Molecular Beam Epitaxy*, in *Epitaxial Growth of Complex Metal Oxides* (Elsevier, 2022), pp. 53–74.

[71] A. P. Kajdos and S. Stemmer, *Surface Reconstructions in Molecular Beam Epitaxy of SrTiO 3*, Appl. Phys. Lett. **105**, 191901 (2014).

[72] R. C. Haislmaier, R. Engel-Herbert, and V. Gopalan, *Stoichiometry as Key to Ferroelectricity in Compressively Strained SrTiO 3 Films*, Appl. Phys. Lett. **109**, 032901 (2016).

[73] P. Moetakef, T. A. Cain, D. G. Ouellette, J. Y. Zhang, D. O. Klenov, A. Janotti, C. G. Van de Walle, S. Rajan, S. J. Allen, and S. Stemmer, *Electrostatic Carrier Doping of GdTiO 3 /SrTiO 3 Interfaces*, Appl. Phys. Lett. **99**, 232116 (2011).

[74] C. A. Jackson, P. Moetakef, S. James Allen, and S. Stemmer, *Capacitance-Voltage Analysis of High-Carrier-Density SrTiO 3 /GdTiO 3 Heterostructures*, Appl. Phys. Lett. **100**, 232106 (2012).

[75] Y. Matsubara, K. S. Takahashi, Y. Tokura, and M. Kawasaki, *Single-Crystalline BaTiO3 Films Grown by Gas-Source Molecular Beam Epitaxy*, Appl. Phys. Express **7**, 125502 (2014).

[76] K. Ahadi, L. Galletti, and S. Stemmer, *Evidence of a Topological Hall Effect in Eu 1− x Sm x TiO 3*, Appl. Phys. Lett. **111**, 172403 (2017).

[77] K. Ahadi, H. Kim, and S. Stemmer, *Spontaneous Hall Effects in the Electron System at the SmTiO3/EuTiO3 Interface*, APL Mater. **6**, 2 (2018).

[78] Z. Lebens-Higgins, D. O. Scanlon, H. Paik, S. Sallis, Y. Nie, M. Uchida, N. F. Quackenbush, M. J. Wahila, G. E. Sterbinsky, D. A. Arena, J. C. Woicik, D. G. Schlom, and L. F. J. Piper, *Direct Observation of Electrostatically Driven Band Gap Renormalization in a Degenerate Perovskite Transparent Conducting Oxide*, Phys. Rev. Lett. **116**, 027602 (2016).

[79] M. Y. Tsai, M. E. White, and J. S. Speck, *Investigation of (110) SnO2 Growth Mechanisms on TiO2 Substrates by Plasma-Assisted Molecular Beam Epitaxy*, J. Appl. Phys. **106**, 024911 (2009).

[80] S. Raghavan, T. Schumann, H. Kim, J. Y. Zhang, T. A. Cain, and S. Stemmer, *High-Mobility BaSnO3 Grown by Oxide Molecular Beam Epitaxy*, APL Mater. **4**, 016106 (2016).

[81] A. Prakash, J. Dewey, H. Yun, J. S. Jeong, K. A. Mkhoyan, and B. Jalan, *Hybrid Molecular Beam Epitaxy for the Growth of Stoichiometric $BaSnO_3$*, J. Vac. Sci. Technol. A Vacuum, Surfaces, Film. **33**, 060608 (2015).

[82] T. Wang, L. R. Thoutam, A. Prakash, W. Nunn, G. Haugstad, and B. Jalan, *Defect-Driven Localization Crossovers in MBE-Grown La-Doped SrSnO3 Films*, Phys. Rev. Mater. **1**, 061601 (2017).

[83] R. H. Lamoreaux, D. L. Hildenbrand, and L. Brewer, *High-Temperature Behavior of Oxides II*, J. Phys. Chem. Ref. Data **16**, 419 (1986).

[84] H. Paik, Z. Chen, E. Lochocki, A. Seidner H., A. Verma, N. Tanen, J. Park, M. Uchida, S. Shang, B. Zhou, M. Brützam, R. Uecker, Z. Liu, D. Jena, K. M. Shen, D. A. Muller, and D. G. Schlom, *Adsorption-Controlled Growth of La-Doped BaSnO 3 by Molecular-Beam Epitaxy*, APL Mater. **5**, 116107 (2017).

[85] J. S. Speck and W. Pompe, *Domain Configurations Due to Multiple Misfit Relaxation Mechanisms in Epitaxial Ferroelectric Thin Films. I. Theory*, J. Appl. Phys. **76**, 466 (1994).

[86] T. Wang, K. Ganguly, P. Marshall, P. Xu, and B. Jalan, *Critical Thickness and Strain Relaxation in Molecular Beam Epitaxy-Grown SrTiO 3 Films*, Appl. Phys. Lett. **103**,

212904 (2013).

[87] W. Wu, N. G. Combs, and S. Stemmer, *Molecular Beam Epitaxy of Phase-Pure Antiperovskite Sr 3 SnO Thin Films*, Appl. Phys. Lett. **119**, 161903 (2021).

[88] W. Wu, N. G. Combs, and S. Stemmer, *Revealing the Intrinsic Transport Properties of Antiperovskite Sr 3 SnO Thin Films*, Appl. Phys. Lett. **121**, 233101 (2022).

[89] N. G. Combs, W. Wu, and S. Stemmer, *Stoichiometry Control in Molecular Beam Epitaxy of BaSnO3*, Phys. Rev. Mater. **4**, 014604 (2020).

[90] N. G. Combs, H. Jeong, R. Russell, L. Kautzsch, T. N. Pardue, T. E. Mates, S. D. Wilson, J. W. Harter, and S. Stemmer, *Ferroelectricity and Superconductivity in Strained EuxSr1−xTiO3 Films*, Phys. Rev. B **107**, 094504 (2023).

[91] W. J. Lee, H. J. Kim, E. Sohn, T. H. Kim, J. Y. Park, W. Park, H. Jeong, T. Lee, J. H. Kim, K. Y. Choi, and K. H. Kim, *Enhanced Electron Mobility in Epitaxial (Ba,La)SnO3 Films on BaSnO3(001) Substrates*, Appl. Phys. Lett. **108**, 665 (2016).

[92] P. V. Wadekar, J. Alaria, M. O'Sullivan, N. L. O. Flack, T. D. Manning, L. J. Phillips, K. Durose, O. Lozano, S. Lucas, J. B. Claridge, and M. J. Rosseinsky, *Improved Electrical Mobility in Highly Epitaxial La:BaSnO 3 Films on SmScO 3 (110) Substrates*, Appl. Phys. Lett. **105**, 052104 (2014).

[93] K. Ganguly, P. Ambwani, P. Xu, J. S. Jeong, K. A. Mkhoyan, C. Leighton, and B. Jalan, *Structure and Transport in High Pressure Oxygen Sputter-Deposited BaSnO 3−δ*, APL Mater. **3**, 062509 (2015).

[94] S. Raghavan, Improving Transport in Complex Oxide Heterostructures : High Density 2DELs and High Mobility Stannates, University of California - Santa Barbara, 2017.

[95] C. R. Freeze, Molecular Beam Epitaxy of Wide-Band Gap Perovskite Oxides: (Ba,

Sr)TiO3 and BaSnO3, University of California - Santa Barbara, 2019.

[96] T. Razzak, H. Xue, Z. Xia, S. Hwang, A. Khan, W. Lu, and S. Rajan, *Ultra-Wide Band Gap Materials for High Frequency Applications*, 2018 IEEE MTT-S Int. Microw. Work. Ser. Adv. Mater. Process. RF THz Appl. IMWS-AMP 2018 17 (2018).

[97] J. Cheng, C. Wang, C. Freeze, O. Shoron, N. Combs, H. Yang, N. K. Kalarickal, Z. Xia, S. Stemmer, S. Rajan, and W. Lu, *High-Current Perovskite Oxide BaTiO3/BaSnO3 Heterostructure Field Effect Transistors*, IEEE Electron Device Lett. **41**, 621 (2020).

[98] J. Cheng, H. Yang, C. Wang, N. Combs, C. Freeze, O. Shoron, W. Wu, N. K. Kalarickal, H. Chandrasekar, S. Stemmer, S. Rajan, W. Lu, N. Combs, C. Freeze, O. Shoron, S. Stemmer, S. Rajan, and W. Lu, *Nanoscale Etching of Perovskite Oxides for Field Effect Transistor Applications*, J. Vac. Sci. Technol. B **38**, 012201 (2020).

[99] O. F. Shoron, S. Raghavan, C. R. Freeze, and S. Stemmer, *BaTiO 3 /SrTiO 3 Heterostructures for Ferroelectric Field Effect Transistors*, Appl. Phys. Lett. **110**, 232902 (2017).

[100] L. Bjaalie, B. Himmetoglu, L. Weston, A. Janotti, and C. G. Van de Walle, *Oxide Interfaces for Novel Electronic Applications*, New J. Phys. **16**, 025005 (2014).

[101] R. J. Terry, N. Combs, C. D. Mcmillen, S. Stemmer, and J. W. Kolis, *Hydrothermal Growth of BaSnO 3 Single Crystals for Wide Bandgap Applications*, J. Cryst. Growth **536**, 125529 (2020).

[102] C. D. Theis, J. Yeh, D. G. Schlom, M. E. Hawley, and G. W. Brown, *Adsorption-Controlled Growth of PbTiO3 by Reactive Molecular Beam Epitaxy*, Thin Solid Films **325**, 107 (1998).

[103] D. O. Scanlon, *Defect Engineering of BaSnO 3 for High-Performance Transparent*

Conducting Oxide Applications, Phys. Rev. B **87**, 161201 (2013).

[104] L. Weston, L. Bjaalie, K. Krishnaswamy, and C. G. Van de Walle, *Origins of n -Type Doping Difficulties in Perovskite Stannates*, Phys. Rev. B **97**, 054112 (2018).

[105] U. Kumar and S. Upadhyay, *Structural, Optical and Electrical Properties of Ruddlesden Popper Oxide Ba2SnO4*, J. Electron. Mater. **48**, 5279 (2019).

[106] E. J. Tarsa, E. A. Hachfeld, F. T. Quinlan, J. S. Speck, and M. Eddy, *Growth-Related Stress and Surface Morphology in Homoepitaxial SrTiO 3 Films*, Appl. Phys. Lett. **490**, 490 (1995).

[107] D. G. Schlom, J. H. Haeni, J. Lettieri, C. D. Theis, W. Tian, J. C. Jiang, and X. Q. Pan, *Oxide Nano-Engineering Using MBE*, Mater. Sci. Eng. B Solid-State Mater. Adv. Technol. **87**, 282 (2001).

[108] T. Ohnishi, M. Lippmaa, T. Yamamoto, S. Meguro, and H. Koinuma, *Improved Stoichiometry and Misfit Control in Perovskite Thin Film Formation at a Critical Fluence by Pulsed Laser Deposition*, Appl. Phys. Lett. **87**, 241919 (2005).

[109] A. Prakash, P. Xu, X. Wu, G. Haugstad, X. Wang, and B. Jalan, *Adsorption-Controlled Growth and the Influence of Stoichiometry on Electronic Transport in Hybrid Molecular Beam Epitaxy-Grown BaSnO 3 Films*, J. Mater. Chem. C **5**, 5730 (2017).

[110] T. Wang, K. C. Pitike, Y. Yuan, S. M. Nakhmanson, V. Gopalan, and B. Jalan, *Chemistry, Growth Kinetics, and Epitaxial Stabilization of Sn 2+ in Sn-Doped SrTiO 3 Using (CH 3) 6 Sn 2 Tin Precursor*, APL Mater. **4**, 126111 (2016).

[111] S. Suzuki, T. Takeda, A. Ando, T. Oyama, N. Wada, H. Niimi, and H. Takagi, *Effect of Sn 2+ Ion Substitution on Dielectric Properties of (Ba,Ca)TiO 3 Ferroelectric Ceramics*, Jpn. J. Appl. Phys. **49**, 09MC04 (2010).

[112] S. Suzuki, T. Takeda, A. Ando, and H. Takagi, *Ferroelectric Phase Transition in Sn2+ Ions Doped (Ba,Ca)TiO3 Ceramics*, Appl. Phys. Lett. **96**, 132903 (2010).

[113] S. KC, A. J. E. Rowberg, L. Weston, and C. G. Van de Walle, *First-Principles Study of Antisite Defects in Perovskite Stannates*, J. Appl. Phys. **126**, 195701 (2019).

[114] Y. Chiang, D. P. Birnie, and W. D. Kingery, *Physical Ceramics: Principles for Ceramic Science and Engineering* (John Wiley & Sons, New York, 1997).

[115] E. S. Hellman, *Effects of Oxygen on the Sublimation of Alkaline Earths from Effusion Cells*, J. Vac. Sci. Technol. B Microelectron. Nanom. Struct. **12**, 1178 (1994).

[116] S. Suetsugu, K. Hayama, A. W. Rost, J. Nuss, C. Mühle, J. Kim, K. Kitagawa, and H. Takagi, *Magnetotransport in Sr3PbO Antiperovskite*, Phys. Rev. B **98**, 115203 (2018).

[117] Y. Obata, S. Matsuishi, and H. Hosono, *Flux Growth and Magneto-Transport Properties of Cubic Antiperovskite Ca3PbO Single Crystals*, Mater. Res. Bull. **106**, 1 (2018).

[118] H. Nakamura, D. Huang, J. Merz, E. Khalaf, P. Ostrovsky, A. Yaresko, D. Samal, and H. Takagi, *Robust Weak Antilocalization Due to Spin-Orbital Entanglement in Dirac Material Sr3SnO*, Nat. Commun. **11**, 1161 (2020).

[119] D. Huang, H. Nakamura, K. Küster, A. Yaresko, D. Samal, N. B. M. M. Schröter, V. N. Strocov, U. Starke, and H. Takagi, *Unusual Valence State in the Antiperovskites Sr3SnO and Sr3PbO Revealed by X-Ray Photoelectron Spectroscopy*, Phys. Rev. Mater. **3**, 124203 (2019).

[120] D. Samal, H. Nakamura, and H. Takagi, *Molecular Beam Epitaxy of Three-Dimensional Dirac Material Sr 3 PbO*, APL Mater. **4**, 076101 (2016).

[121] Y. Ma, A. Edgeton, H. Paik, B. D. Faeth, C. T. Parzyck, B. Pamuk, S. Shang, Z. Liu, K. M. Shen, D. G. Schlom, and C. Eom, *Realization of Epitaxial Thin Films of the*

Topological Crystalline Insulator Sr 3 SnO, Adv. Mater. **32**, 2000809 (2020).

[122] M. M. Nasrallah and D. L. Douglass, *Ionic and Electronic Conductivity in Y2O3-Doped Monoclinic ZrO2*, J. Electrochem. Soc. **121**, 255 (1974).

[123] R. Engel-Herbert, Y. Hwang, J. Cagnon, and S. Stemmer, *Metal-Oxide-Semiconductor Capacitors with ZrO2 Dielectrics Grown on In0.53Ga0.47As by Chemical Beam Deposition*, Appl. Phys. Lett. **95**, 062908 (2009).

[124] S. Salmani-Rezaie, K. Ahadi, W. M. Strickland, and S. Stemmer, *Order-Disorder Ferroelectric Transition of Strained SrTiO3*, Phys. Rev. Lett. **125**, 087601 (2020).

[125] S. Salmani-Rezaie, K. Ahadi, and S. Stemmer, *Polar Nanodomains in a Ferroelectric Superconductor*, Nano Lett. **20**, 6542 (2020).

[126] U. Bianchi, W. Kleemann, and J. G. Bednorz, *Raman Scattering of Ferroelectric Sr 1-x Ca x TiO 3 , X=0.007*, J. Phys. Condens. Matter **6**, 1229 (1994).

[127] E. K. H. Salje, O. Aktas, M. A. Carpenter, V. V. Laguta, and J. F. Scott, *Domains within Domains and Walls within Walls: Evidence for Polar Domains in Cryogenic SrTiO3*, Phys. Rev. Lett. **111**, 247603 (2013).

[128] K. A. Müller, W. Berlinger, and E. Tosatti, *Indication for a Novel Phase in the Quantum Paraelectric Regime of SrTiO3*, Zeitschrift Für Phys. B Condens. Matter **84**, 277 (1991).

[129] H. Uwe, H. Yamaguchi, and T. Sakudo, *Ferroelectric Microregion in KTa 1− x Nb x O 3 and SrTiO 3*, Ferroelectrics **96**, 123 (1989).

[130] S. Salmani-Rezaie, L. Galletti, T. Schumann, R. Russell, H. Jeong, Y. Li, J. W. Harter, and S. Stemmer, *Superconductivity in Magnetically Doped SrTiO 3*, Appl. Phys. Lett. **118**, 202602 (2021).

[131] A. D. Caviglia, S. Gariglio, N. Reyren, D. Jaccard, T. Schneider, M. Gabay, S. Thiel, G.

Hammerl, J. Mannhart, and J. M. Triscone, *Electric Field Control of the LaAlO3/SrTiO3 Interface Ground State*, Nature **456**, 624 (2008).

[132] D. Stornaiuolo, C. Cantoni, G. M. De Luca, R. Di Capua, E. Di Gennaro, G. Ghiringhelli, B. Jouault, D. Marrè, D. Massarotti, F. M. Granozio, I. Pallecchi, C. Piamonteze, S. Rusponi, F. Tafuri, and M. Salluzzo, *Tunable Spin Polarization and Superconductivity in Engineered Oxide Interfaces*, Nat. Mater. **15**, 278 (2016).

[133] A. D. Caviglia, M. Gabay, S. Gariglio, N. Reyren, C. Cancellieri, and J.-M. Triscone, *Tunable Rashba Spin-Orbit Interaction at Oxide Interfaces*, Phys. Rev. Lett. **104**, 126803 (2010).

[134] G. Khalsa, B. Lee, and A. H. MacDonald, *Theory of T2g Electron-Gas Rashba Interactions*, Phys. Rev. B **88**, 041302 (2013).

[135] A. Joshua, S. Pecker, J. Ruhman, E. Altman, and S. Ilani, *A Universal Critical Density Underlying the Physics of Electrons at the LaAlO3/SrTiO3 Interface*, Nat. Commun. **3**, 1129 (2012).

[136] H. Noad, E. M. Spanton, K. C. Nowack, H. Inoue, M. Kim, T. A. Merz, C. Bell, Y. Hikita, R. Xu, W. Liu, A. Vailionis, H. Y. Hwang, and K. A. Moler, *Variation in Superconducting Transition Temperature Due to Tetragonal Domains in Two-Dimensionally Doped SrTiO3*, Phys. Rev. B **94**, 174516 (2016).

[137] S. Hameed, D. Pelc, Z. W. Anderson, A. Klein, R. J. Spieker, L. Yue, B. Das, J. Ramberger, M. Lukas, Y. Liu, M. J. Krogstad, R. Osborn, Y. Li, C. Leighton, R. M. Fernandes, and M. Greven, *Enhanced Superconductivity and Ferroelectric Quantum Criticality in Plastically Deformed Strontium Titanate*, Nat. Mater. **21**, 54 (2022).

[138] D. Pelc, Z. Anderson, B. Yu, C. Leighton, and M. Greven, *Universal Superconducting*

Precursor in Three Classes of Unconventional Superconductors, Nat. Commun. **10**, 2729 (2019).

[139] P. Gao, S. Yang, R. Ishikawa, N. Li, B. Feng, A. Kumamoto, N. Shibata, P. Yu, and Y. Ikuhara, *Atomic-Scale Measurement of Flexoelectric Polarization at SrTiO3 Dislocations*, Phys. Rev. Lett. **120**, 267601 (2018).

[140] M. Smidman, M. B. Salamon, H. Q. Yuan, and D. F. Agterberg, *Superconductivity and Spin–Orbit Coupling in Non-Centrosymmetric Materials: A Review*, Reports Prog. Phys. **80**, 036501 (2017).

[141] L. P. Gor'kov and E. I. Rashba, *Superconducting 2d System with Lifted Spin Degeneracy: Mixed Singlet-Triplet State*, Phys. Rev. Lett. **87**, 37004 (2001).

[142] V. M. Edelshtein, *Characteristics of the Cooper Pairing in Two-Dimensional Noncentrosymmetric Electron Systems*, J. Exp. Theor. Phys. **95**, 2151 (1989).

[143] N. Pertsev, A. Tagantsev, and N. Setter, *Phase Transitions and Strain-Induced Ferroelectricity in Epitaxial Thin Films*, Phys. Rev. B - Condens. Matter Mater. Phys. **61**, R825 (2000).

[144] P. W. Anderson and E. I. Blount, *Symmetry Considerations on Martensitic Transformations: "Ferroelectric" Metals?*, Phys. Rev. Lett. **14**, 217 (1965).

[145] N. A. Benedek and T. Birol, *"Ferroelectric" Metals Reexamined: Fundamental Mechanisms and Design Considerations for New Materials*, J. Mater. Chem. C **4**, 4000 (2016).

[146] W. X. Zhou and A. Ariando, *Review on Ferroelectric/Polar Metals*, Jpn. J. Appl. Phys. **59**, SI0802 (2020).

[147] F. Gu, J. Wang, Z.-J. Lang, and W. Ku, *Quantum Fluctuation of Ferroelectric Order in*

Polar Metals, 1 (2023).

[148] Y. Shi, Y. Guo, X. Wang, A. J. Princep, D. Khalyavin, P. Manuel, Y. Michiue, A. Sato, K. Tsuda, S. Yu, M. Arai, Y. Shirako, M. Akaogi, N. Wang, K. Yamaura, and A. T. Boothroyd, *A Ferroelectric-like Structural Transition in a Metal*, Nat. Mater. **12**, 1024 (2013).

[149] J. Engelmayer, X. Lin, F. Koç, C. P. Grams, J. Hemberger, K. Behnia, and T. Lorenz, *Ferroelectric Order versus Metallicity in Sr1−xCaxTiO3−δ*, Phys. Rev. B **100**, 195121 (2019).

[150] J. Wang, L. Yang, C. W. Rischau, Z. Xu, Z. Ren, T. Lorenz, J. Hemberger, X. Lin, and K. Behnia, *Charge Transport in a Polar Metal*, Npj Quantum Mater. **4**, 61 (2019).

[151] R. Blinc, B. Zalar, V. V. Laguta, and M. Itoh, *Order-Disorder Component in the Phase Transition Mechanism of 18O Enriched Strontium Titanate*, Phys. Rev. Lett. **94**, 2 (2005).

[152] B. Zalar, A. Lebar, J. Seliger, R. Blinc, V. V. Laguta, and M. Itoh, *NMR Study of Disorder in BaTiO 3 and SrTiO 3*, Phys. Rev. B - Condens. Matter Mater. Phys. **71**, 1 (2005).

[153] T. Nakatani, A. Yoshiasa, A. Nakatsuka, T. Hiratoko, T. Mashimo, M. Okube, and S. Sasaki, *Variable-Temperature Single-Crystal X-Ray Diffraction Study of Tetragonal and Cubic Perovskite-Type Barium Titanate Phases*, Acta Crystallogr. Sect. B Struct. Sci. Cryst. Eng. Mater. **72**, 151 (2016).

[154] A. M. Pugachev, V. I. Kovalevskii, N. V. Surovtsev, S. Kojima, S. A. Prosandeev, I. P. Raevski, and S. I. Raevskaya, *Broken Local Symmetry in Paraelectric BaTiO3 Proved by Second Harmonic Generation*, Phys. Rev. Lett. **108**, 247601 (2012).

[155] E. A. Stern, *Character of Order-Disorder and Displacive Components in Barium*

Titanate, Phys. Rev. Lett. **93**, 037601 (2004).

[156] Y. Girshberg and Y. Yacoby, *Ferroelectric Phase Transitions and Off-Centre Displacements in Systems with Strong Electron-Phonon Interaction*, J. Phys. Condens. Matter **11**, 9807 (1999).

[157] S. Salmani-Rezaie, H. Jeong, R. Russell, J. W. Harter, and S. Stemmer, *Role of Locally Polar Regions in the Superconductivity of SrTiO3*, Phys. Rev. Mater. **5**, 104801 (2021).

[158] S. Salmani-Rezaie, H. Kim, K. Ahadi, and S. Stemmer, *Lattice Relaxations around Individual Dopant Atoms in SrTiO3*, Phys. Rev. Mater. **3**, 114404 (2019).

[159] A. Bencan, E. Oveisi, S. Hashemizadeh, V. K. Veerapandiyan, T. Hoshina, T. Rojac, M. Deluca, G. Drazic, and D. Damjanovic, *Atomic Scale Symmetry and Polar Nanoclusters in the Paraelectric Phase of Ferroelectric Materials*, Nat. Commun. **12**, 3509 (2021).

[160] W. Zhong, R. D. King-Smith, and D. Vanderbilt, *Giant LO-TO Splittings in Perovskite Ferroelectrics*, Phys. Rev. Lett. **72**, 3618 (1994).

[161] A. Bussmann-Holder, *The Polarizability Model for Ferroelectricity in Perovskite Oxides*, J. Phys. Condens. Matter **24**, 273202 (2012).

[162] G. A. Samara, *The Relaxational Properties of Compositionally Disordered ABO 3 Perovskites*, J. Phys. Condens. Matter **15**, R367 (2003).

[163] H. Takenaka, I. Grinberg, S. Liu, and A. M. Rappe, *Slush-like Polar Structures in Single-Crystal Relaxors*, Nature **546**, 391 (2017).

[164] A. A. Bokov and Z. G. Ye, *Recent Progress in Relaxor Ferroelectrics with Perovskite Structure*, J. Mater. Sci. **41**, 31 (2006).

[165] A. Kumar, J. N. Baker, P. C. Bowes, M. J. Cabral, S. Zhang, E. C. Dickey, D. L. Irving, and J. M. LeBeau, *Atomic-Resolution Electron Microscopy of Nanoscale Local*

Structure in Lead-Based Relaxor Ferroelectrics, Nat. Mater. **20**, 62 (2021).

[166] A. Simon, J. Ravez, and M. Maglione, *The Crossover from a Ferroelectric to a Relaxor State in Lead-Free Solid Solutions*, J. Phys. Condens. Matter **16**, 963 (2004).

[167] R. Muralidharan, K. Meera, and Y. H. Jeong, *Evidence on the Quantum Critical Point in EuTiO3–SrTiO3 Solid Solution*, Phys. B Condens. Matter **620**, 3 (2021).

[168] H. W. Jang, A. Kumar, S. Denev, M. D. Biegalski, P. Maksymovych, C. W. Bark, C. T. Nelson, C. M. Folkman, S. H. Baek, N. Balke, C. M. Brooks, D. A. Tenne, D. G. Schlom, L. Q. Chen, X. Q. Pan, S. V. Kalinin, V. Gopalan, and C. B. Eom, *Ferroelectricity in Strain-Free SrTiO3 Thin Films*, Phys. Rev. Lett. **104**, 197601 (2010).

[169] H. Jeong, R. Russell, N. G. Combs, T. N. Pardue, J. W. Harter, and S. Stemmer, *Similarity in the Critical Thicknesses for Superconductivity and Ferroelectricity in Strained SrTiO 3 Films*, Appl. Phys. Lett. **121**, 012601 (2022).

[170] K. Michaeli, A. C. Potter, and P. A. Lee, *Superconducting and Ferromagnetic Phases in SrTiO3 /LaAlO3 Oxide Interface Structures: Possibility of Finite Momentum Pairing*, Phys. Rev. Lett. **108**, 117003 (2012).

[171] M. Kim, Y. Kozuka, C. Bell, Y. Hikita, and H. Y. Hwang, *Intrinsic Spin-Orbit Coupling in Superconducting δ -Doped SrTiO 3 Heterostructures*, Phys. Rev. B **86**, 085121 (2012).

[172] D. Olaya, F. Pan, C. T. Rogers, and J. C. Price, *Superconductivity in La-Doped Strontium Titanate Thin Films*, Appl. Phys. Lett. **84**, 4020 (2004).

[173] T. Schumann, L. Galletti, H. Jeong, K. Ahadi, W. M. Strickland, S. Salmani-Rezaie, and S. Stemmer, *Possible Signatures of Mixed-Parity Superconductivity in Doped Polar SrTiO3 Films*, Phys. Rev. B **101**, 100503 (2020).

[174] A. A. Abrikosov and L. P. Gor'kov, *Contribution to the Theory of Superconducting Alloys with Paramagnetic Impurities*, Sov. Phys. JETP **12**, (1961).

[175] J. M. Edge and A. V. Balatsky, *Upper Critical Field as a Probe for Multiband Superconductivity in Bulk and Interfacial STO*, J. Supercond. Nov. Magn. **28**, 2373 (2015).

[176] F. Hunte, J. Jaroszynski, A. Gurevich, D. C. Larbalestier, R. Jin, A. S. Sefat, M. A. McGuire, B. C. Sales, D. K. Christen, and D. Mandrus, *Two-Band Superconductivity in LaFeAsO0.89F0.11 at Very High Magnetic Fields*, Nature **453**, 903 (2008).

[177] A. Golubov and I. Mazin, *Effect of Magnetic and Nonmagnetic Impurities on Highly Anisotropic Superconductivity*, Phys. Rev. B - Condens. Matter Mater. Phys. **55**, 15146 (1997).

[178] P. A. Frigeri, D. F. Agterberg, A. Koga, and M. Sigrist, *Superconductivity without Inversion Symmetry: MnSi versus CePt 3Si*, Phys. Rev. Lett. **92**, 6 (2004).

[179] S. Fujimoto, *Electron Correlation and Pairing States in Superconductors without Inversion Symmetry*, J. Phys. Soc. Japan **76**, 051008 (2007).

[180] M. S. Scheurer, M. Hoyer, and J. Schmalian, *Pair Breaking in Multiorbital Superconductors: An Application to Oxide Interfaces*, Phys. Rev. B **92**, 014518 (2015).

[181] S. Kanasugi and Y. Yanase, *Multiorbital Ferroelectric Superconductivity in Doped SrTiO3*, Phys. Rev. B **100**, 094504 (2019).

[182] S. Kanasugi and Y. Yanase, *Spin-Orbit-Coupled Ferroelectric Superconductivity*, Phys. Rev. B **98**, 024521 (2018).

[183] O. Dimitrova and M. V. Feigel'man, *Theory of a Two-Dimensional Superconductor with Broken Inversion Symmetry*, Phys. Rev. B **76**, 014522 (2007).

[184] M. S. Scheurer and J. Schmalian, *Topological Superconductivity and Unconventional Pairing in Oxide Interfaces*, Nat. Commun. **6**, 6005 (2015).

[185] M. S. Scheurer, *Mechanism, Time-Reversal Symmetry, and Topology of Superconductivity in Noncentrosymmetric Systems*, Phys. Rev. B **93**, 174509 (2016).

[186] A. V. Balatsky, I. Vekhter, and J. X. Zhu, *Impurity-Induced States in Conventional and Unconventional Superconductors*, Rev. Mod. Phys. **78**, 373 (2006).

[187] A. P. Mackenzie and Y. Maeno, *The Superconductivity of Sr2RuO4 and the Physics of Spin-Triplet Pairing*, Rev. Mod. Phys. **75**, 657 (2003).

[188] A. Ohtomo and H. Y. Hwang, *Surface Depletion in Doped SrTiO3 Thin Films*, Appl. Phys. Lett. **84**, 1716 (2004).

[189] H. Jeong, N. G. Combs, S. Munyan, A. Rashidi, and S. Stemmer, *Reducing Surface Depletion of Superconducting SrTiO 3 Films with EuTiO 3 Capping Layers*, Appl. Phys. Lett. **119**, 162601 (2021).

[190] L. Sagarna, S. Populoh, A. Shkabko, J. Eilertsen, A. E. Maegli, R. Hauert, M. Schrade, L. Karvonen, and A. Weidenkaff, *Influence of the Oxygen Content on the Electronic Transport Properties of SrxEu1- XTiO3-δ*, J. Phys. Chem. C **118**, 7821 (2014).

[191] Z. Guguchia, A. Shengelaya, H. Keller, J. Köhler, and A. Bussmann-Holder, *Tuning the Structural Instability of SrTiO3 by Eu Doping: The Phase Diagram of Sr1−xEuxTiO3*, Phys. Rev. B **85**, 134113 (2012).

[192] C. T. Wolowiec, B. D. White, and M. B. Maple, *Conventional Magnetic Superconductors*, Phys. C Supercond. Its Appl. **514**, 113 (2015).

[193] P. W. Anderson, *Theory of Dirty Superconductors*, J. Phys. Chem. Solids **11**, 26 (1959).

[194] C. Collignon, B. Fauqué, A. Cavanna, U. Gennser, D. Mailly, and K. Behnia, *Superfluid*

Density and Carrier Concentration across a Superconducting Dome: The Case of Strontium Titanate, Phys. Rev. B **96**, 224506 (2017).

[195] H. Suzuki, H. Bando, Y. Ootuka, I. H. Inoue, T. Yamamoto, K. Takahashi, and Y. Nishihara, *Superconductivity in Single-Crystalline S r 1- x L a x T i O 3*, J. Phys. Soc. Japan **65**, 1529 (1996).

[196] Y. Gindikin and V. A. Sablikov, *Electron Correlations Due to Pair Spin–Orbit Interaction in 2D Electron Systems*, Phys. E Low-Dimensional Syst. Nanostructures **143**, 115328 (2022).

[197] J. Hutchinson, J. E. Hirsch, and F. Marsiglio, *Enhancement of Superconducting Tc Due to the Spin-Orbit Interaction*, Phys. Rev. B **97**, 184513 (2018).

[198] A. Prakash, P. Xu, A. Faghaninia, S. Shukla, J. W. Ager, C. S. Lo, and B. Jalan, *Wide Bandgap BaSnO3 Films with Room Temperature Conductivity Exceeding 104 S Cm−1*, Nat. Commun. **8**, 15167 (2017).